Heavy-meson bag parameters using gradient flow

Matthew Black,[1,2,*] Robert V. Harlander,[3] Jonas T. Kohnen,[3] Fabian Lange,[4,5] Antonio Rago,[6] Andrea Shindler,[3,7,8] and Oliver Witzel[9]

[1]*Higgs Centre for Theoretical Physics, School of Physics and Astronomy, University of Edinburgh, Edinburgh EH9 3JZ, United Kingdom*
[2]*Theoretische Physik 1, Center for Particle Physics Siegen, Naturwissenschaftlich-Technische Fakultät, Universität Siegen, 57068 Siegen, Germany*
[3]*Institute for Theoretical Particle Physics and Cosmology, RWTH Aachen University, 52056 Aachen, Germany*
[4]*Physik-Institut, Universität Zürich, Winterthurerstrasse 190, 8057 Zürich, Switzerland*
[5]*PSI Center for Neutron and Muon Sciences, 5232 Villigen PSI, Switzerland*
[6]*IMADA and Quantum Theory Center, University of Southern Denmark, Odense, Denmark*
[7]*Nuclear Science Division, Lawrence Berkeley National Laboratory, Berkeley, California 94720, USA*
[8]*Department of Physics, University of California, Berkeley, California 94720, USA*
[9]*Theoretische Physik 1, Center for Particle Physics Siegen, Naturwissenschaftlich-Technische Fakultät, and Cluster of Excellence "Color meets Flavor," Universität Siegen, 57068 Siegen, Germany*

(Received 16 April 2026; accepted 24 September 2026; published 5 November 2026)

We demonstrate the use of the gradient flow combined with the short flow-time expansion (GF + SFTX) as a renormalization procedure for four-quark operator matrix elements and associated bag parameters relevant to neutral heavy-meson mixing ($\Delta Q = 2$) and heavy-meson lifetimes ($\Delta Q = 0$). Using six RBC/UKQCD $2+1$-flavor domain-wall fermion ensembles, we calculate for a charm-strange system with physical quark masses flowed bag parameters and match them to the $\overline{\text{MS}}$ scheme using perturbative SFTX coefficients up to next-to-next-to-leading order in QCD. We employ a multiscale matching strategy and a renormalization-group improved flow-time evolution which allows for a reliable estimate of systematic uncertainties. For a fictitious neutral D_s meson, we obtain the $\Delta Q = 2$ $\overline{\text{MS}}$ bag parameter $\mathcal{B}_1^{\overline{\text{MS}}}(3\text{ GeV}) = 0.7673(123)$, consistent with existing short-distance D^0 mixing determinations. For the $\Delta Q = 0$ lifetime-ratio operator basis, we find the $\overline{\text{MS}}$ results $B_1^{\overline{\text{MS}}}(3\text{ GeV}) = 1.0524(97)$, $B_2^{\overline{\text{MS}}}(3\text{ GeV}) = 0.9621(71)$, $\epsilon_1^{\overline{\text{MS}}}(3\text{ GeV}) = -0.2275(76)$, and $\epsilon_2^{\overline{\text{MS}}}(3\text{ GeV}) = -0.0005(8)$. We provide conversion formulae to reexpress these results for an arbitrary choice of evanescent operators. These results demonstrate that GF + SFTX can deliver precise determinations of dimension-six four-quark operators and establish a framework for future lattice computations including more complex operator bases, where the challenge of power-divergent mixing is shifted to the continuum and handled in the SFTX.

DOI: 10.1103/47j9-h8s5

I. INTRODUCTION

The physics of heavy hadrons involves short- and long-distance contributions from QCD. Using effective field theories such as the heavy-quark expansion (HQE), they can be factorized into perturbative Wilson coefficients and matrix elements of composite operators which need to be evaluated using nonperturbative methods. In particular, the mixing and decay processes of heavy mesons, which are at the focus of this paper, are mediated by four-quark operators of mass-dimension six, carrying a net heavy-quark flavor quantum number of $\Delta Q = 2$ and $\Delta Q = 0$, respectively. The relevant hadronic matrix elements are typically parameterized by so-called bag parameters. Their combination with the perturbative Wilson coefficients requires a common renormalization scheme, which presents one of the main obstacles in the theoretical description of these processes.

The calculation of bag parameters for neutral meson mixing is rather well established using numerical lattice QCD simulations [1–14]. Both perturbative [15,16] and nonperturbative [4,17–19] renormalization procedures have been used in the past. While percent-level precision [20] has been reached for the Standard Model (SM) operator

*Contact author: matthew.black@ed.ac.uk

Published by the American Physical Society under the terms of the Creative Commons Attribution 4.0 International license. Further distribution of this work must maintain attribution to the author(s) and the published article's title, journal citation, and DOI. Funded by SCOAP³.

describing neutral kaon-mixing, results for beyond Standard Model operators are in tension between the ETM Collaboration (ETMC) [10] and the determinations by the SWME [3] and RBC/UKQCD [6,21] Collaborations. SWME uses a perturbative renormalization scheme, whereas both ETMC and RBC/UKQCD perform a nonperturbative renormalization requiring gauge fixing, referred to as regularization-independent momentum-subtraction (RI-MOM). It has been suggested that the difference between ETMC and RBC/UKQCD originates from differently chosen kinematics in their RI-MOM schemes [19]. Currently most precise results for the SM mass-difference operator by the Fermilab/MILC [13] and HPQCD [14] Collaborations exhibit some tension as well; they both rely on perturbative renormalization using the $\overline{\text{MS}}$-NDR scheme.[1] An independent theoretical approach to meson mixing would certainly help to clarify this situation. It is the aim of this paper to provide such an approach by considering the short-distance contribution to D meson mixing, allowing us to compare to few-percent-level results which have been obtained by ETMC [9,10] and Fermilab/MILC [12].

Concerning the theoretical description of heavy-meson decays, one faces two major additional challenges. First, so-called "eye diagrams" occur whose lattice calculation is known to be numerically expensive. Subsequently, the renormalization of the $\Delta Q = 0$ operators introduces a mixing with operators of lower mass dimension, which on the lattice implies power divergences in $1/a$. While different strategies to calculate eye diagrams have been already pursued [23,24], the mixing of operators with lower mass dimensions remains one of the outstanding challenges. Recently, a gauge-invariant renormalization scheme has been proposed [25], and for the special case of four-quark operators using the static heavy-quark approximation an approach using position-space renormalization has been suggested [26]. Nevertheless, to date no lattice-QCD determination of the corresponding bag parameters with full error budget exists, despite some early works [27–29] as well as preliminary work [30] in the static limit.

To a good approximation, both the issue of the eye diagrams as well as the mixing with lower-dimensional operators can be eliminated by considering lifetime ratios rather than absolute lifetimes. However, even in this case, no determination of the bag parameters is available whose accuracy would be at the level of current experimental precision.

We evaluate bag parameters with the help of the gradient flow [31–34] in combination with the short flow-time expansion (SFTX) [35–37].[2] The gradient flow (GF) provides a gauge-invariant, UV-finite definition of composite operators, while the SFTX allows one to convert the corresponding matrix elements to the $\overline{\text{MS}}$ scheme. The window condition for the involved length (or mass) scales implied by this procedure is found to be comfortably fulfilled in our case. We claim that the GF + SFTX procedure is suitable for high-precision determinations of various hadronic quantities since it decreases discretization effects in the lattice calculation and has an easily-attainable matching condition to the $\overline{\text{MS}}$ scheme. This is supported by recent applications of this procedure to the determination of renormalized strange and charm quark masses [39] and parton distribution functions [40–44], as well as earlier work on the determination of thermodynamical quantities based on the energy-momentum tensor [45,46], for example.

We will apply the GF + SFTX method to D_s mesons which provide an ideal heavy-light laboratory for establishing the method. This has the advantage that in a fully relativistic setup both charm and strange quark can be tuned to their physical masses avoiding extrapolations in the mass or the use of effective actions. In addition, heavy-meson matrix elements warrant the use of a massive renormalization scheme to ensure a sufficient separation of scales, which typically poses additional challenges; alternative approaches to this challenge have been discussed in Refs. [47,48]. Moreover, heavy-light mesons exhibit a rich phenomenological structure, and further insight on the validity of the heavy-quark expansion for charm quarks is highly desired. Sum-rules techniques have been used by Ref. [49] to compute results for D mesons and thus provide a comparison point for our results. They use the heavy-quark effective theory (HQET) before matching to QCD for both D and B mesons which allows for an additional evaluation on the applicability of HQET for the charm quark, since it is much lighter than the bottom quark.

It is well known that the bag parameters in the $\overline{\text{MS}}$ scheme still have a residual scheme ambiguity related to the choice of so-called evanescent operators which are an intrinsic artifact of dimensional regularization. Any dependence on this choice will cancel in the combination of the bag parameters with the corresponding Wilson coefficients, which, therefore, need to be evaluated in the same scheme. We will present our final results for one specific scheme choice in this paper, but also provide conversion formulae to virtually arbitrary other schemes in Appendix B.

The remainder of this paper is organized as follows. We will first motivate our calculation with a discussion of the phenomenology of heavy mesons in Sec. II, before introducing the GF + SFTX formalism in Sec. III. The GF + SFTX method is based on three major components, all of which will then be provided in this paper. The first one is understanding the perturbative matching matrix between flowed and unflowed operators, whose calculation will be presented in Sec. IV; the second component is the lattice evaluation of matrix elements of flowed operators and their extrapolation to the continuum—details for this will be described in Secs. V and VI; and the third component is the extrapolation of the product of the first two components to

[1]Joint work by RBC/UKQCD and JLQCD using RI-(S)MOM renormalization is ongoing [22].

[2]Preliminary work towards a similar application of this topic was presented by the WHOT QCD Collaboration at Lattice 2019 [38].

vanishing flow time. For this latter part, we have developed a robust procedure which takes into account various systematic uncertainties (see Sec. VII) where also other sources of systematic effects are considered. We give our final results in the context of phenomenology in Sec. VIII, then Sec. IX presents our conclusions. Preliminary results have been presented in Refs. [50–52] and we highlight phenomenological importance of the obtained results for heavy-meson lifetimes in Ref. [53].

II. HEAVY-MESON PHENOMENOLOGY

Charm and bottom quarks are of special phenomenological interest. Due to their large mass, a plethora of decay modes exist which may be affected by physics beyond the SM. Studying the decays of heavy-light mesons containing one heavy quark Q is particularly promising due to the precise experimental results available, building on a long history of measurements from dedicated flavor factories as well as general-purpose collider programs.

From a theory perspective, the hadron's decay rate is largely dominated by the free weak decay of the heavy quark Q, while bound-state effects are suppressed by the heavy-quark mass. They can be consistently taken into account using the HQE [54,55], which is an operator product expansion (OPE) [56,57] based on the hierarchy $\Lambda_{\mathrm{QCD}} \ll m_Q$, where Λ_{QCD} is the QCD confinement scale and m_Q is the heavy quark mass. In the following general discussion, H denotes a (neutral) heavy-light D or B meson, i.e. the heavy quark Q is either a charm or bottom quark, whereas the light quark q can be up, down, or strange. Focusing on dimension-six four-quark operators, we discuss two interesting sectors of heavy quark phenomenology: the mixing of neutral mesons with their antiparticles (via $\Delta Q = 2$ operators), and spectator effects in the decay of heavy mesons (via $\Delta Q = 0$ operators).

A. Neutral heavy-meson mixing

For a neutral meson H (with quark content $Q\bar{q}$), the box diagrams shown in Fig. 1 induce the mixing with its antiparticle $\bar{H}$ (with quark content $\bar{Q}q$). The time evolution of this mixing is described by

$$\mathrm{i}\frac{\mathrm{d}}{\mathrm{d}t}\begin{pmatrix}|H(t)\rangle\\ |\bar{H}(t)\rangle\end{pmatrix} = \left(\hat{M} - \frac{\mathrm{i}}{2}\hat{\Gamma}\right)\begin{pmatrix}|H(t)\rangle\\ |\bar{H}(t)\rangle\end{pmatrix}. \tag{1}$$

Diagonalizing the matrices $\hat{M}$ and $\hat{\Gamma}$ leads to the heavy- (H_{H}) and light- (H_{L}) mass eigenstates of the system. The differences in the mass and decay rates of H_{H} and H_{L} are determined by the off diagonal elements of the dispersive matrix $\hat{M}$ and absorptive matrix $\hat{\Gamma}$, respectively,

$$\Delta M = 2|M_{12}|, \qquad \Delta\Gamma = 2|\Gamma_{12}|\cos\phi_{12}, \tag{2}$$

where $\phi_{12} = \arg(-M_{12}/\Gamma_{12})$. The mass differences ΔM are well measured by experiments; in particular, after a rich history of measurements [58–105], they have reached subpercent level precision for B_d mesons and subpermille level precision for B_s mesons, while D^0 mixing, which occurs at much lower frequencies, is measured with 10% level accuracy. The world averages of the mass differences as determined by the heavy-flavor averaging group (HFLAV) [106] are

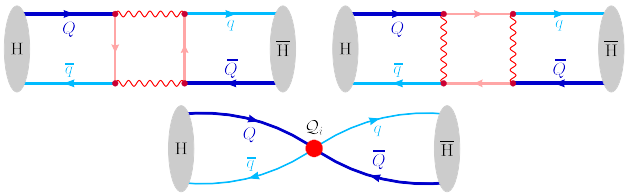


FIG. 1. SM box diagrams contributing to neutral-meson mixing (top). After integrating out the heavy electroweak degrees of freedom, this is represented by a pointlike $\Delta Q = 2$ four-quark operator (bottom). The diagrams were produced with the help of FEYNGAME [110,111].

$$\begin{aligned}\Delta M_{B_d} &= 0.5069 \pm 0.0019\ \mathrm{ps}^{-1},\\ \Delta M_{B_s} &= 17.765 \pm 0.006\ \mathrm{ps}^{-1},\\ \Delta M_{D^0} &= 9.4 \pm 1.1\ \mathrm{ns}^{-1}.\end{aligned} \tag{3}$$

Theoretically, the off diagonal elements M_{12} and Γ_{12} in Eq. (2) can be expressed as

$$2M_H\left(M_{12} - \frac{\mathrm{i}}{2}\Gamma_{12}\right) = \langle H|\mathcal{H}_{\mathrm{eff}}^{\Delta Q=2}|\bar{H}\rangle + \sum_n \frac{\langle H|\mathcal{H}_{\mathrm{eff}}^{\Delta Q=1}|n\rangle\langle n|\mathcal{H}_{\mathrm{eff}}^{\Delta Q=1}|\bar{H}\rangle}{M_H - E_n + \mathrm{i}\epsilon}, \tag{4}$$

where M_H refers to the average mass of the meson H, and $\mathcal{H}_{\mathrm{eff}}^{\Delta Q=1}$, $\mathcal{H}_{\mathrm{eff}}^{\Delta Q=2}$ denote weak effective Hamiltonians consisting of $\Delta Q = 1$ and $\Delta Q = 2$ operators. The sum over n represents all possible states which the meson H can decay into with energy E_n. While the first term only contributes to $\hat{M}$, the second term contributes to both $\hat{M}$ and $\hat{\Gamma}$ in Eq. (4). The interactions incorporated in the second term are inherently long distance, and their proper calculation presents a significant challenge (for an overview in the context of D mesons, see Ref. [107], and for a proposed strategy to tackle this problem with lattice QCD, see Ref. [108]). For the mass differences ΔM of B mesons, these long-distance effects are negligible [107,109], however they are in fact the dominant contribution for D mesons. It also follows that these long-distance interactions generate the decay-rate difference $\Delta\Gamma$ for all heavy mesons.

Nevertheless, in the context of ΔM, our focus in this paper is on the $\Delta Q = 2$ effective Hamiltonian. Its matrix elements are formed from short-distance operators inserted between clearly-defined meson states which are well suited to be

extracted on the lattice. In the SM, this Hamiltonian yields a contribution from a single $\Delta Q = 2$ operator,[3] namely

$$\mathcal{Q}_1 = (\bar{Q}\gamma_\mu(1-\gamma_5)q)(\bar{Q}\gamma_\mu(1-\gamma_5)q), \tag{5}$$

whose Wilson coefficient is known to next-to-leading order (NLO) [112,113]. First estimates of the matrix element of this operator used the vacuum insertion approximation (VIA), which assumes that the matrix element of any four-quark operator is saturated by the intermediary vacuum state between two quark bilinears, i.e.

$$\langle H|\mathcal{O}|\bar{H}\rangle \overset{\text{VIA}}{=} \langle H|\bar{Q}^i C_{ij}\Gamma_1 q^j|0\rangle \cdot \langle 0|\bar{Q}^k C_{kl}\Gamma_2 q^l|\bar{H}\rangle, \tag{6}$$

where Γ_1 and Γ_2 are the Dirac structures of each bilinear in the four-quark operator and C_{ij} and C_{kl} represent generic color structures such as δ_{ij} or T^A_{ij} for fundamental color indices i, j, k, l and adjoint index A. For example, if we consider the VIA for operator $\mathcal{Q}_1$ from Eq. (5), first we can identify the matrix element of the two (identical) quark bilinears as

$$\langle H(\vec{p})|\bar{Q}\gamma^\mu(1-\gamma_5)q|0\rangle = -\mathrm{i}f_H p^\mu, \tag{7}$$

which is just the matrix element of the axial-vector current. Then, the matrix element of $\mathcal{Q}_1$ in the VIA is given by

$$\langle H|\mathcal{Q}_1|\bar{H}\rangle \overset{\text{VIA}}{=} \frac{8}{3} f_H^2 M_H^2, \tag{8}$$

where the additional factor $8/3$ accounts for spin and color algebra. Beyond the VIA, an additional hadronic quantity is introduced which parametrizes the deviation of the true matrix element from Eq. (6). This is the bag parameter, $\mathcal{B}_1^H(\mu)$, which carries a dependence on the renormalization scale μ. The full matrix element of $\mathcal{Q}_1$ is then given as

$$\langle H|\mathcal{Q}_1|\bar{H}\rangle(\mu) = \frac{8}{3} f_H^2 M_H^2 \mathcal{B}_1^H(\mu), \tag{9}$$

which is parametrized in terms of the decay constant f_H, the mass M_H, and the bag parameter $\mathcal{B}_1^H(\mu)$. By comparing Eqs. (8) and (9), one can see that in the VIA, $\mathcal{B}_1^H(\mu) = 1$. Since the meson mass M_H is precisely measured [114] and the decay constant is well predicted from nonperturbative methods [20], it is convenient to focus our efforts on calculating the bag parameter in order to contribute to the precise determination of the four-quark matrix element.

The bag parameter $\mathcal{B}_1^H(\mu)$ has been determined for both neutral B and D mesons using sum rule techniques in HQET [115–118], and also from lattice QCD calculations [1,5,8–10,12–14,22]. Beyond mass-dimension six, the matrix elements of the dimension-seven four-quark operators have been explored in lattice QCD by the HPQCD Collaboration [119] using tree-level matching between lattice and the $\overline{\text{MS}}$ scheme.

[3]The SM prediction of $\Delta\Gamma$ inherits two more four-quark operators of the $\Delta Q = 2$ Hamiltonian by applying the HQE to the long-distance term [109].

B. Heavy-meson lifetimes

The lifetimes of heavy mesons have received much attention from various experiments over the years, leading to high-precision results for B mesons [63,73,74,77,85,89,120–174] as well as for D mesons [169,175–186]. Concerning B mesons, HFLAV [106] combines these results to find

$$\begin{aligned}
&\tau(B^0) = 1.517 \pm 0.004 \text{ ps}, \\
&\tau(B^+) = 1.638 \pm 0.004 \text{ ps}, \quad \frac{\tau(B^+)}{\tau(B^0)} = 1.076 \pm 0.004, \\
&\tau(B_s^0) = 1.516 \pm 0.006 \text{ ps}, \quad \frac{\tau(B_s^0)}{\tau(B^0)} = 1.0021 \pm 0.0034,
\end{aligned} \tag{10}$$

while the D-meson measurements are combined by the Particle Data Group (PDG) [114] to give

$$\begin{aligned}
&\tau(D^0) = 0.4103 \pm 0.0010 \text{ ps}, \\
&\tau(D^+) = 1.033 \pm 0.005 \text{ ps}, \quad \frac{\tau(D^+)}{\tau(D^0)} = 2.518 \pm 0.014, \\
&\tau(D_s^+) = 0.5012 \pm 0.0022 \text{ ps}, \quad \frac{\tau(D_s^+)}{\tau(D^0)} = 1.2215 \pm 0.006.
\end{aligned} \tag{11}$$

The decay rate of a heavy-meson H is given by $\hat{\Gamma}_{11}$ of Eq. (1), which, similar to Eq. (4), can be written as the sum of the decay of H to all possible final states n,

$$\Gamma_H = \frac{1}{2M_H}\sum_n \int_{\text{PS}} (2\pi)^4 \delta^{(4)}(p_H - p_n)|\langle n|\mathcal{H}_{\text{eff}}^{\Delta Q=1}|H\rangle|^2, \tag{12}$$

where $\mathcal{H}_{\text{eff}}^{\Delta Q=1}$ is the weak effective Hamiltonian describing the decay of the heavy quark Q, and $\int_{\text{PS}}$ denotes the phase-space integral for each final state n. Via the optical theorem, this expression can be related to the imaginary part of the forward-scattering amplitude. The corresponding "transition operator"

$$\mathcal{T}^{\Delta Q=0} = \mathrm{i}\int d^4x\, \mathrm{T}\{\mathcal{H}_{\text{eff}}^{\Delta Q=1}(x)\mathcal{H}_{\text{eff}}^{\Delta Q=1}(0)\} \tag{13}$$

has $\Delta Q = 0$, because it mediates between two identical external states. In turn, the total decay rate of H can be

reexpressed as

$$\Gamma_H = \frac{1}{2M_H}\mathrm{Im}\langle H|\mathcal{T}^{\Delta Q=0}|H\rangle. \tag{14}$$

In the limit where the heavy quark Q is infinitely heavy, the decay rate of the heavy hadron is identical to the decay rate of the free heavy quark. The HQE allows one to systematically include corrections to this infinite mass limit. By assuming that the heavy quark Q inside the meson interacts with the light degrees of freedom via momentum exchanges $O(\Lambda_{\mathrm{QCD}}) \ll m_Q$, one can see that the heavy quark's momentum will be dominated by its mass and can thus be decomposed as

$$p_Q^\mu = m_Q v^\mu + k^\mu, \tag{15}$$

where v^μ is the meson velocity and $k^\mu \sim O(\Lambda_{\mathrm{QCD}})$ is the residual momentum stemming from nonperturbative interactions with the meson's light degrees of freedom. The heavy-quark field can therefore be rescaled as

$$Q(x) = \mathrm{e}^{-\mathrm{i}m_Q v\cdot x} Q_v(x), \tag{16}$$

such that the field $Q_v(x)$ contains only low frequencies of order k. From here on, when discussing heavy quark fields, we are referring to this rescaled field $Q_v(x)$. This allows us to perform a second OPE upon the transition operator $\mathcal{T}^{\Delta Q=0}$ of Eq. (13) via the small parameter $\Lambda_{\mathrm{QCD}}/m_Q \ll 1$,[4] which expresses the decay rate as

$$\Gamma_H = \Gamma_3 + \cdots + 16\pi^2\left[\Gamma_6 \frac{\overline{\langle \mathcal{O}_6\rangle}}{m_Q^3} + \Gamma_7 \frac{\overline{\langle \mathcal{O}_7\rangle}}{m_Q^4} + \cdots\right], \tag{17}$$

where, for each mass-dimension d, Γ_d are short-distance coefficients computed in perturbation theory, and $\overline{\langle \mathcal{O}_d\rangle} \equiv \langle H|\mathcal{O}_d|H\rangle/2M_H$ are the matrix elements of the operators of the $\Delta Q = 0$ effective Hamiltonian. The free decay of the heavy quark Q is described by the leading term Γ_3, while corrections arise starting at $O(1/m_Q^2)$, induced by two-quark operators of mass-dimension five, contained in the first ellipse of Eq. (17); see Ref. [188] for an overview. The four-quark operators $\mathcal{O}_d$, which are of interest here, first arise at mass-dimension six, and carry a relative factor of $16\pi^2$ from loop enhancement compared to the two-quark operators; see e.g. Ref. [189]. Their Wilson coefficients $\Gamma_{6/7}$ are known to NLO [190–196] and leading order (LO) [197,198] respectively. In the SM, the $\Delta Q = 0$ four-quark operators appearing at mass-dimension six are[5]

$$\begin{aligned}
\mathcal{O}_1 &= (\bar{Q}\gamma_\mu(1-\gamma_5)q)(\bar{q}\gamma^\mu(1-\gamma_5)Q),\\
T_1 &= (\bar{Q}\gamma_\mu(1-\gamma_5)T^A q)(\bar{q}\gamma^\mu(1-\gamma_5)T^A Q),\\
\mathcal{O}_2 &= (\bar{Q}(1-\gamma_5)q)(\bar{q}(1+\gamma_5)Q),\\
T_2 &= (\bar{Q}(1-\gamma_5)T^A q)(\bar{q}(1+\gamma_5)T^A Q),
\end{aligned} \tag{18}$$

where T^A are the generators of SU(3) color. Feynman diagrams illustrating the line of reasoning from the SM description of the heavy-meson decay to the HQE formulation are shown in Fig. 2. When considering absolute lifetimes, however, so-called eye diagrams also contribute; see Fig. 3. On the lattice, their signal-to-noise ratio is notoriously challenging. In addition, the calculation of absolute lifetimes involves contributions from lower-dimensional operators, indicated by the right diagram in Fig. 3, implying power divergences on the lattice. They also require significantly increased efforts on the perturbative side due to the mixing with unphysical operators. However, both of these types of contributions cancel when considering lifetime ratios in the limit of isospin (or $\mathrm{SU(3)_F}$) symmetry; see e.g. Ref. [49]. Furthermore, the bag parameters contributing to absolute lifetimes have been computed in HQET within the sum-rule framework of Refs. [199,200]. In those studies, the eye-diagram contributions in HQET were found to be $O(0.2\%)$, and we assume that their magnitude does not change significantly when going from HQET to full QCD. For the sake of this first study, we will therefore focus on the assumption of $\mathrm{SU(3)_F}$ symmetry, thus avoiding the associated technical problems. Nevertheless, our method should be applicable also for absolute lifetimes, as we will discuss in more detail below.

Continuing with the operators of Eq. (18), in analogy to Eq. (9), their matrix elements are parametrized in terms of the decay constant f_H, quark and hadron masses m_q, m_Q,

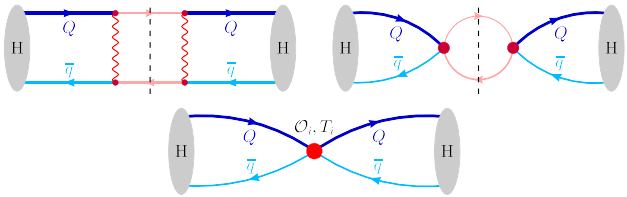


FIG. 2. Imaginary part of a $\Delta Q = 0$ box diagram in the SM (top left). After integrating out the W bosons, this is described by a double insertion of the resulting $\Delta Q = 1$ effective weak Hamiltonian (top right) which can be matched to local $\Delta Q = 0$ four-quark operators of the HQE (bottom).

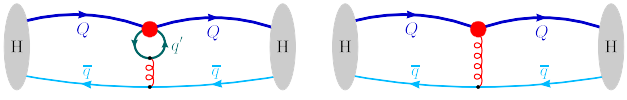


FIG. 3. Eye diagram (left) and contributions from lower-dimensional operators (right). The quark q' forming the "eye" can be any light quark flavor.

[4]The question of suitability of the HQE for a charm quark is challenging and remains open; see e.g. Ref. [187].

[5]The dimension-seven four-quark operators have yet to be studied beyond the VIA and are beyond the scope of this work.

and M_H, and the bag parameters B_i^H, ϵ_i^H (for $i = 1, 2$) describing the deviation from the VIA:

$$\begin{aligned}\langle H|\mathcal{O}_1|H\rangle &= f_H^2 M_H^2 B_1^H,\\ \langle H|\mathcal{O}_2|H\rangle &= \frac{M_H^2}{(m_Q+m_q)^2} f_H^2 M_H^2 B_2^H,\\ \langle H|T_1|H\rangle &= f_H^2 M_H^2 \epsilon_1^H,\\ \langle H|T_2|H\rangle &= \frac{M_H^2}{(m_Q+m_q)^2} f_H^2 M_H^2 \epsilon_2^H.\end{aligned} \tag{19}$$

The bag parameters B_i^H of the color-singlet operators $\mathcal{O}_i$ share a similar notation to the $\Delta Q = 2$ operators, motivated by the similarity of the operators, while the color-octet operators T_i have their bag parameters written instead as ϵ_i^H. A clear distinction can be understood by comparing their values in the VIA, where

$$B_i^{H\,\mathrm{VIA}} = 1, \qquad \epsilon_i^{H\,\mathrm{VIA}} = 0. \tag{20}$$

Similarly to the case of neutral meson mixing, HQET sum rules can be applied to predict the bag parameters of the $\Delta Q = 0$ operator basis and have yielded results for B and D meson lifetimes and lifetime ratios [49,116,117,187,199,200]. However, as discussed above, there are no complete determinations of these quantities from lattice QCD.

C. Renormalization of bag parameters

In a general prescription, renormalized operators are given by

$$\mathcal{O}_i^{\mathrm{ren}} = \sum_j Z_{ij}\mathcal{O}_j, \tag{21}$$

where Z_{ij} is the renormalization matrix. Importantly for lattice calculations, this renormalization must occur at finite lattice spacing (defining operators at a scale $a\mu$ in e.g. the RI-MOM scheme) in order to properly define a continuum limit. In simple cases, this mainly introduces additional cutoff effects which must be controlled and can be particularly delicate for heavy-quark processes [48]. For more complicated operator bases—such as those for lifetime calculations including eye contractions—lattice symmetries may allow for mixing with lower-dimensional operators whose coefficients $\propto 1/a^n$ such that the continuum limit is not meaningful unless these contributions are properly accounted for. A renormalization scheme that both improves the approach to the continuum limit and avoids power-divergent subtractions at finite a is highly desirable. The GF formalism indeed provides such a scheme, as we will review in the following.

III. GRADIENT FLOW RENORMALIZATION

A. Flow equations

The QCD GF formalism [33,35] extends the QCD fields by an auxiliary parameter, the flow time τ which has mass-dimension $[\tau] = -2$. The *flowed fields* $\chi, \bar{\chi}, \mathcal{A}$ are connected to the regular QCD fields $\psi_f, \bar{\psi}_f, A$ via the initial conditions

$$\begin{aligned}\chi_f(\tau = 0, x) &= \psi_f(x),\\ \bar{\chi}_f(\tau = 0, x) &= \bar{\psi}_f(x),\\ \mathcal{A}_\mu^A(\tau = 0, x) &= A_\mu^A(x).\end{aligned} \tag{22}$$

We denote color indices in the adjoint representation by capital letters A, B, C, while f denotes the flavor e.g. $\psi_f \in \{Q, q\}$.

At positive flow time, the behavior of the flowed fields is described by the flow equations

$$\begin{aligned}\partial_\tau \mathcal{A}_\mu^A &= D_\nu^{AB} G_{\nu\mu}^B + \kappa D_\mu^{AB}\partial_\nu \mathcal{A}_\nu^B,\\ \partial_\tau \chi &= \Delta\chi + \mathrm{i}\kappa g_0 \partial_\mu \mathcal{A}_\mu^A T^A \chi,\\ \partial_\tau \bar{\chi} &= \bar{\chi}\,\overleftarrow{\Delta} - \mathrm{i}\kappa g_0 \bar{\chi}\partial_\mu \mathcal{A}_\mu^A T^A,\end{aligned} \tag{23}$$

where

$$\Delta = D_\mu^{\mathrm{F}} D_\mu^{\mathrm{F}}, \qquad \overleftarrow{\Delta} = \overleftarrow{D}_\mu^{\mathrm{F}} \overleftarrow{D}_\mu^{\mathrm{F}}, \tag{24}$$

and

$$\begin{aligned}D_\mu^{AB} &= \partial_\mu \delta^{AB} - g_0 f^{ABC}\mathcal{A}_\mu^C,\\ D_\mu^{\mathrm{F}} &= \partial_\mu - \mathrm{i}g_0 \mathcal{A}_\mu^A T^A,\\ \overleftarrow{D}_\mu^{\mathrm{F}} &= \overleftarrow{\partial}_\mu + \mathrm{i}g_0 \mathcal{A}_\mu^A T^A,\end{aligned} \tag{25}$$

with the bare QCD coupling g_0, and $[T^A, T^B] = \mathrm{i}f^{ABC}T^C$. The flowed field-strength tensor is given by

$$G_{\mu\nu}^A = \partial_\mu \mathcal{A}_\nu^A - \partial_\nu \mathcal{A}_\mu^A + g_0 f^{ABC}\mathcal{A}_\mu^B \mathcal{A}_\nu^C. \tag{26}$$

The parameter κ is a flowed gauge parameter [33]; in the perturbative calculation (see Sec. IV), it is advantageous to set $\kappa = 1$, while we set κ to zero on the lattice. However, our lattice and perturbative results are separately independent of this choice. Using the flow equations, one can derive a Lagrangian of flowed QCD [35], which incorporates the Feynman rules of regular (unflowed) QCD as well as additional flowed Feynman rules, which are listed in Ref. [201].

The solutions of the flow equations of Eq. (23) lead to an exponential suppression of high-momentum modes. In particular, composite operators of flowed fields do not require any operator renormalization [34,35,202]. In our choice of normalization, the flowed gluon field renormalizes in the same way as the gauge coupling, while flowed quarks need to be renormalized in order to result in finite

Green's functions. Throughout our perturbative calculation, we will adopt the ringed scheme, defined as [203]

$$\mathring{\chi}(\tau) = \mathring{Z}_\chi^{1/2}(\tau)\chi(\tau), \qquad \langle \mathring{\bar{\chi}} \not{D}^{\mathrm{F}} \mathring{\chi} \rangle \equiv -\frac{2N_c}{(4\pi\tau)^2}, \tag{27}$$

where $N_c = 3$ is the number of colors. The explicit form of $\mathring{Z}_\chi$ is given in Appendix A. Our results for the perturbative matching coefficients of the four-quark operators in Sec. IV C will be provided in this scheme. However, as we will see later, the wave function renormalization factors $\mathring{Z}_\chi$ actually cancel in the ratios of matrix elements defining the bag parameters. The renormalization of the QCD parameters (coupling and quark masses) is the same as in regular QCD.

B. Short flow-time expansion

With the gradient flow, the Wilson coefficients C_n and operators $\mathcal{O}_n$ of an effective Hamiltonian can be expressed in terms of *flowed operators* $\tilde{\mathcal{O}}_n(\tau)$, composed of flowed fields, and *flowed Wilson coefficients* $\tilde{C}_n(\tau)$, i.e.

$$\mathcal{H}_{\mathrm{eff}} = \sum_n C_n \mathcal{O}_n = \sum_n \tilde{C}_n(\tau)\tilde{\mathcal{O}}_n(\tau). \tag{28}$$

While Wilson coefficients and matrix elements of operators depend on the choice of the renormalization scheme, the effective Hamiltonian itself (and therefore any physical observable derived from it) is independent of this choice (up to perturbative truncation effects). This does not change in the flowed theory, where the dependence on the flow time between the operator matrix elements and Wilson coefficients will mutually cancel. In the short flow-time expansion, the relation between matrix elements of the flowed operators and the regular ones is

$$\langle \tilde{\mathcal{O}}_n(\tau) \rangle = \sum_m \zeta_{nm}(\tau,\mu) \langle \mathcal{O}_m^{\overline{\mathrm{MS}}} \rangle(\mu) + O(\tau), \tag{29}$$

where $\zeta_{nm}(\tau,\mu)$ are perturbatively calculated matching coefficients, and $\mathcal{O}^{\overline{\mathrm{MS}}}$ are the regular operators renormalized in the $\overline{\mathrm{MS}}$ scheme. Therefore, by inverting this relation, the matrix elements of the operators in the $\overline{\mathrm{MS}}$ scheme can be obtained from the matrix elements of the flowed operators with the help of the inverse matching matrix.

In our analysis, terms of order τ (and higher) will be neglected in Eq. (29), meaning that the rhs of Eq. (28) will have a residual flow-time dependence of $O(\tau)$, implying an upper limit on τ in its applicability that needs to be quantified. Strict independence on τ is formally reached only in the limit $\tau \to 0$. However, in a lattice evaluation of the flowed matrix elements, the "smearing radius" $\sqrt{8\tau}$ must be larger than the lattice spacings in order to suppress discretization effects coming from the boundary and to sufficiently approach a renormalized trajectory. Moreover, the perturbative matching coefficients depend on the renormalization scale μ, which needs to be chosen in a regime where the strong coupling $\alpha_s(\mu)$ assumes perturbative values. The dependence on τ is logarithmic, which also restricts its values to a finite interval in order to preserve perturbativity. One therefore needs to identify a window $\tau \in [\tau_{\min}, \tau_{\max}]$ in flow time where all these aspects are taken into account, and which allows for a reliable extrapolation $\tau \to 0$ within well-defined uncertainties. We will show that, in our case, a suitable interval for τ exists. We will describe in detail our procedure for the $\tau \to 0$ extrapolation, resulting in the bag parameters in the $\overline{\mathrm{MS}}$ scheme at a fixed renormalization scale μ_0.

It is worth pointing out that any mixing which occurs in lattice operator renormalization as power divergences in $1/a^n$ will turn into divergences of the form $1/\tau^{n/2}$ in the GF + SFTX procedure; see e.g. [204]. Such terms are absent for the operator basis presented here; they will appear when including the full operator basis for absolute lifetimes through eye diagrams and penguin operators though. The main strategy for renormalizing these operators using GF + SFTX remains the same as described here, however.

C. Application to the four-quark operators

Focusing on heavy-meson mixing and lifetime ratios, the set of flowed operators is simply obtained by replacing the regular fields in Eqs. (5) and (18) by flowed ones. Adopting a unified notation for both mixing and lifetime operators, we write them as

$$\begin{aligned}
\tilde{\mathcal{O}}_1 &= \mathring{Z}_\chi^2 (\bar{\chi}_\alpha \gamma_\mu (1-\gamma_5)\chi_\beta)(\bar{\chi}_\gamma \gamma_\mu (1-\gamma_5)\chi_\delta), \\
\tilde{T}_1 &= \mathring{Z}_\chi^2 (\bar{\chi}_\alpha \gamma_\mu (1-\gamma_5) T^A \chi_\beta)(\bar{\chi}_\gamma \gamma_\mu (1-\gamma_5) T^A \chi_\delta), \\
\tilde{\mathcal{O}}_2 &= \mathring{Z}_\chi^2 (\bar{\chi}_\alpha (1-\gamma_5)\chi_\beta)(\bar{\chi}_\gamma (1+\gamma_5)\chi_\delta), \\
\tilde{T}_2 &= \mathring{Z}_\chi^2 (\bar{\chi}_\alpha (1-\gamma_5) T^A \chi_\beta)(\bar{\chi}_\gamma (1+\gamma_5) T^A \chi_\delta),
\end{aligned} \tag{30}$$

where $\mathring{Z}_\chi$ is the flowed quark renormalization in the ringed scheme as defined in Eq. (27). The indices α, β, γ, δ in Eq. (30) denote the quark flavor. By choosing the initial conditions $\chi(\tau = 0) = \psi$, with

$$\psi_\alpha = \psi_\gamma = Q, \qquad \psi_\beta = \psi_\delta = q, \tag{31}$$

$\tilde{\mathcal{O}}_1$ corresponds to the flowed version of the mixing operator $\mathcal{Q}_1$ in Eq. (5), while setting

$$\psi_\alpha = \psi_\delta = Q, \qquad \psi_\beta = \psi_\gamma = q \tag{32}$$

leads to the flowed versions of the lifetime operators of Eq. (18). The lattice evaluation of the corresponding matrix elements relevant for heavy-meson mixing and decay will be described in Secs. V and VI. Before that, we describe the perturbative calculation of the corresponding matching coefficients.

IV. PERTURBATIVE MATCHING COEFFICIENTS

We will calculate matching matrices for the flowed operators of Eq. (30) through next-to-next-to-leading order (NNLO) QCD. Since we focus on mixing parameters and lifetime ratios, we can assume that the flavor indices of the four quark fields in Eq. (30) are mutually distinct, i.e. we can assume that they denote quarks of four different flavors. For the sake of clarity, the discussion in this section is mostly devoted to the lifetime operators. The treatment of the mixing operator will be discussed at the end of Sec. IV C.

According to the color structure of the operators in Eqs. (18) and (30), the matching matrix is block diagonal, so that we can write the SFTX at the operator level as

$$\begin{pmatrix} \tilde{\mathcal{O}}_i \\ \tilde{T}_i \end{pmatrix} = \zeta_i \begin{pmatrix} \mathcal{O}_i^{\overline{\mathrm{MS}}} \\ T_i^{\overline{\mathrm{MS}}} \end{pmatrix}, \qquad i \in \{1,2\}, \tag{33}$$

with the 2×2 matching matrices ζ_1 and ζ_2.

A. Evanescent operators

It is well known that the operator bases of Eqs. (5) and (18) are not closed under renormalization when working in dimensional regularization. Instead, one needs to include so-called evanescent operators [205–207] which vanish in $D = 4$ space-time dimensions due to algebraic identities [208], but are nonzero when working at $D = 4 - 2\epsilon$. At each perturbative order, additional evanescent operators have to be introduced. Their choice is not unique and can affect the finite parts of the final results, thus defining subvariants of the $\overline{\mathrm{MS}}$ scheme. In the main part of this paper, we will adopt the following set of evanescent operators for the lifetime calculations, referring to it as the *minimal basis* [cf. Eq. (32) for the notation]:

$$\begin{aligned}
\mathcal{E}^{(1)}_{\mathcal{O}_1} &= (\bar{\psi}_\alpha \gamma_{\mu\nu\rho}(1-\gamma_5)\psi_\beta)(\bar{\psi}_\gamma \gamma_{\rho\nu\mu}(1-\gamma_5)\psi_\delta) - 4\mathcal{O}_1, \\
\mathcal{E}^{(1)}_{T_1} &= (\bar{\psi}_\alpha \gamma_{\mu\nu\rho}(1-\gamma_5)T^A\psi_\beta)(\bar{\psi}_\gamma \gamma_{\rho\nu\mu}(1-\gamma_5)T^A\psi_\delta) - 4T_1, \\
\mathcal{E}^{(1)}_{\mathcal{O}_2} &= (\bar{\psi}_\alpha \gamma_{\mu\nu}(1-\gamma_5)\psi_\beta)(\bar{\psi}_\gamma \gamma_{\nu\mu}(1+\gamma_5)\psi_\delta) - 4\mathcal{O}_2, \\
\mathcal{E}^{(1)}_{T_2} &= (\bar{\psi}_\alpha \gamma_{\mu\nu}(1-\gamma_5)T^A\psi_\beta)(\bar{\psi}_\gamma \gamma_{\nu\mu}(1+\gamma_5)T^A\psi_\delta) - 4T_2,
\end{aligned} \tag{34}$$

and

$$\begin{aligned}
\mathcal{E}^{(2)}_{\mathcal{O}_1} &= (\bar{\psi}_\alpha \gamma_{\mu\nu\rho\sigma\tau}(1-\gamma_5)\psi_\beta)(\bar{\psi}_\gamma \gamma_{\tau\sigma\rho\nu\mu}(1-\gamma_5)\psi_\delta) - 16\mathcal{O}_1, \\
\mathcal{E}^{(2)}_{T_1} &= (\bar{\psi}_\alpha \gamma_{\mu\nu\rho\sigma\tau}(1-\gamma_5)T^A\psi_\beta)(\bar{\psi}_\gamma \gamma_{\tau\sigma\rho\nu\mu}(1-\gamma_5)T^A\psi_\delta) \\
&\quad - 16T_1, \\
\mathcal{E}^{(2)}_{\mathcal{O}_2} &= (\bar{\psi}_\alpha \gamma_{\mu\nu\rho\sigma}(1-\gamma_5)\psi_\beta)(\bar{\psi}_\gamma \gamma_{\sigma\rho\nu\mu}(1+\gamma_5)\psi_\delta) - 16\mathcal{O}_2, \\
\mathcal{E}^{(2)}_{T_2} &= (\bar{\psi}_\alpha \gamma_{\mu\nu\rho\sigma}(1-\gamma_5)T^A\psi_\beta)(\bar{\psi}_\gamma \gamma_{\sigma\rho\nu\mu}(1+\gamma_5)T^A\psi_\delta) \\
&\quad - 16T_2,
\end{aligned} \tag{35}$$

where

$$\gamma_{\mu_1 \ldots \mu_n} = \gamma_{\mu_1} \cdots \gamma_{\mu_n}. \tag{36}$$

The $\mathcal{E}^{(n)}_{\mathcal{O}_i}, \mathcal{E}^{(n)}_{T_i}$ are required for the calculation of the ζ_i, $i \in \{1,2\}$ at n-loop level, respectively, cf. Eq. (58). In our calculation, we actually allow for a more general choice of evanescent operators, as described in Appendix B. The results and anomalous dimensions in this general scheme can be found in the ancillary file; see Appendix C and Ref. [209].

A priori, the evanescent operators contribute to the SFTX of the physical operators. The matching matrix of the full operator basis can be schematically written as

$$\begin{pmatrix} \tilde{\mathcal{O}}(\tau) \\ \tilde{\mathcal{E}}(\tau) \end{pmatrix} = \begin{pmatrix} \zeta_{\mathcal{O}\mathcal{O}}(\tau,\mu) & \zeta_{\mathcal{O}\mathcal{E}}(\tau,\mu) \\ \zeta_{\mathcal{E}\mathcal{O}}(\tau,\mu) & \zeta_{\mathcal{E}\mathcal{E}}(\tau,\mu) \end{pmatrix} \begin{pmatrix} \mathcal{O}^{\mathrm{R}}(\mu) \\ \mathcal{E}^{\mathrm{R}}(\mu) \end{pmatrix}, \tag{37}$$

where

$$\begin{pmatrix} \mathcal{O}^{\mathrm{R}} \\ \mathcal{E}^{\mathrm{R}} \end{pmatrix} = \begin{pmatrix} \mathcal{Z}_{\mathcal{O}\mathcal{O}} & \mathcal{Z}_{\mathcal{O}\mathcal{E}} \\ \mathcal{Z}_{\mathcal{E}\mathcal{O}} & \mathcal{Z}_{\mathcal{E}\mathcal{E}} \end{pmatrix} \begin{pmatrix} \mathcal{O} \\ \mathcal{E} \end{pmatrix}. \tag{38}$$

Here, $\mathcal{O}$ and $\mathcal{E}$ refer to the collection of physical and evanescent operators, respectively. The submatrix $\mathcal{Z}_{\mathcal{E}\mathcal{O}}$ contains a nonminimal finite part which is defined such that the renormalized evanescent operators vanish at $D = 4$ [205–207] and thus do not contribute to physical observables. Explicit results are given in Appendix A. In the GF, this renormalization condition can be implemented by requiring that [210]

$$\zeta_{\mathcal{E}\mathcal{O}}(\tau,\mu) = \mathcal{O}(\epsilon). \tag{39}$$

This follows from the fact that matrix elements of flowed operators are free from UV divergences; one can therefore write $\langle \tilde{\mathcal{E}}(\tau) \rangle = \mathcal{O}(\epsilon)$. Combining Eqs. (37) and (39) then also enforces $\langle \mathcal{E}^{\mathrm{R}}(\mu) \rangle = \mathcal{O}(\epsilon)$. The results for the finite renormalization matrix in a general scheme of evanescent operators are provided in the ancillary file; see Appendix C and Ref. [209].

B. Method of projectors

Our procedure to determine the matching matrices ζ_i of Eq. (33) relies on the method of projectors [211,212]. For each of the operators of Eq. (18) (assuming four different quark flavors; see above) as well as each of the evanescent operators of Sec. IV A, we construct a projector P_i, consisting of external states and derivatives w.r.t. masses and external momenta, such that

$$P_i[\mathcal{O}_j] = \delta_{ij}. \tag{40}$$

Setting all masses and external momenta to zero before loop integration eliminates all higher-order contributions on the lhs of this relation. Applying these projectors on the

flowed operators thus directly gives the individual components of the matching matrix [213],

$$\zeta_{mn} = P_n[\tilde{\mathcal{O}}_m]. \tag{41}$$

For the calculation of the resulting Feynman diagrams, we use an updated version of the setup described in Ref. [201] which consists of `qgraf` [214,215] for generating the Feynman diagrams, `tapir/exp` [216–218][6] for identifying the momentum topologies and inserting the Feynman rules, and `FORM` [219,220] for the calculation of the Dirac and color traces [221]. We adopt anticommuting γ_5 throughout the calculation; this is justified, because all traces contain an even number of γ_5 (see Ref. [210]). The resulting scalar integrals are then reduced to the one and six master integrals of Ref. [213] at one and two loops, respectively, by solving integration-by-parts identities [201,222–224] with `Kira⊗FireFly` [225–228].

C. Results

The results for ζ_1 have already been presented in Ref. [210] through NNLO. We reevaluated the matrix as a check for our calculation of ζ_2 and include them here for the sake of completeness. For convenience of the reader, we quote the results for the inverse matching matrix rather than the matrix itself, as it is this quantity that is required to relate the lattice matrix elements to the perturbative matching coefficient; cf. Eq. (29). We use the definitions

$$\begin{aligned}\zeta(2) = \mathrm{Li}_2(1) &= \frac{\pi^2}{6} = 1.64493\ldots \\ \mathrm{Li}_2(1/4) &= 0.267652\ldots,\end{aligned} \tag{42}$$

where $\mathrm{Li}_2(z) = \sum_{k=1}^{\infty} z^k/k^2$ is the dilogarithm. The flowed quark fields are renormalized in the ringed scheme, and we define the evanescent operators as in Sec. IV A. Furthermore, we denote the number of quark flavors by n_f, and define $a_\mathrm{s}(\mu) = \frac{g^2(\mu)}{4\pi^2}$ with $g(\mu)$ the strong coupling in the $\overline{\mathrm{MS}}$ scheme. The coefficient $c_\chi^{(2)}$ appearing in the results arises from the conversion to the ringed scheme and is only known numerically; its value can be found in Eqs. (A17) and (A18). The matching coefficients depend on

$$L_{\mu\tau} = \ln 2\mu^2\tau + \gamma_\mathrm{E}, \tag{43}$$

with $\gamma_\mathrm{E} = 0.577215\ldots$ being the Euler-Mascheroni constant.

Finally, for $i = 1$, we find[7]

$$\begin{aligned}
(\zeta_1^{-1})_{11} &= 1 + a_\mathrm{s}\left(-\frac{1}{3}+\frac{8}{3}\ln 2 + 2\ln 3\right) + a_\mathrm{s}^2\left\{-\frac{1}{8}c_\chi^{(2)} + \frac{2413}{144} - \frac{35}{72}n_\mathrm{f} + \left(\frac{119}{72} - \frac{1}{6}n_\mathrm{f}\right)\zeta(2) + \frac{70}{3}\ln 2\right. \\
&\quad + \frac{22}{9}\ln^2 2 + 8\ln 2\ln 3 - \frac{83}{3}\ln 3 + 3\ln^2 3 - \frac{107}{6}\mathrm{Li}_2(1/4) \\
&\quad \left. + L_{\mu\tau}\left[-\frac{3}{8}+\frac{1}{18}n_\mathrm{f} + \left(\frac{22}{3}-\frac{4}{9}n_\mathrm{f}\right)\ln 2 + \left(\frac{11}{2}-\frac{1}{3}n_\mathrm{f}\right)\ln 3\right] + \frac{1}{4}L_{\mu\tau}^2\right\} + \mathcal{O}(a_\mathrm{s}^3), \\
(\zeta_1^{-1})_{12} &= -a_\mathrm{s}\left(\frac{3}{4}+\frac{3}{2}L_{\mu\tau}\right) + a_\mathrm{s}^2\left\{-\frac{301}{48} + \frac{133}{288}n_\mathrm{f} + \left(-\frac{67}{96}+\frac{1}{8}n_\mathrm{f}\right)\zeta(2) - \frac{451}{24}\ln 2 + \frac{201}{16}\ln 3 - \frac{27}{16}\mathrm{Li}_2(1/4)\right. \\
&\quad \left. + L_{\mu\tau}\left[-\frac{245}{32}+\frac{5}{12}n_\mathrm{f} - 4\ln 2 - 3\ln 3\right] + L_{\mu\tau}^2\left[-\frac{39}{16}+\frac{1}{8}n_\mathrm{f}\right]\right\} + \mathcal{O}(a_\mathrm{s}^3), \\
(\zeta_1^{-1})_{21} &= -a_\mathrm{s}\left(\frac{1}{6}+\frac{1}{3}L_{\mu\tau}\right) + a_\mathrm{s}^2\left\{-\frac{733}{216} + \frac{133}{1296}n_\mathrm{f} + \left(-\frac{67}{432}+\frac{1}{36}n_\mathrm{f}\right)\zeta(2) - \frac{451}{108}\ln 2 + \frac{67}{24}\ln 3 - \frac{3}{8}\mathrm{Li}_2(1/4)\right. \\
&\quad \left. + L_{\mu\tau}\left[-\frac{317}{144}+\frac{5}{54}n_\mathrm{f} - \frac{8}{9}\ln 2 - \frac{2}{3}\ln 3\right] + L_{\mu\tau}^2\left[-\frac{13}{24}+\frac{1}{36}n_\mathrm{f}\right]\right\} + \mathcal{O}(a_\mathrm{s}^3),
\end{aligned}$$

[6]We recently replaced `q2e` [216,217] by `tapir` [218]; in fact, we used this project to check our implementation of `tapir` against the `q2e` version.

[7]The results of Ref. [210] are equivalent to ours, even though the choice of basis is slightly different. The difference amounts to the choice of $B_{1,0}$ and $B_{2,0}$ as defined in Eqs. (B3) and (B4). This choice does not impact the physical part of the matching matrix though (see Appendix B).

$$(\zeta_1^{-1})_{22} = 1 + a_s\left(\frac{17}{12}+\frac{8}{3}\ln 2 + 2\ln 3 + \frac{1}{2}L_{\mu\tau}\right) + a_s^2\left\{-\frac{1}{8}c_\chi^{(2)} + \frac{6913}{288} - \frac{625}{864}n_f + \left(\frac{181}{96}-\frac{5}{24}n_f\right)\zeta(2) + \frac{2419}{72}\ln 2 + \frac{22}{9}\ln^2 2 + 8\ln 2\ln 3 - \frac{1385}{48}\ln 3 + 3\ln^2 3 - \frac{829}{48}\mathrm{Li}_2(1/4) + L_{\mu\tau}\left[\frac{281}{96}-\frac{1}{12}n_f + \left(\frac{26}{3}-\frac{4}{9}n_f\right)\ln 2 + \left(\frac{13}{2}-\frac{1}{3}n_f\right)\ln 3\right] + L_{\mu\tau}^2\left[\frac{17}{16}-\frac{1}{24}n_f\right]\right\} + \mathcal{O}(a_s^3), \tag{44}$$

and for $i = 2$

$$(\zeta_2^{-1})_{11} = 1 + a_s\left(\frac{4}{3}+\frac{8}{3}\ln 2 + 2\ln 3 + 2L_{\mu\tau}\right) + a_s^2\left\{-\frac{1}{8}c_\chi^{(2)} + \frac{2291}{72} - \frac{10}{9}n_f + \left(\frac{7}{4}-\frac{1}{3}n_f\right)\zeta(2) + \frac{143}{3}\ln 2 + \frac{22}{9}\ln^2 2 + 8\ln 2\ln 3 - \frac{251}{6}\ln 3 + 3\ln^2 3 - \frac{47}{2}\mathrm{Li}_2(1/4) + L_{\mu\tau}\left[\frac{29}{2}-\frac{1}{2}n_f + \left(\frac{38}{3}-\frac{4}{9}n_f\right)\ln 2 + \left(\frac{19}{2}-\frac{1}{3}n_f\right)\ln 3\right] + L_{\mu\tau}^2\left[\frac{19}{4}-\frac{1}{6}n_f\right]\right\} + \mathcal{O}(a_s^3),$$

$$(\zeta_2^{-1})_{12} = \frac{1}{2}a_s + a_s^2\left\{\frac{17}{192}-\frac{1}{144}n_f + \frac{5}{96}\zeta(2) + \frac{77}{24}\ln 2 + \frac{1}{16}\ln 3 - \frac{25}{16}\mathrm{Li}_2(1/4) - \frac{19}{32}L_{\mu\tau}\right\} + \mathcal{O}(a_s^3),$$

$$(\zeta_2^{-1})_{21} = \frac{1}{9}a_s + a_s^2\left\{-\frac{91}{864}-\frac{1}{648}n_f + \frac{5}{432}\zeta(2) + \frac{77}{108}\ln 2 + \frac{1}{72}\ln 3 - \frac{25}{72}\mathrm{Li}_2(1/4) + \frac{17}{144}L_{\mu\tau}\right\} + \mathcal{O}(a_s^3),$$

$$(\zeta_2^{-1})_{22} = 1 + a_s\left(\frac{19}{24}+\frac{8}{3}\ln 2 + 2\ln 3 - \frac{1}{4}L_{\mu\tau}\right) + a_s^2\left\{-\frac{1}{8}c_\chi^{(2)} + \frac{21223}{1152} - \frac{845}{1728}n_f + \left(\frac{935}{576}-\frac{7}{48}n_f\right)\zeta(2) + \frac{209}{9}\ln 2 + \frac{22}{9}\ln^2 2 + 8\ln 2\ln 3 - \frac{275}{12}\ln 3 + 3\ln^2 3 - \frac{797}{48}\mathrm{Li}_2(1/4) + L_{\mu\tau}\left[-\frac{427}{192}+\frac{1}{8}n_f + \left(\frac{20}{3}-\frac{4}{9}n_f\right)\ln 2 + \left(5-\frac{1}{3}n_f\right)\ln 3\right] + L_{\mu\tau}^2\left[-\frac{5}{16}+\frac{1}{48}n_f\right]\right\} + \mathcal{O}(a_s^3). \tag{45}$$

Note that the NLO result for both ζ_1^{-1} and ζ_2^{-1} was recently obtained in Ref. [229] using the 't Hooft-Veltman scheme for γ_5. A direct comparison is not possible without a dedicated calculation.

In principle, ζ_{11}^{-1} is both an element of the matching matrix for the $\Delta Q = 0$ operators of Eq. (18), as well as the matching coefficient for the only relevant $\Delta Q = 2$ operator given in Eq. (5). However, for the latter case, it is more common to define [205,230]

$$\mathcal{Q}_\pm = \frac{1}{2}(\mathcal{Q}_1 \pm \mathcal{Q}_2), \tag{46}$$

with $\mathcal{Q}_1$ from Eq. (5), and

$$\mathcal{Q}_2 = (\bar{Q}^i\gamma_\mu(1-\gamma_5)q^j)(\bar{q}^j\gamma^\mu(1-\gamma_5)Q^i) = 2(\bar{Q}\gamma_\mu(1-\gamma_5)T^Aq)(\bar{q}\gamma^\mu(1-\gamma_5)T^AQ) + \frac{1}{N_c}\mathcal{Q}_1, \tag{47}$$

where i, j are color indices, and we used the SU(N_c) identity

$$T^A_{ij}T^A_{kl} = \frac{1}{2}\left(\delta_{il}\delta_{jk} - \frac{1}{N_c}\delta_{ij}\delta_{kl}\right). \tag{48}$$

In $D = 4$ space-time dimensions, it is $\mathcal{Q}_1 = \mathcal{Q}_2 = \mathcal{Q}_+$ due to Fierz identities, while $\mathcal{Q}_-$ is evanescent. This also implies $\tilde{\mathcal{Q}}_1 = \tilde{\mathcal{Q}}_+$, since flowed operators are UV finite. Nevertheless, this change of basis affects the higher orders in the matching relation, which we now write as

$$\mathcal{Q}_+^{\overline{\mathrm{MS}}} = \zeta_{++}^{-1}\tilde{\mathcal{Q}}_+ = \zeta_{++}^{-1}\tilde{\mathcal{Q}}_1. \tag{49}$$

Choosing this nonmixing basis, corresponding to the evanescent operators of Eq. (B5), we find

$$\zeta_{++}^{-1} = 1 + a_s\left(-\frac{5}{4}+\frac{8}{3}\ln 2 + 2\ln 3 - \frac{1}{2}L_{\mu\tau}\right) + a_s^2\left\{-\frac{1}{8}c_\chi^{(2)} + \frac{62527}{3600} - \frac{85}{288}n_f + \left(\frac{409}{288}-\frac{1}{8}n_f\right)\zeta(2) + \frac{367}{24}\ln 2 + \frac{22}{9}\ln^2 2 + 8\ln 2\ln 3 - \frac{397}{16}\ln 3 + 3\ln^2 3 - \frac{883}{48}\mathrm{Li}_2(1/4) + L_{\mu\tau}\left[-\frac{83}{32}+\frac{7}{36}n_f + \left(6-\frac{4}{9}n_f\right)\ln 2 + \left(\frac{9}{2}-\frac{1}{3}n_f\right)\ln 3\right] + L_{\mu\tau}^2\left[-\frac{9}{16}+\frac{1}{24}n_f\right]\right\} + \mathcal{O}(a_s^3). \quad (50)$$

In Ref. [231] the NLO result was obtained within the dimensional-reduction scheme for γ_5; direct comparison requires further calculation beyond the scope of this work.

The calculation of all the matching coefficients has been carried out in general R_ξ gauge, the independence of the final result on the gauge parameter ξ providing a strong check. The full result including the dependence on the choice of evanescent operators is provided in the ancillary file; see Appendix C and Ref. [209].

V. FLOWED MATRIX ELEMENTS

In this section, we describe the evaluation of the flowed matrix elements required for the calculation of the bag parameters.

A. Simulation details

Our work is based on six ensembles of gauge field configurations generated by the RBC/UKQCD Collaboration [232–235]. These $2+1$ flavor ensembles feature the effect of degenerate up/down (light) and strange quarks in the sea sector, and simulations are performed using the Iwasaki gauge action [236] and Shamir domain-wall fermions (DWF) [237–239]. Details of the ensembles are summarized in Table I.

In the valence sector, we simulate strange quarks using the same DWF action as in the sea sector, but set the bare mass to its physical value determined in Refs. [234,235]. For charm quarks, we use stout-smeared [240] Möbius DWF [241] optimized for simulating heavy flavors [242]. We tune the bare charm quark mass to its physical value using the mass of the D_s pseudoscalar meson [114] and a^{-1} from Refs. [234,235].

The setup for our measurements is inspired by the determination of bag parameters for neutral B-meson mixing [235]. All propagators are generated with $\mathbb{Z}_2$ wall sources and we choose an equal-time separation for N_{src} source positions as specified in Table I. We suppress excited states by applying iterative Gaussian smearing [243] to strange quark sources using a width σ and N_σ iterations.

The evolution of gauge and propagator fields is performed using a third-order Runge-Kutta algorithm with step size $\delta\tau/a^2 = 0.01$ [33,34]. Flowed fields are contracted into two- and three-point correlation functions, initially every ten steps and later every 40 steps. The maximum flow times in lattice units are set such that all ensembles are flowed by the same physical distance.

The construction of three-point functions is shown by the quark-line diagrams in Figs. 4 and 5 where the pseudoscalar meson states are placed at Euclidean times t_0 and $t_0 + \Delta T$. We contract the four-quark operators at all times $t \in [t_0, t_0 + \Delta T]$. To study the dependence of the signal on the separation of both sources, we perform contractions for multiple choices of ΔT up to half the temporal extent of the lattice.

We use the `Grid` [244] and `Hadrons` [245,246] lattice QCD software libraries to carry out our measurements. The gradient-flow evolution of both the gauge and propagator

TABLE I. RBC/UKQCD's $N_f = 2+1$ Shamir DWF ensembles with Iwasaki gauge action [232–235] characterized by inverse lattice spacing (a^{-1}), unitary pion mass (M_π), sea strange (am_s^{val}), valence strange (am_s^{val}), and charm (am_c) quark masses. We use two coarse (C1, C2), three medium (M1, M2, M3), and one fine ensemble (F1S). The Jacobi smearing procedure is applied on the C and M ensembles with smearing width σ and N_σ iterations. ΔT_{min} indicates the minimum source separation ΔT considered to have sufficient resolution of the ground state.

	L/a	T/a	a^{-1} [GeV]	M_π [MeV]	am_s^{sea}	am_s^{val}	am_c	$N_{\mathrm{src}} \times \mathrm{N_{conf}}$	σ	N_σ	ΔT_{min}
C1	24	64	1.7848(50)	339.8(1.2)	0.04	0.03224	0.64	32×101	4.5	400	20
C2	24	64	1.7848(50)	430.6(1.4)	0.04	0.03224	0.64	32×101	4.5	400	20
M1	32	64	2.3833(86)	303.6(1.4)	0.03	0.02477	0.45	32×79	6.5	400	22
M2	32	64	2.3833(86)	360.7(1.6)	0.03	0.02477	0.45	32×89	6.5	100	22
M3	32	64	2.3833(86)	410.8(1.7)	0.03	0.02477	0.45	32×68	6.5	100	22
F1S	48	96	2.785(11)	267.6(1.3)	0.02144	0.02167	0.37	24×98			28

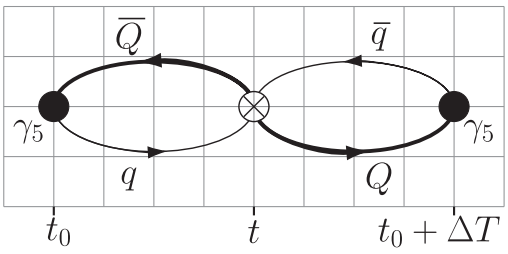


FIG. 4. Quark-line diagram to calculate $\Delta Q = 2$ operators on the lattice for neutral meson mixing.

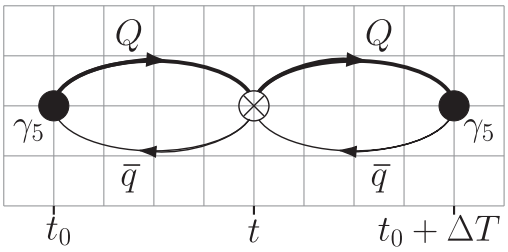


FIG. 5. Quark-line diagrams to calculate $\Delta Q = 0$ operators on the lattice for valence-quark contributions to lifetimes.

fields is implemented in new `Hadrons` modules[8] including an example run application.[9]

Instead of working with the operators defined in Eq. (18), it is more convenient to use a basis for the lattice simulations where the quark pairs on each spin line are color singlets:

$$\begin{aligned}
\mathcal{O}_1 &= (\bar{Q}\gamma_\mu(1-\gamma_5)q)(\bar{q}\gamma_\mu(1-\gamma_5)Q),\\
\mathcal{O}_2 &= (\bar{Q}(1-\gamma_5)q)(\bar{q}(1+\gamma_5)Q),\\
\mathcal{T}_1 &= (\bar{Q}\gamma_\mu(1-\gamma_5)Q)(\bar{q}\gamma_\mu(1-\gamma_5)q),\\
\mathcal{T}_2 &= (\bar{Q}\gamma_\mu(1+\gamma_5)Q)(\bar{q}\gamma_\mu(1-\gamma_5)q).
\end{aligned} \tag{51}$$

Through Eq. (48), they are related to the operators defined in Eq. (18) via

$$\begin{pmatrix} \mathcal{O}_1 \\ \mathcal{O}_2 \\ T_1 \\ T_2 \end{pmatrix} = \begin{pmatrix} 1 & 0 & 0 & 0 \\ 0 & 1 & 0 & 0 \\ -\frac{1}{2N_c} & 0 & -\frac{1}{2} & 0 \\ 0 & -\frac{1}{2N_c} & 0 & \frac{1}{4} \end{pmatrix} \begin{pmatrix} \mathcal{O}_1 \\ \mathcal{O}_2 \\ \mathcal{T}_1 \\ \mathcal{T}_2 \end{pmatrix}. \tag{52}$$

Furthermore, since QCD is parity invariant, we are only interested in the parity-even components of these operators, i.e. the terms that involve an even number of γ_5 matrices. While the basis of Eq. (51) is used in the simulations, we only show results that have been converted back to the bases defined in Eq. (18).

[8]https://github.com/aportelli/Hadrons/pull/137.
[9]https://github.com/mbr-phys/HeavyMesonLifetimes.

VI. DATA ANALYSIS

In the following, we will provide a detailed description of our analysis strategy. In order to test the coherence and reliability of our framework, all numerical analyses described below have been performed using two independent setups: one based on the bootstrap procedure [247], and the other based on the Γ method [248–252]. Both analyses lead to consistent results.

A. Correlator fits

While the matrix elements of four-quark operators themselves can be extracted from the three-point correlation functions, the bag parameters can be extracted by comparing the matrix element to its VIA using the ratio of the three-point function over two two-point functions which individually yield the bilinear matrix elements of the VIA for each operator. We thus form ratios of correlation functions for each flow time τ, reading

$$\begin{aligned}
R_X(t_0, t, \Delta T; \tau) &= \frac{C_X^{\mathrm{3pt}}(t_0, t, t_0 + \Delta T; \tau)}{\eta_X C_X(t_0, t; \tau) C_X(t_0 + \Delta T, t; \tau)} \\
&\to \tilde{B}_X(\tau),
\end{aligned} \tag{53}$$

where the arrow indicates the limits $t_0 \ll t \ll t_0 + \Delta T$ and $\Delta T \to \infty$. The flowed two- and three-point functions are given by

$$\begin{aligned}
C_X^{\mathrm{3pt}}(t_1, t_2, t_3; \tau) &= \langle 0 | j_P(t_1) \tilde{X}(t_2; \tau) j_P^\dagger(t_3) | 0 \rangle, \\
C_X(t_1, t_2; \tau) &= \langle 0 | \tilde{j}_X(t_2; \tau) j_P^\dagger(t_1) | 0 \rangle,
\end{aligned} \tag{54}$$

where $t_1 < t_2 < t_3$ are generic positions, and $j_P = \bar{q}\gamma_5 Q$ and $j_X = \bar{q}\Gamma_X Q$ are zero-momentum currents. Note that we are using X both as an operator and as a subscript in Eq. (54). The associated Dirac structures are $\Gamma_{\mathcal{Q}_1} = \Gamma_{\mathcal{O}_1} = \Gamma_{T_1} = \gamma_0\gamma_5$, and $\Gamma_{\mathcal{O}_2} = \Gamma_{T_2} = \gamma_5$. Furthermore, we use the notation $B_i = B_{\mathcal{O}_i}, \epsilon_i = B_{T_i}$. The normalization factor η_X is given as $\eta_{\mathcal{Q}_1} = 8/3$ and $\eta_{\mathcal{O}_i} = \eta_{T_i} = 1$. In all cases, the gradient-flow evolution is applied only at the sink operator. As discussed in the context of Eq. (27), the flowed-quark wave function renormalization $\mathring{Z}_\chi$ cancels in the ratios of Eq. (53), and thus the bag parameters extracted at $\tau > 0$ are UV finite without any additional renormalization.

In the limit of large Euclidean time separation between sources, these ratios will reach a plateau corresponding to the value of the flowed bag parameter of their inserted operator. For each flow time, we use Eq. (53) to extract ground state values of our ratios by performing correlated, simultaneous fits to all separations $\Delta T \geq \Delta T_{\mathrm{min}}$ (listed in Table I). Excited states are not statistically resolved.

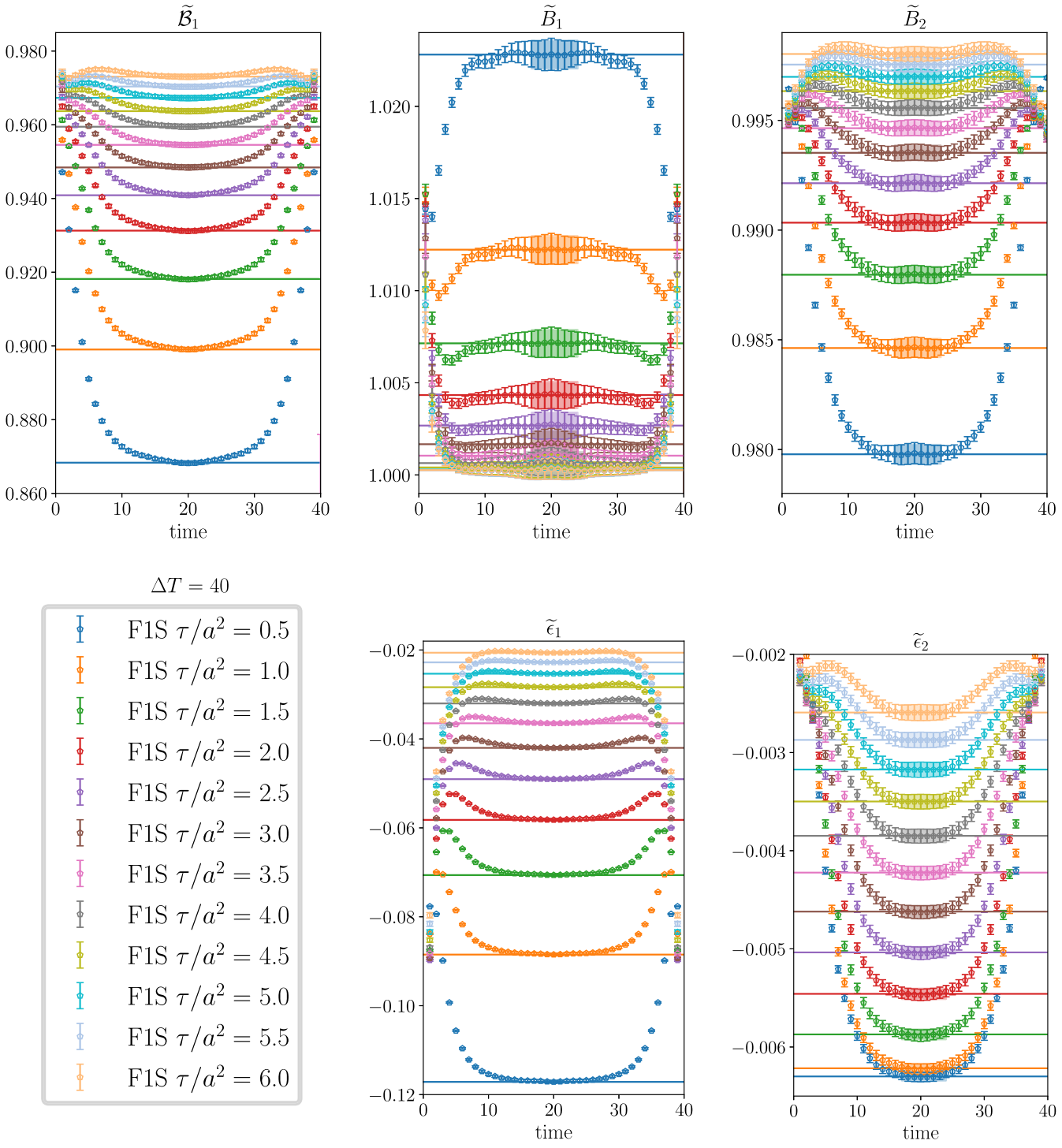


FIG. 6. Example fits to the ratio R_X [Eq. (53)] extracting the different bag parameters at various flow times on the F1S ensemble for fixed $\Delta T = 40$.

Examples of the ratio fits at various flow times for each operator are shown in Fig. 6. The flow-time evolutions of the fitted bag parameters are shown in Fig. 7 where the data are plotted first as a function of the lattice flow time τ/a^2 on the left and then in physical flow time [GeV^{-2}] on the right. We see that as the operators are evolved along the gradient flow, the data from different ensembles quickly converge to lie on top of each other at the same physical flow time.

B. Continuum limits

In order to take a continuum limit at fixed values of the flow time in physical units, we first linearly interpolate the

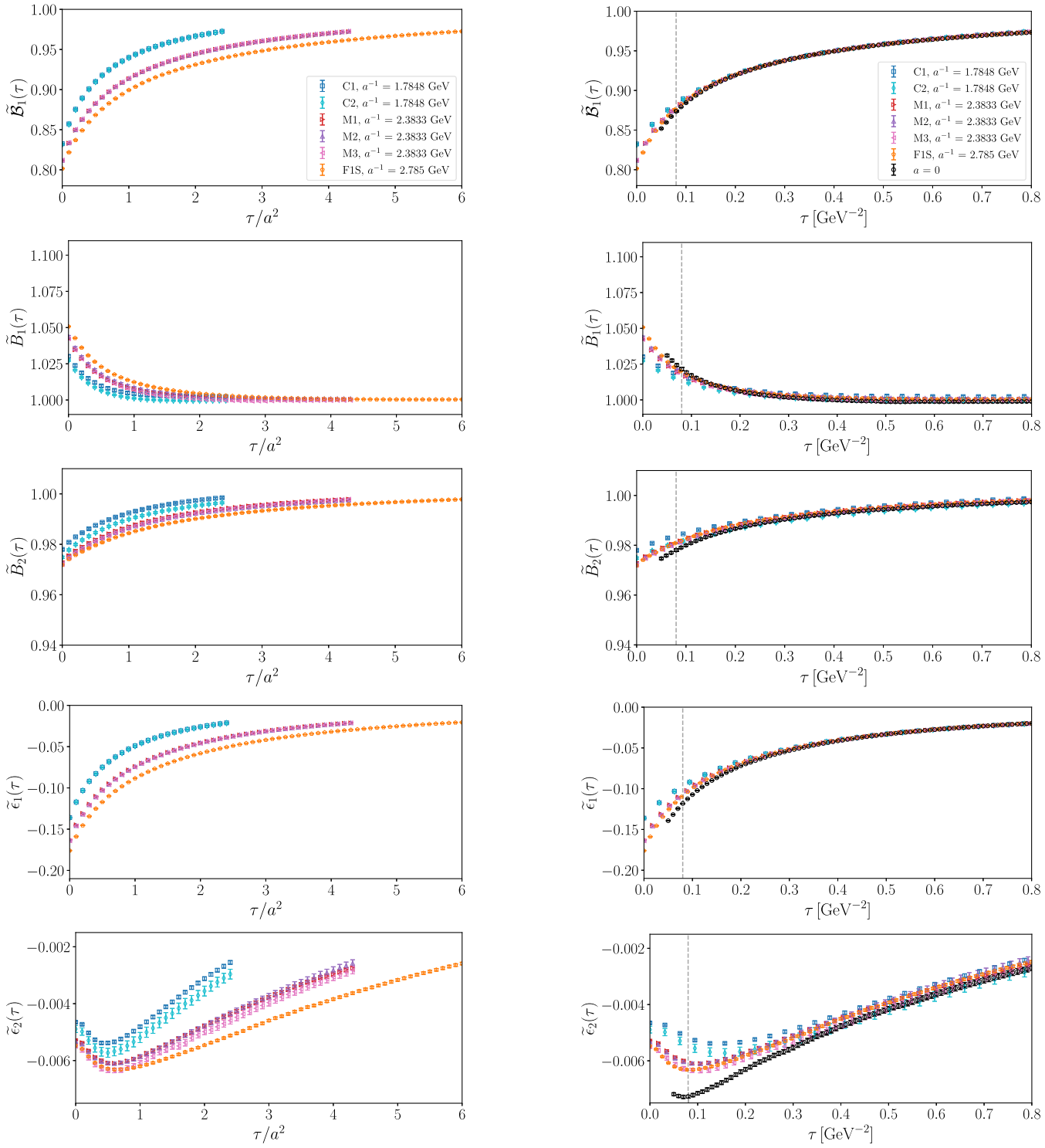


FIG. 7. Flow-time evolution of the bag parameters. The panels on the left show the bag parameters in lattice units τ/a^2, whereas we show the conversion to physical units $\tau[\mathrm{GeV}^{-2}]$ in the right panels. The dashed gray lines indicate τ_{min}, the minimum flow time for which the continuum limit is considered reliable, defined relative to our coarsest lattice spacing.

values on each ensemble to a common set of flow times $\tau_{\text{phys}} = \{0.01, 0.02, \ldots, 0.80\}$.[10] The continuum limit is then taken at all values τ_{phys}, but the $a \to 0$ extrapolation is reliable only for a sufficiently large "smearing radius" $\sqrt{8\tau}$ as discussed in Sec. III B. We find that a suitable choice is $8\tau > 2a_{\text{max}}^2$, where a_{max} is the coarsest lattice spacing in the analysis. In practice, this translates to $\tau \gtrsim \tau_{\text{min}} \equiv 0.08\ \text{GeV}^{-2}$. Smaller values of τ are considered only in order to check for possible systematic effects. For increasing values of $\tau > \tau_{\text{min}}$, the continuum-limit extrapolations quickly become very flat, which may also be attributed to the use of DWF. For our choice of lattice actions, discretization effects are expected to appear at $O(a^2)$.[11] Therefore, we choose a linear ansatz in a^2 to perform the $a \to 0$ extrapolation. Although we study only charm-strange mesons, we observe that small differences due to different pion masses in the sea sector are resolved. We therefore parametrize the pion-mass dependence in a chiral-continuum limit using the ansatz

$$\tilde{B}_i^{\text{latt}}(a^2, M_\pi^{\text{latt}}; \tau) = \tilde{B}_i(\tau) + Ca^2 + Da^2[(M_\pi^{\text{latt}})^2 - (M_\pi^{\text{phys}})^2], \quad (55)$$

where $\tilde{B}_i^{\text{latt}}(a^2, M_\pi^{\text{latt}}; \tau)$ are the bag parameters extracted on each ensemble from Eq. (53), $\tilde{B}_i(\tau)$ denotes the extrapolated estimator in the continuum limit at the physical pion mass, M_π^{phys} [114], while C and D are dimensionful fit parameters describing the leading discretization effects and their dependence on the sea-pion mass, M_π^{latt}, which is in physical units. Example chiral-continuum limits at fixed flow times are shown in Figs. 8 and 9.

We then define the SFTX at the level of the bag parameters, i.e.

$$\mathcal{B}_1(\tau, \mu) = \zeta_{\mathcal{B}_1}^{-1}(\tau, \mu)\tilde{\mathcal{B}}_1(\tau) \quad (56)$$

for the mixing, and

$$\begin{pmatrix} B_1(\tau,\mu) \\ \epsilon_1(\tau,\mu) \end{pmatrix} = \zeta_{B,1}^{-1}(\tau,\mu) \begin{pmatrix} \tilde{B}_1(\tau) \\ \tilde{\epsilon}_1(\tau) \end{pmatrix},$$
$$\begin{pmatrix} B_2(\tau,\mu) \\ \epsilon_2(\tau,\mu) \end{pmatrix} = \zeta_{B,2}^{-1}(\tau,\mu) \begin{pmatrix} \tilde{B}_2(\tau) \\ \tilde{\epsilon}_2(\tau) \end{pmatrix}, \quad (57)$$

for the lifetimes, where $\tilde{\mathcal{B}}_1(\tau)$, $\tilde{B}_i(\tau)$, and $\tilde{\epsilon}_i(\tau)$ represent the continuum-extrapolated bag parameters from the lattice data. The corresponding matching matrices are given by

[10]The flow time is technically a continuous variable and any choice of physical flow times is equally valid.

[11]The fermionic gradient flow is classically $O(a)$ improved and does not introduce relevant discretization effects beyond those from the 4D theory for $\tau \gtrsim \tau_{\text{min}}$.

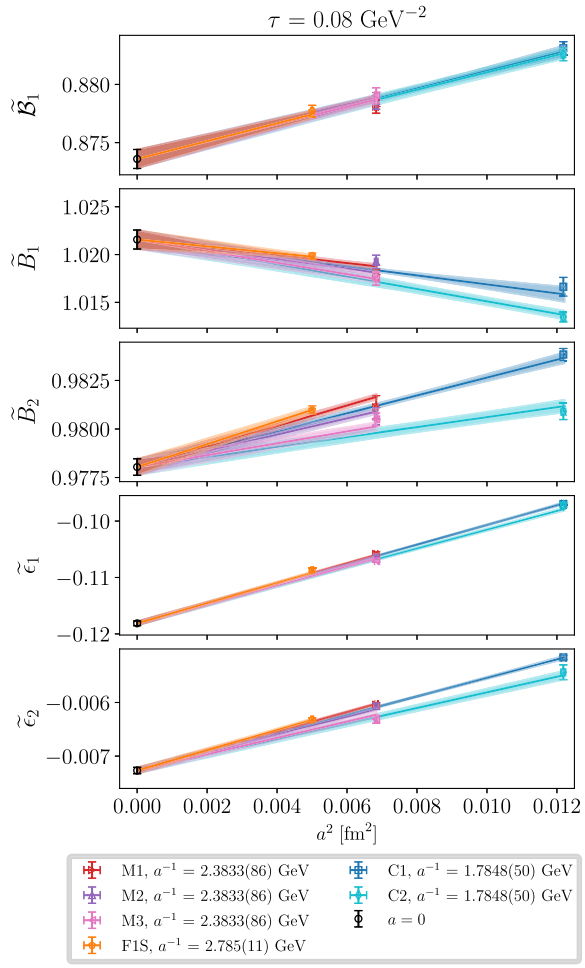


FIG. 8. Chiral-continuum limit fits for each bag parameter at $\tau = 0.08\,\text{GeV}^{-2}$. The black data point is the continuum-extrapolated value at physical pion mass, and the colored bands are the linear a^2 relations at each ensemble's pion mass after fitting to Eq. (55).

$$\zeta_{\mathcal{B},1} = \zeta_{++}\zeta_A^{-2}, \qquad \zeta_{B,1} = \zeta_1\zeta_A^{-2}, \qquad \zeta_{B,2} = \zeta_2\zeta_P^{-2}, \quad (58)$$

with ζ_1, ζ_2, and ζ_{++} evaluated in Sec. IV and provided explicitly in Eqs. (44), (45), and (50). Finally, ζ_P and ζ_A are the SFTX matching coefficients for the pseudoscalar and the axial-vector currents, which are available through NNLO QCD [253–255].

VII. ZERO-FLOW-TIME EXTRAPOLATION

Throughout this paper, we use $\alpha_s(M_Z) = 0.1180$ [114] as input and evolve it down to $\alpha_s(\mu = 3\ \text{GeV}) = 0.2535$ at five-loop level, decoupling the bottom quark at $\mu = m_b$ at four-loop level. For any further change of the renormalization scale, we evolve α_s to the corresponding perturbative order, i.e. one-loop running at NLO and two-loop running

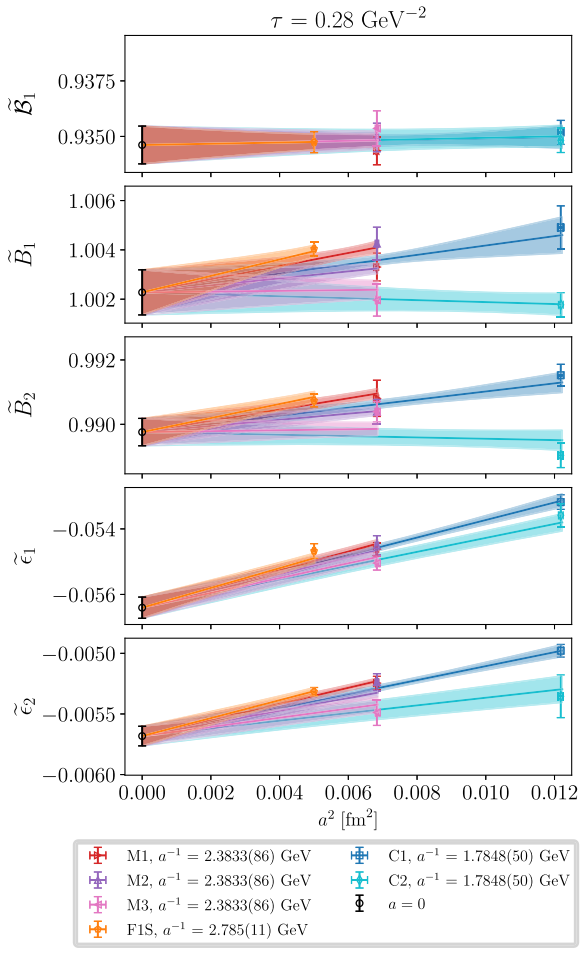


FIG. 9. Chiral-continuum limit fits for each bag parameter at $\tau = 0.28\,\mathrm{GeV}^{-2}$. The black data point is the continuum-extrapolated value at physical pion mass, and the colored bands are the linear a^2 relations at each ensemble's pion mass after fitting to Eq. (55).

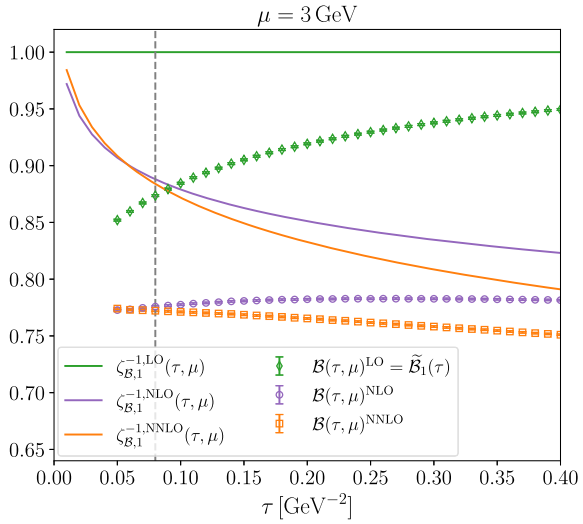


FIG. 10. SFTX-matched bag parameter $\mathcal{B}_1(\tau, \mu = 3\ \mathrm{GeV})$ at LO (green), NLO (purple), and NNLO (orange). The associated matching coefficents $\zeta^{-1}_{\mathcal{B},1}$ are plotted in solid lines, where the LO matching is 1, and the NLO and NNLO matching coefficients are given by Eq. (50). The dashed line at $\tau = 0.08$ GeV^{-2} indicates the appropriate τ_{min} for our dataset.

at NNLO. All of these operations are done with the help of `RunDec` [256,257].[12]

A. Fixed perturbative order

The SFTX-matched bag parameters of Eqs. (56) and (57) —which still depend on both the renormalization scale μ and the flow time τ—are related to the $\overline{\mathrm{MS}}$ bag parameters by taking the $\tau \to 0$ extrapolation, i.e.

$$\mathcal{B}_1^{\overline{\mathrm{MS}}}(\mu) = \lim_{\tau \to 0} \mathcal{B}_1(\tau, \mu), \tag{59}$$

and similarly for the lifetime bag parameters B_i, ϵ_i. The limit of $\tau \to 0$ is not trivial and involves identifying the correct region from which such an extrapolation can be performed which takes into account the constraints outlined in Sec. III B. Figure 10 illustrates the situation for the example of the mixing bag parameter $\mathcal{B}_1$ by displaying the individual terms of Eq. (56). The markers show data for $\mathcal{B}_1(\tau, \mu)$ obtained by using the matching coefficient $\zeta^{-1}_{\mathcal{B},1}$ at LO (green diamonds), NLO (purple circles), and NNLO (orange squares). Since $\zeta^{-1,\mathrm{LO}}_{\mathcal{B},1} = 1$, the green diamonds are equivalent to the pure lattice data $\tilde{\mathcal{B}}_1(\tau)$.

The matching coefficients are also shown separately as solid curves. They suggest reliable perturbative convergence over the full τ range of the figure, with the NLO corrections amounting to less than 20%, and the NNLO effects adding less than another $\pm 5\%$. At first sight, this might seem remarkable considering that the flow time reaches up to relatively large values. However, it is important to note that we perform the matching at $\mu = 3$ GeV, which sets the scale for the strong coupling $\alpha_s(\mu)$, while the flow time occurs only via $L_{\mu\tau}$; cf. Eq. (43). At $\mu = 3$ GeV and $\tau = 0.4$ GeV^{-2}, its numerical value is $L_{\mu\tau} \approx 2.55$, which apparently is sufficiently small for the matching coefficients to remain perturbatively stable.

The plot clearly exhibits the basic features expected from the SFTX. While both the lattice data for $\tilde{\mathcal{B}}_1(\tau)$ as well as the higher-order matching coefficients are logarithmically divergent as $\tau \to 0$, these divergences formally cancel in the ratio $\mathcal{B}_1(\tau, \mu)$. Obviously, in practice this cancellation is incomplete due to the finite perturbative order of the matching coefficients as well as discretization effects when $\sqrt{8\tau} \lesssim a$. Nevertheless, the (partial) cancellation is effective over quite a large range of τ, resulting in an approximately linear behavior of $\mathcal{B}_1(\tau, \mu)$ in τ due to the truncation

[12] A Python wrapper for `RunDec` was also utilized, provided by https://github.com/DavidMStraub/rundec-python.

of these terms in the SFTX; see Eq. (29). Moreover, the NLO and NNLO values for $\mathcal{B}_1(\tau,\mu)$ are reasonably compatible within the displayed region of τ.

Based on these qualitative observations, it is the purpose of this section to work out a robust procedure for the extrapolation of the quantities defined in Eqs. (56) and (57) to $\tau = 0$ which reliably takes into account the possible sources of systematic uncertainties.

Our goal is to derive the bag parameters in the $\overline{\text{MS}}$ scheme at a certain reference value $\mu = \mu_0$. In principle, we can do this by inserting the (inverse) matching matrices at this value, $\zeta^{-1}(\tau,\mu_0)$, into Eqs. (56) and (57). However, it is equally valid to start from a different scale μ and evaluate the matching matrix at μ_0 according to its renormalization-group (RG) evolution:

$$\mu^2 \frac{\mathrm{d}}{\mathrm{d}\mu^2}\zeta(\tau,\mu) = \zeta(\tau,\mu)\gamma(\alpha_s(\mu)), \tag{60}$$

with γ the anomalous dimension in the $\overline{\text{MS}}$ scheme of B_X [205,258–260], provided in Appendix A. We denote the resulting matching matrix as $\zeta(\tau,\mu\to\mu_0)$. Different choices of the initial value of μ typically change the τ dependence of $\zeta^{-1}(\tau,\mu\to\mu_0)\tilde{B}(\tau)$, and therefore the $\tau\to 0$ limit, but critically not the value at $\tau = 0$ itself. Therefore we can better inform the $\tau\to 0$ limit by simultaneously fitting to data for multiple values of μ, where the flow-time dependence of each μ value can be parametrized separately. In practice, we choose $\mu_0 = 3$ GeV and set $n_f = 4$ as the number of active flavors at this scale. For the set of $\mu\in\{2.5, 3.0, 3.5, 4.0, 4.5\}$ GeV we then perform a combined $\tau\to 0$ extrapolation. Our final results for $\mathcal{B}_1(\mu_0)$, $B_i(\mu_0)$, and $\epsilon_i(\mu_0)$ are obtained by performing a single global fit to $B(\mu\to\mu_0)$ for all μ using the functional form

$$f(\tau,\mu) = c_0 + \tau(c_1^{(\mu)} + c_2^{(\mu)} \ln(\mu^2\tau)), \tag{61}$$

where the $c_{1,2}^{(\mu)}$ can be different for each value of μ, while c_0 is a parameter common to all fit functions. This ensures a solution for which the perturbative RG evolution is consistent across the chosen range of μ.

We evaluate all possible fit intervals fixing $\tau_{\text{min}} = 0.08\ \text{GeV}^{-2}$ (cf. Sec. VI B) and ranging up to at most $\tau_{\text{max}} = 0.4\ \text{GeV}^{-2}$, which is chosen to suppress $O(\tau)$ effects beyond the leading assumptions of the SFTX.[13] To further account for bias and/or systematic effects in the choice of τ_{min}, we repeat this procedure for minimum values $\tau_{\text{min}} + 0.01, 0.02, 0.03, 0.04\ \text{GeV}^{-2}$. The results are given by identifying the spread of all fit results for c_0 with p-value > 0.05 as the symmetrized uncertainty interval for the bag parameters at scale μ_0.

This interval accounts for both statistical and systematical uncertainties of the $\tau\to 0$ extrapolation, the latter arising from the finite perturbative order of the matching coefficients as well as the constraints on the allowed values of τ; see Sec. III B.

The $\tau\to 0$ extrapolations for the $\Delta Q = 2$ and $\Delta Q = 0$ operators are shown in Figs. 11 and 12 respectively. Next we discuss how we may improve upon this SFTX matching procedure by taking advantage of RG running.

B. Renormalization-group improvement

The dependence of the flowed operators on the flow time can be parametrized by the *flowed anomalous dimensions* $\tilde{\gamma}$, which allows for the resummation of their logarithmic τ dependence. They are defined in Ref. [261] as

$$\tau\frac{\mathrm{d}}{\mathrm{d}\tau}\tilde{\mathcal{O}}(\tau) = \tilde{\gamma}\,\tilde{\mathcal{O}}(\tau), \quad \text{with} \quad \tilde{\gamma} = \left(\tau\frac{\mathrm{d}}{\mathrm{d}\tau}\zeta\right)\zeta^{-1}. \tag{62}$$

For the operators in Eq. (18), we define the flow-time renormalization-group equation (RGE) as

$$\tau\frac{\mathrm{d}}{\mathrm{d}\tau}\begin{pmatrix}\tilde{\mathcal{O}}_i(\tau)\\ \tilde{T}_i(\tau)\end{pmatrix} = \tilde{\gamma}_i\begin{pmatrix}\tilde{\mathcal{O}}_i(\tau)\\ \tilde{T}_i(\tau)\end{pmatrix}, \qquad i\in\{1,2\}, \tag{63}$$

and then find the anomalous dimensions $\tilde{\gamma}_i$ to be

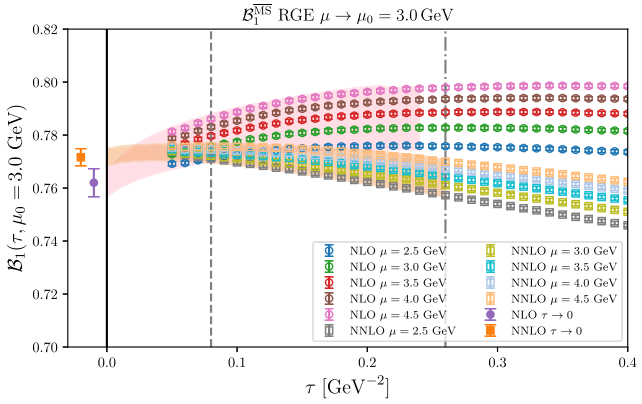


FIG. 11. Zero-flow-time extrapolation of the matched flow-time data for the $\Delta Q = 2$ $\mathcal{B}_1$ parameter. The matching to the $\overline{\text{MS}}$ scheme is performed at both NLO and NNLO using $\mu\in\{2.5, 3.0, 3.5, 4.0, 4.5\}$ GeV before running back to $\mu_0 = 3$ GeV. The pink and orange shaded areas indicate the spread of all acceptable fits to the data at NLO and NNLO, resulting in the purple and orange data points in the left panel respectively. The dashed line at $\tau = 0.08\ \text{GeV}^{-2}$ indicates the appropriate τ_{min} for our dataset, and the dot-dashed lines indicate the maximum flow time which enters the set of acceptable fits for each operator.

[13]The value of τ_{min} is a stricter limit than τ_{max} and is required by both the lattice spacings and the fixed-order perturbation theory used. Using finer lattice spacings and/or additional perturbative orders will push τ_{min} to smaller values.

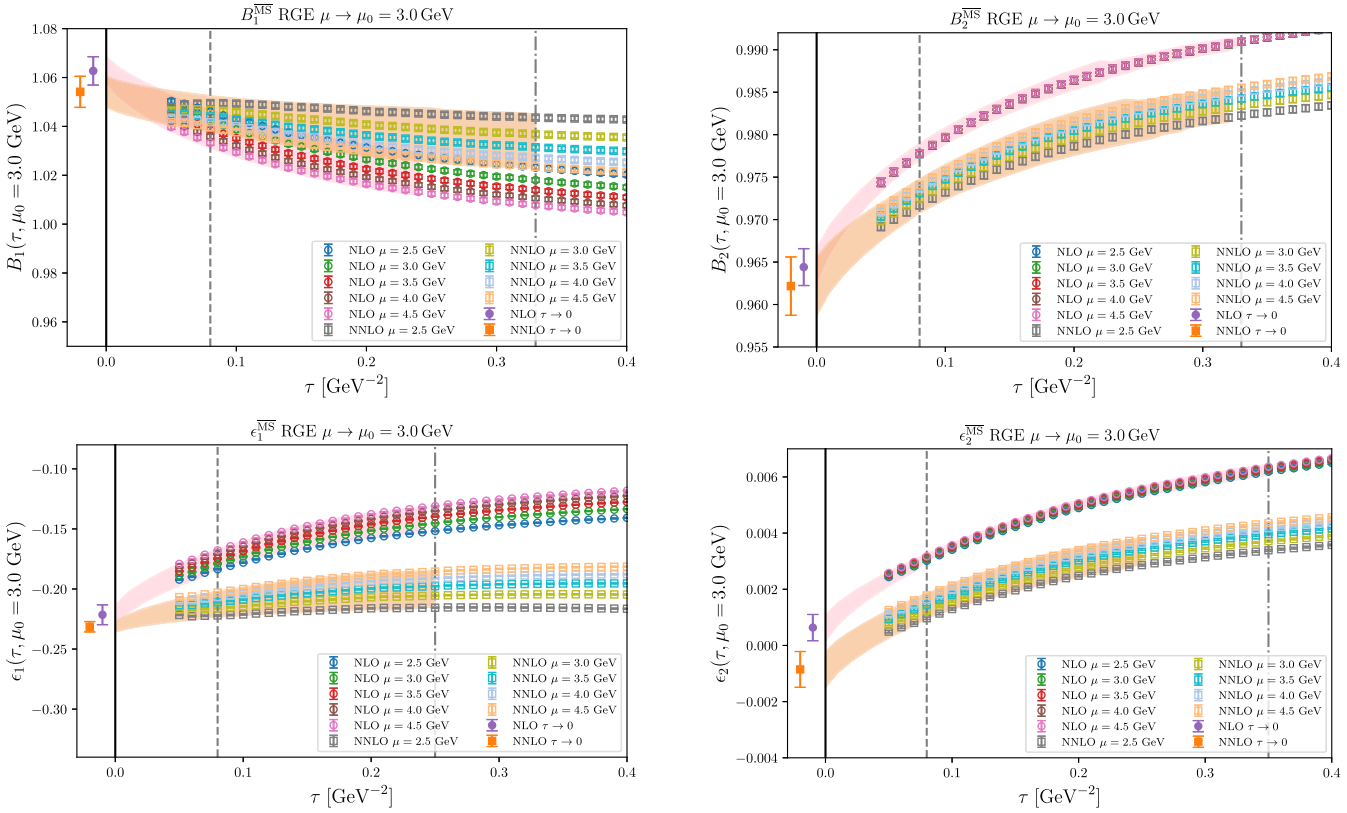


FIG. 12. Zero-flow-time extrapolations of the matched flow-time data for the $\Delta Q = 0$ bag parameters—B_1 (top left), B_2 (top right), ϵ_1 (bottom left), and ϵ_2 (bottom right). The matching to the $\overline{\rm MS}$ scheme is performed at both NLO and NNLO using $\mu \in \{2.5, 3.0, 3.5, 4.0, 4.5\}$ GeV before running back to $\mu_0 = 3$ GeV. The pink and orange shaded areas indicate the spread of all acceptable fits to the data at NLO and NNLO, resulting in the purple and orange data points in the left panel respectively. The dashed line at $\tau = 0.08$ GeV^{-2} indicates the appropriate $\tau_{\rm min}$ for our dataset, and the dot-dashed lines indicate the maximum flow time which enters the set of acceptable fits for each operator.

$$
\begin{aligned}
(\tilde{\gamma}_1)_{11} &= a_s^2\left[\frac{5}{8} - \frac{1}{18}n_f + \left(-\frac{22}{3} + \frac{4}{9}n_f\right)\ln 2\right. \\
&\quad \left. + \left(-\frac{11}{2} + \frac{1}{3}n_f\right)\ln 3\right] + \mathcal{O}(a_s^3), \\
(\tilde{\gamma}_1)_{12} &= \frac{3}{2}a_s + a_s^2\left[\frac{249}{32} - \frac{5}{12}n_f + \left(\frac{33}{8} - \frac{1}{4}n_f\right)L_{\mu\tau}\right] \\
&\quad + \mathcal{O}(a_s^3), \\
(\tilde{\gamma}_1)_{21} &= \frac{1}{3}a_s + a_s^2\left[\frac{83}{48} - \frac{5}{54}n_f + \left(\frac{11}{12} - \frac{1}{18}n_f\right)L_{\mu\tau}\right] \\
&\quad + \mathcal{O}(a_s^3), \\
(\tilde{\gamma}_1)_{22} &= -\frac{1}{2}a_s + a_s^2\left[-\frac{63}{32} + \frac{1}{12}n_f + \left(-\frac{22}{3} + \frac{4}{9}n_f\right)\ln 2\right. \\
&\quad + \left(-\frac{11}{2} + \frac{1}{3}n_f\right)\ln 3 \\
&\quad \left. + \left(-\frac{11}{8} + \frac{1}{12}n_f\right)L_{\mu\tau}\right] + \mathcal{O}(a_s^3),
\end{aligned} \tag{64}
$$

and

$$
\begin{aligned}
(\tilde{\gamma}_2)_{11} &= -2a_s + a_s^2\left[-\frac{71}{6} + \frac{1}{2}n_f + \left(-\frac{22}{3} + \frac{4}{9}n_f\right)\ln 2\right. \\
&\quad + \left(-\frac{11}{2} + \frac{1}{3}n_f\right)\ln 3 \\
&\quad \left. + \left(-\frac{11}{2} + \frac{1}{3}n_f\right)L_{\mu\tau}\right] + \mathcal{O}(a_s^3), \\
(\tilde{\gamma}_2)_{12} &= \frac{15}{32}a_s^2 + \mathcal{O}(a_s^3), \\
(\tilde{\gamma}_2)_{21} &= \frac{5}{48}a_s^2 + \mathcal{O}(a_s^3), \\
(\tilde{\gamma}_2)_{22} &= \frac{1}{4}a_s + a_s^2\left[\frac{389}{192} - \frac{1}{8}n_f + \left(-\frac{22}{3} + \frac{4}{9}n_f\right)\ln 2\right. \\
&\quad + \left(-\frac{11}{2} + \frac{1}{3}n_f\right)\ln 3 \\
&\quad \left. + \left(\frac{11}{16} - \frac{1}{24}n_f\right)L_{\mu\tau}\right] + \mathcal{O}(a_s^3).
\end{aligned} \tag{65}
$$

The dependence on the scheme of evanescent operators drops out in $\tilde{\gamma}$, which also means that the flowed anomalous dimension for the $\Delta Q = 2$ operator is $\tilde{\gamma}_{++} = \tilde{\gamma}_{11}$.

In the SFTX matching procedure used above, flow-time logarithms [Eq. (43)]—which are naturally present in both the all-orders nonperturbative lattice data and the fixed-order perturbative matching coefficients—will only cancel up to the available perturbative order. We therefore expect higher-order logarithms to manifest as curvature at smaller flow times in Figs. 11 and 12, and ultimately lead to divergences as $\tau \to 0$, which is one of the limiting factors in pushing $\tau_{\min}$ in our fits to smaller values; see Sec. III B. Our fit function in Eq. (61) is designed to capture part of this logarithmic behavior. Indeed, from inspecting the data we can see that residual logarithmic effects are small, but they may be non-negligible at the precision of our analysis.

One option to estimate these effects is to resum logarithmic terms with the help of Eq. (62) [39]. This equation enables us to run operators defined at some flow time τ to a different value τ_0, which can be chosen to improve perturbative behavior of the operators and limit the effects of logarithms. A particularly appealing choice is $\tau_0 = e^{-\gamma_E}/2\mu_0^2$, since this would exactly set the logarithmic terms defined in Eq. (43) to zero [213]. For the case of the $\Delta Q = 2$ parameter $\mathcal{B}_1$, where the matching matrix is a single number, we can explicitly write this flow-time evolution as

$$\tilde{\mathcal{B}}_1(\tau \to \tau_0) = \exp\left[-\int_0^{L_{\mu_0 \tau}} \tilde{\gamma}(a_s(\mu_0), L) \mathrm{d}L\right] \tilde{\mathcal{B}}(\tau), \tag{66}$$

where $\tilde{\mathcal{B}}_1(\tau \to \tau_0)$ is the set of values for $\tilde{\mathcal{B}}_1(\tau_0)$ calculated for each τ. Having run our continuum results from each τ to τ_0, we can combine these data with the matching coefficient at τ_0, i.e.

$$\mathcal{B}(\mu_0) = \lim_{\tau \to 0} \zeta^{-1}(\tau_0, \mu_0) \tilde{\mathcal{B}}_1(\tau \to \tau_0) \tag{67}$$

where we expect decreased flow-time dependence and thus an easier $\tau \to 0$ extrapolation.

This procedure defines the *RG-improved* SFTX and $\tau \to 0$ extrapolation. The RG improvement of the $\Delta Q = 0$ operators follows analogously, however since the flowed anomalous dimensions are now matrices, we do not write an analytic expression for the evolution to τ_0 but directly integrate Eq. (62) numerically.

In the following we use the RG-improved SFTX as our preferred method to obtain final results for the bag parameters in the $\overline{\text{MS}}$ scheme. A good validation of this choice is seen by comparing Figs. 11 and 12 to 13 and 14 where the final results with and without RG improvement are very compatible with one another. Furthermore, for all four $\Delta Q = 0$ bag parameters, the RG-improved matching leads to more controlled extrapolations and thus somewhat smaller errors at $\tau = 0$. Hence, adopting our default choice of evanescent operators, our final results for the $\Delta Q = 2$ and the four $\Delta Q = 0$ bag parameters are

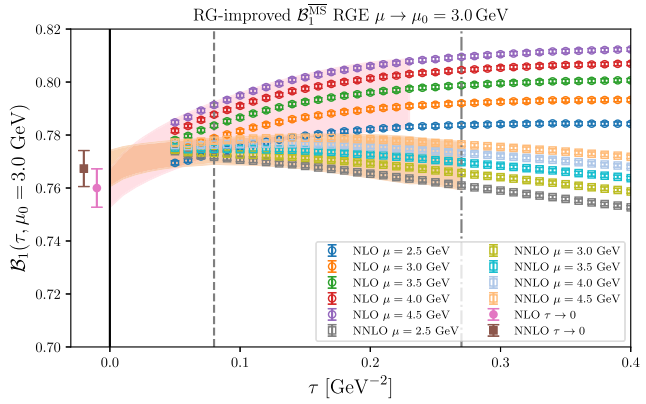


FIG. 13. Zero-flow-time extrapolation of the RG-improved matched flow-time data for the $\Delta Q = 2$ $\mathcal{B}_1$ parameter. The matching to $\overline{\text{MS}}$ is performed at both NLO and NNLO using $\mu \in \{2.5, 3.0, 3.5, 4.0, 4.5\}$ GeV before running back to $\mu_0 = 3$ GeV. The flow-time RGE is used to set flow-time logarithms to zero and improve the extrapolations. The pink and orange shaded areas indicate the spread of all acceptable fits to the data at NLO and NNLO, resulting in the pink and brown data points in the left panel. The dashed line at $\tau = 0.08$ GeV^{-2} indicates the appropriate $\tau_{\min}$ for our dataset, and the dot-dashed lines indicate the maximum flow time which enters the set of acceptable fits for each operator.

$$\begin{aligned}
\mathcal{B}_1^{\overline{\text{MS}}}(3\ \text{GeV}) &= 0.7673(68)_{\text{GF}}, \\
B_1^{\overline{\text{MS}}}(3\ \text{GeV}) &= 1.0524(69)_{\text{GF}}, \\
B_2^{\overline{\text{MS}}}(3\ \text{GeV}) &= 0.9621(26)_{\text{GF}}, \\
\epsilon_1^{\overline{\text{MS}}}(3\ \text{GeV}) &= -0.2275(41)_{\text{GF}}, \\
\epsilon_2^{\overline{\text{MS}}}(3\ \text{GeV}) &= -0.0005(3)_{\text{GF}},
\end{aligned} \tag{68}$$

where the uncertainty labeled "GF" combines statistical errors as well as systematic effects of the $\tau \to 0$ extrapolation from our analysis procedure which also directly propagates uncertainties of a^{-1} quoted in Table I. We will now estimate additional sources of systematic uncertainties in our calculation.

C. Systematic uncertainties

Our values above are obtained at NNLO with the improvement provided by the flow-time RGE following Eq. (67). In Fig. 15 we show these final values using brown squares and they are fully consistent with the orange squares obtained by carrying out the same analysis but without the flowed RG improvement. Subsequently, we discuss other possible sources of uncertainty and also estimate their impact on our results.

1. Continuum-limit extrapolation

In order to test for systematic effects in our continuum extrapolation, we repeat the full analysis discarding the

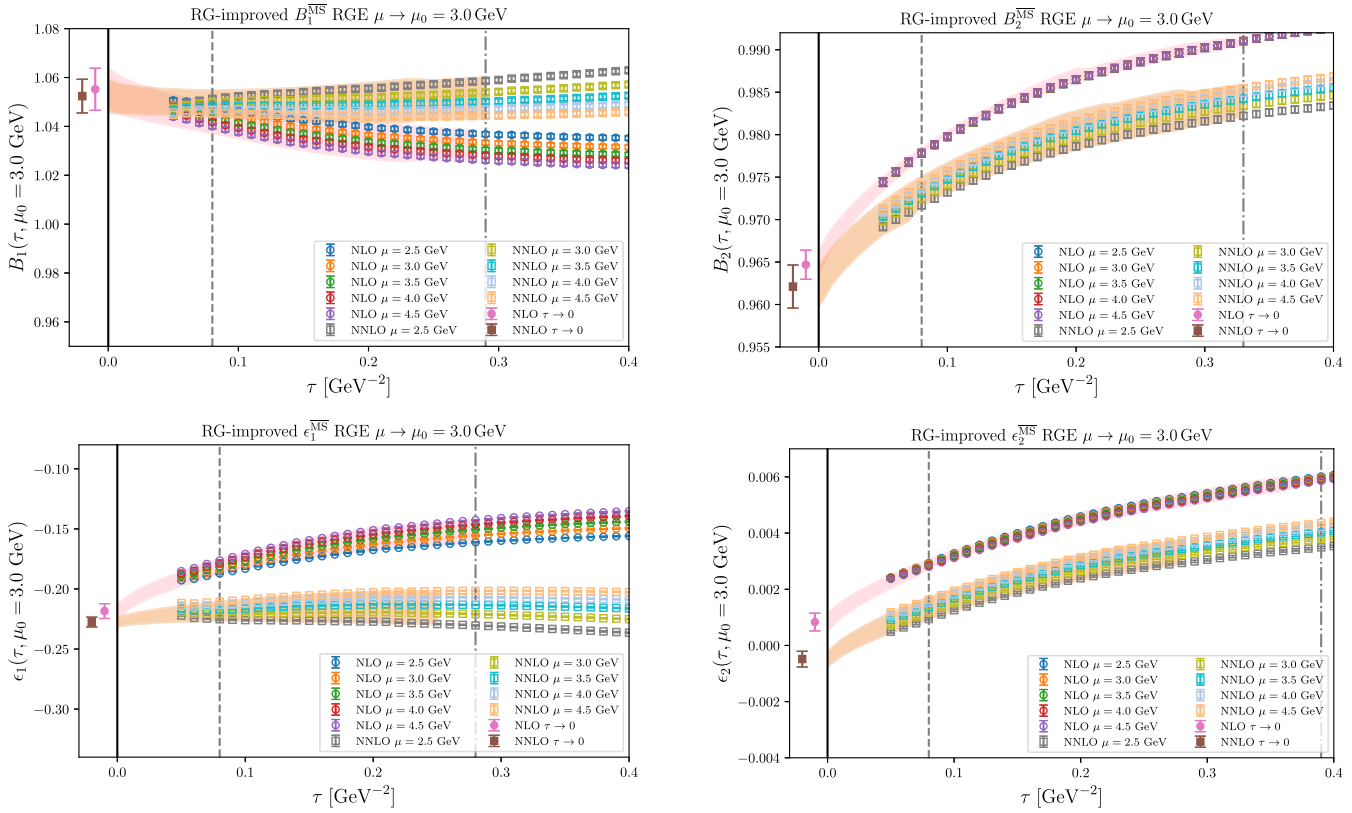


FIG. 14. Zero-flow-time extrapolation of the RG-improved matched flow-time data for the $\Delta Q = 0$ bag parameters—B_1 (top left), B_2 (top right), ϵ_1 (bottom left), and ϵ_2 (bottom right). The matching to $\overline{\rm MS}$ is performed at both NLO and NNLO using $\mu \in \{2.5, 3.0, 3.5, 4.0, 4.5\}$ GeV before running back to $\mu_0 = 3$ GeV. The flow-time RGE is used to set flow-time logarithms to zero and improve the extrapolations. The pink and orange shaded areas indicate the spread of all acceptable fits to the data at NLO and NNLO, resulting in the pink and brown data points in the left panel. The dashed lines indicate $\tau_{\rm min} = 0.08\ \text{GeV}^{-2}$, whereas dash-dotted lines mark the maximum flow time included in our fit results.

coarse C1 and C2 ensembles. This affects the analysis in several ways:

(i) Discretization effects are reduced because the smallest value of a^{-1} increases from 1.78 GeV to 2.38 GeV.

(ii) Heavy-quark discretization effects are reduced since the heaviest bare charm-quark mass simulated decreases from $am_c = 0.64$ to 0.45.

(iii) The uncertainties in the $\tau \to 0$ extrapolation increase, because the $a \to 0$ extrapolation is performed with two instead of three values of the lattice spacing, and thus, the continuum data have increased uncertainty.

We show examples of the resulting continuum limit extrapolations excluding the coarse ensembles in Fig. 16 and 17. The outcome of these alternative continuum limits is compatible with our previously obtained central results, albeit with larger uncertainties, which is an expected effect of discarding 1/3 of our ensembles. We propagate these alternative continuum limits through the analysis to estimate the effect on our final bag parameters in the $\overline{\rm MS}$ scheme.

For all five bag parameters considered, we find at most a 1.8% change of the central values and the obtained bag parameter values are shown in gray in Fig. 15. To quantify the effect of these alternative continuum limits, we assign half the difference of the central values as an additional uncertainty to our final results in Eq. (70) and use the label "CL" to indicate this "continuum limit" uncertainty.

2. *Perturbative truncation*

The systematics due to the truncation of the perturbative series are partly taken into account through the variation of the renormalization scale μ as discussed in the context of Eq. (60). However, estimates based on scale variations are known to be unreliable for capturing the full truncation effects. This is illustrated by the pink circles in Fig. 15, which show the outcome of the RG-improved analysis based on the NLO rather than the NNLO expressions for the matching coefficients. While they are consistent with the NNLO results for $\mathcal{B}_1^{\overline{\rm MS}}$, $B_1^{\overline{\rm MS}}$, $B_2^{\overline{\rm MS}}$, and $\epsilon_1^{\overline{\rm MS}}$, the perturbative uncertainty still seems to be underestimated for $\epsilon_2^{\overline{\rm MS}}$. We therefore include an additional "perturbative truncation" uncertainty by taking half the difference of the central values at NLO and NNLO, referring to it as "PT" in the final results.

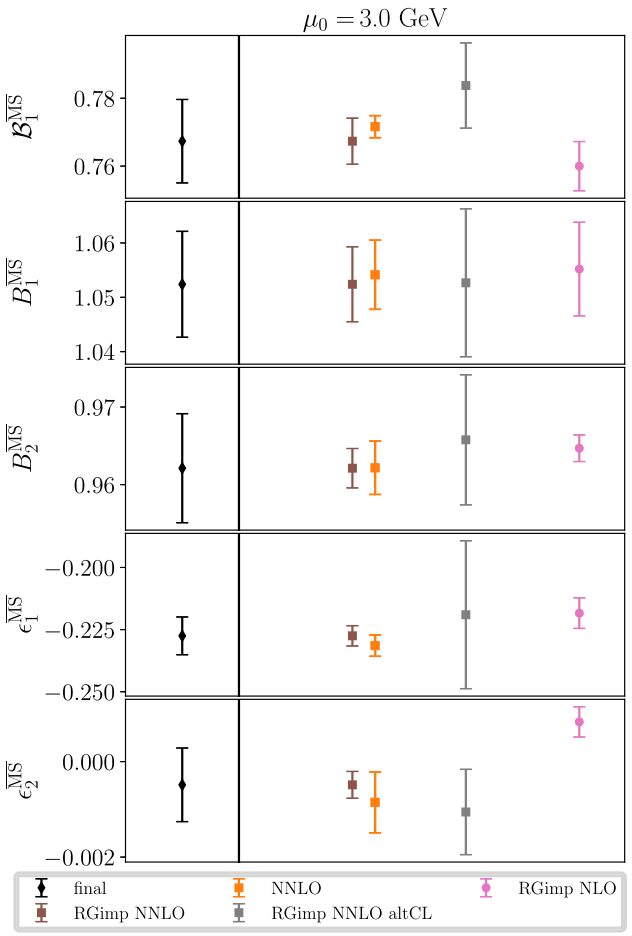


FIG. 15. Final results for the $\Delta Q = 2$ (top) and $\Delta Q = 0$ bag parameters in the $\overline{\rm MS}$ scheme at $\mu_0 = 3$ GeV are shown by the black data points. The central value is taken as the NNLO result (brown) whose error is combined with half the differences to the alternative NNLO (gray) and NLO (pink) results as well as an additional 0.5% quark mass mistuning estimate in quadrature. The data result from $\tau \to 0$ extrapolations using the flow-time RGE to improve the SFTX as described in the text. The NNLO result without the flow-time RGE is also plotted in orange to show consistency.

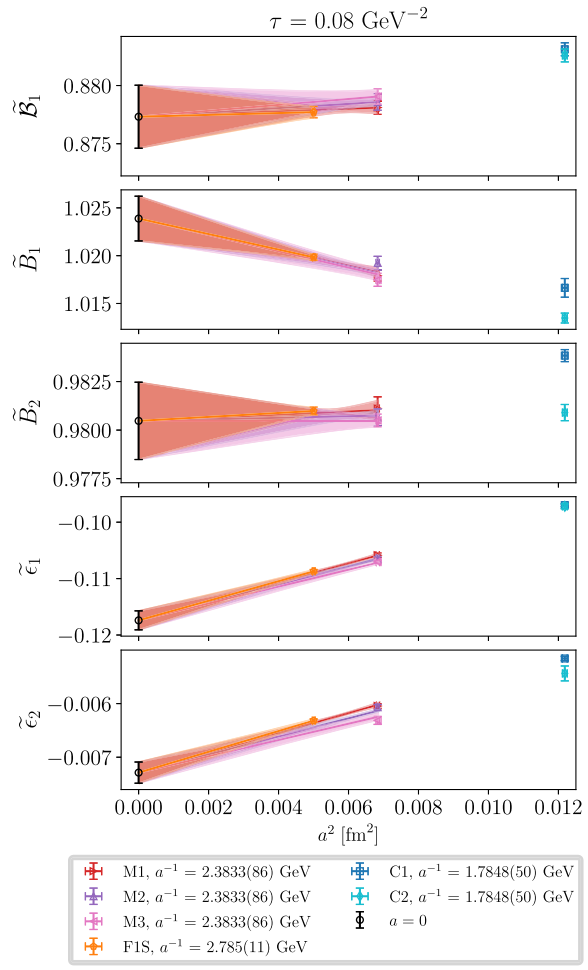


FIG. 16. Alternative chiral-continuum limit fits for each bag parameter at $\tau = 0.08$ GeV^{-2}. The black data point is the continuum-extrapolated value at physical pion mass, and the colored bands are the linear a^2 relations at each ensemble's pion mass after fitting to Eq. (55).

3. Quark-mass tuning

Starting from the physical values of the strange quark mass in lattice units reported by the RBC/UKQCD Collaboration [232–235], we tune the charm-quark masses listed in Table I such that the value of the D_s meson mass matches the PDG value [114] in physical units using the quoted values of the inverse lattice spacings. In Fig. 18 we show the relative deviations from the PDG. Although all data are consistent within uncertainties, they have an associated uncertainty in the matching. Since the dataset of our exploratory calculation does not allow for a refined estimate of this effect on our bag parameters, we simply assign a 0.5% uncertainty due to the matching in our final results.

4. Gluon, light-, and strange-quark discretization

Dominant light-quark and gluon discretization errors arise from the used actions and are of order $\mathcal{O}((a\Lambda_{\rm QCD})^2)$. Using $\Lambda_{\rm QCD} = 300$ MeV, this amounts to 1% at our finest lattice spacing. We account and correct for that by our chiral-continuum extrapolation including terms linear in a^2. Remaining effects start at $\mathcal{O}((a\Lambda_{\rm QCD})^4) \sim 0.01\%$, which is negligible at our current precision. An indicator for discretization errors in domain-wall fermions is the residual mass $am_{\rm res}$ which parametrizes the residual chiral-symmetry breaking as an additive mass term. In our calculation, these are of $\mathcal{O}(am_{\rm res}) \sim 0.4\%$; see Ref. [39].

We add the quark-mass tuning (0.5%) and residual chiral-symmetry breaking (0.4%) systematic uncertainties in quadrature, and assign an additional 0.64% uncertainty, labeled "OS" for "other systematics," to the final results in Eq. (70).

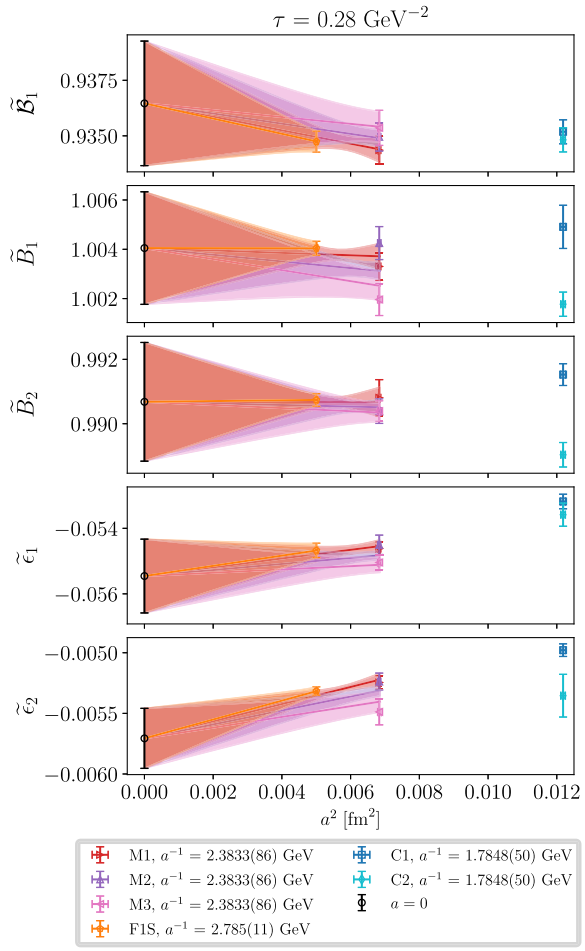


FIG. 17. Chiral-continuum limit fits for each bag parameter at $\tau = 0.28$ GeV^{-2}. The black data point is the continuum-extrapolated value at physical pion mass, and the colored bands are the linear a^2 relations at each ensemble's pion mass after fitting to Eq. (55).

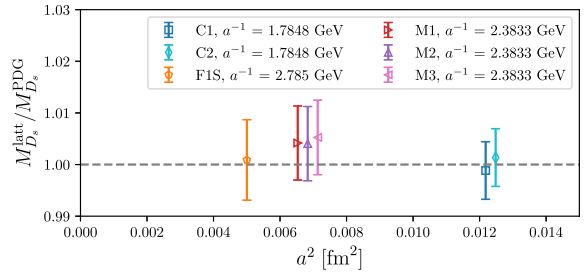


FIG. 18. Ratios of $M_{D_s}^{\text{latt}}/M_{D_s}^{\text{PDG}}$ for each lattice ensemble used.

5. Heavy-quark discretization

Charm quarks are simulated using stout-smeared [240] Möbius domain-wall fermions [241] which are optimized for heavy flavors [242] and allow the simulation of bare charm quark masses with $am_c \lesssim 0.7$ while discretization effects remain small and under control [235,242,262]. This condition is fulfilled on all lattice ensembles in Table I and, hence, we expect discretization errors to be small. As shown in Appendix C of Ref. [39], the residual masses for charm quarks remain small ($am_{\text{res}} \lesssim 10^{-4}$) for all ensembles used and the long plateaus demonstrate that the domain-wall mechanism works well. We therefore conclude heavy quark discretization effects to be negligibly small which is in agreement with the small changes observed when performing alternative continuum limits discarding the coarse ensembles and reducing the largest bare charm quark mass from 0.64 to 0.45.

6. Chiral extrapolation

Although the valence charm and strange quarks are tuned to their physical values, our ensembles differ in the light sea-quark mass, which we have parametrized in the chiral-continuum ansatz of Eq. (55). The lattice-spacing dependence is the dominant component of the chiral-continuum extrapolations, while the chiral term is much smaller and not clearly resolved. Therefore we do not assign a separate uncertainty due to the chiral extrapolation alone.

7. Finite volume

Focusing on a system with only charm- and strange-quark masses in the valence sector on ensembles with $M_\pi \cdot L > 4$, we consider finite-volume effects (FVEs) to be negligible since heavy-light mesons have a short coherence length and the lightest excited state contaminations will scale with masses heavier than pions. While there is no specific evaluation of FVEs in the matrix elements of these operators for charm-strange mesons in the literature, we can interpolate from results for other systems. Reference [263] finds that the $\Delta B = 0$ operator basis for B_s mesons have FVEs $\lesssim 0.05\%$, while Ref. [6] estimates FVEs of $\sim 0.1\%$ for the bag parameters of $\Delta Q = 2$ operators. We infer that the FVEs of the bag parameters of charm-strange mesons lie between 0.1% and 0.05%; this is a negligible uncertainty at our current precision. We therefore do not account for finite-volume effects separately.

8. Isospin-breaking and QED corrections

Furthermore, corrections due to isospin breaking for the light quarks in the sea sector may arise as well as effects due to accounting for electric charges both in the sea and valence sector. Putting the focus on exploring the concept of using GF + SFTX, we refrain from estimating these effects and, hence, corresponding uncertainties are not accounted for.

VIII. PHENOMENOLOGICAL RESULTS

Using a setup with pseudoscalar D_s meson states in pure QCD without electric charges, we determined the bag parameter contributing to the mass difference of a non-physical charm-strange meson at short distance given by a $\Delta Q = 2$ four-quark operator. Accounting for all systematic effects discussed in the previous section, we find in the $\overline{\text{MS}}$ scheme at $\mu_0 = 3$ GeV and adopting our default choice of

evanescent operators

$$\begin{aligned}\mathcal{B}_1^{\overline{\mathrm{MS}}}(3\ \mathrm{GeV}) &= 0.7673(68)_{\mathrm{GF}}(82)_{\mathrm{CL}}(37)_{\mathrm{PT}}(49)_{\mathrm{OS}} \\ &= 0.7673(123). \end{aligned} \tag{69}$$

Based on our knowledge from the B meson sector, we may assume spectator effects to be small and that most of the difference in the hadronic matrix element between using a strange and a light spectator is captured through the decay constant [5,20]. We therefore infer that the bag parameter calculated in Eq. (69) is largely compatible with literature results for short-distance contributions to D^0 mixing. Lattice results exist for the bag parameters of the D^0 meson from both the ETM and FNAL/MILC Collaborations. The former find $\mathcal{B}_1(3\ \mathrm{GeV}) = 0.757(27)$ [10] and the latter $\mathcal{B}_1(3\ \mathrm{GeV}) = 0.784(56)$ [12].[14] These results are in excellent agreement with our result in Eq. (69) albeit with larger uncertainties which are however also expected when extrapolating to/working at physical light quark masses. The bag parameters parametrizing short-distance D^0 mixing have also been calculated using HQET sum rules predicting $\mathcal{B}_1(3\ \mathrm{GeV}) = 0.654^{+0.060}_{-0.052}$ [116]. This result exhibits a noticeable tension to the lattice determinations. However, HQET is less suitable for charm quarks than for bottom quarks, and Ref. [116] does not include $O(1/m_Q^n)$ corrections in the HQET-QCD matching procedure. Note that the results of Refs. [10,12,116], based on NLO matching, employ choices of evanescent operators [259,264] which differ from ours. Nevertheless, our final results can be compared consistently with these because the differences occur only at NNLO for $\mathcal{B}_1^{\overline{\mathrm{MS}}}$.

For the bag parameters parametrizing $\Delta Q = 0$ operator matrix elements describing the lifetime ratio of D_s/D^0 mesons, we obtain, using our default choice of evanescent operators,

$$\begin{aligned}B_1^{\overline{\mathrm{MS}}}(3\ \mathrm{GeV}) &= 1.0524(69)_{\mathrm{GF}}(1)_{\mathrm{CL}}(14)_{\mathrm{PT}}(67)_{\mathrm{OS}} \\ &= 1.0524(97), \\ B_2^{\overline{\mathrm{MS}}}(3\ \mathrm{GeV}) &= 0.9621(25)_{\mathrm{GF}}(18)_{\mathrm{CL}}(13)_{\mathrm{PT}}(62)_{\mathrm{OS}} \\ &= 0.9621(70), \\ \epsilon_1^{\overline{\mathrm{MS}}}(3\ \mathrm{GeV}) &= -0.2275(41)_{\mathrm{GF}}(42)_{\mathrm{CL}}(46)_{\mathrm{PT}}(14)_{\mathrm{OS}} \\ &= -0.2275(76), \\ \epsilon_2^{\overline{\mathrm{MS}}}(3\ \mathrm{GeV}) &= -0.0005(3)_{\mathrm{GF}}(0)_{\mathrm{CL}}(7)_{\mathrm{PT}}(0)_{\mathrm{OS}} \\ &= -0.0005(8). \end{aligned} \tag{70}$$

These are the first lattice results for the bag parameters of $\Delta Q = 0$ operators with a full error budget, and represent a significant step towards more precise predictions of heavy meson lifetimes and lifetime ratios using lattice QCD. Although our focus is on establishing the use of GF + SFTX to renormalize four-quark operators, we obtain percent-level results for $B_1^{\overline{\mathrm{MS}}}$, $B_2^{\overline{\mathrm{MS}}}$, and $\epsilon_1^{\overline{\mathrm{MS}}}$, while $\epsilon_2^{\overline{\mathrm{MS}}}$ is much smaller and vanishes within uncertainties. The latter is however an artifact of a particular choice of evanescent operators (cf. Appendix B).

Although $\mathrm{SU}(3)_{\mathrm{F}}$-breaking corrections to the $\Delta Q = 0$ bag parameters are calculated in Ref. [199] within the HQET sum-rules framework, the HQET-QCD matching for this scenario has not been calculated and, hence, we cannot directly compare results. From Tables 3 and 4 of Ref. [199], we see, however, that the difference between B_d and B_s bag parameters is very small, implying mostly negligible spectator effects. Therefore we expect again that the results calculated here using D_s mesons are largely compatible with D^0 calculations. The most up-to-date values of the $\Delta Q = 0$ bag parameters in QCD from sum rules for D mesons are presented in Ref. [49], where a different basis of evanescent operators has been used than here. Performing the basis transformation described in Appendix B, we express our results of Eq. (70) in the scheme used in Ref. [49] and obtain

$$\begin{aligned}B_1'^{\overline{\mathrm{MS}}}(3\ \mathrm{GeV}) &= 1.103(10), \\ B_2'^{\overline{\mathrm{MS}}}(3\ \mathrm{GeV}) &= 0.9754(71), \\ \epsilon_1'^{\overline{\mathrm{MS}}}(3\ \mathrm{GeV}) &= -0.2427(71), \\ \epsilon_2'^{\overline{\mathrm{MS}}}(3\ \mathrm{GeV}) &= -0.0289(8). \end{aligned} \tag{71}$$

As another consistency check, we also performed the $\tau \to 0$ extrapolations by directly using the matching coefficients defined for this evanescent scheme and find fully compatible results. In comparison to Eq. (6.27) of Ref. [49] our results are an order of magnitude more precise. We note, however, that the uncertainties in Ref. [49] are dominated by the HQET-QCD matching procedure. Furthermore, our values in particular for $B_1^{\overline{\mathrm{MS}}}$ and $\epsilon_1^{\overline{\mathrm{MS}}}$ differ significantly from those of Ref. [49]. This may again be due to the HQET-QCD matching procedure, which may require including $O(1/m_Q^n)$ corrections to more accurately describe D meson.

From a phenomenological perspective, our value for $\epsilon_1^{\overline{\mathrm{MS}}}$ is particularly interesting, because in the HQE the Wilson coefficient multiplying this parameter is rather large [187]. Hence, the observed difference of about a factor of 2 compared to the existing literature may lead to a significant effect in the lifetime predictions for D mesons. An independent verification of our findings would therefore be desirable.

In addition to lifetimes and lifetime ratios, the $\Delta Q = 0$ four-quark operators also contribute to other processes described by the HQE, such as rare semileptonic B-meson

[14] We convert the quoted matrix element using $f_D^{N_f=2+1} = 210.4(1.5)$ MeV [20] and $M_{D^0} = 1864.84(5)$ MeV [114].

decays and are in fact the dominant uncertainties at high q^2 [265,266]. A future high-precision determination of these quantities for B mesons is therefore advantageous to the broader flavor physics community. In particular, the lifetime-ratio operator basis is immediately relevant to the decay-rate ratios of the currents $b \to s\ell\ell$ and $b \to u\ell\nu$ as discussed in Ref. [265] while the future application of our procedure to the eye diagrams will be highly beneficial to $b \to s\ell\ell$ processes themselves.

IX. CONCLUSION

Using six RBC/UKQCD $2+1$-flavor domain-wall ensembles and performing a valence sector measurement with charm and strange quarks tuned to their physical values, we calculate in a heavy-light system $\Delta Q = 2$ operators describing neutral meson mixing as well as $\Delta Q = 0$ operators related to bag parameters entering the determination of heavy meson lifetime ratios. Renormalization of operators is performed using fermionic GF in combination with the SFTX to match our results to the $\overline{\text{MS}}$ scheme. This matching is performed at both NLO and NNLO at a scale of $\mu_0 = 3$ GeV. Taking advantage of perturbatively calculated anomalous dimensions, we improve the $\tau \to 0$ extrapolation by running the matching scale to higher values and canceling flow-time logarithms using the flowed RGE. In the future this may further be improved by nonperturbative determinations of the corresponding anomalous dimensions [267–269].

Although the focus of this work lies on the method to calculate and renormalize four-quark operators using GF + SFTX, we further achieve percent-level results for the bag parameters indicating that GF + SFTX is also a competitive method w.r.t. overall uncertainties. While our results have a full error budget, we do stress, however, that in this study we choose to simplify the problem by neglecting contributions from eye diagrams which are required to obtain absolute lifetimes and $\text{SU}(3)_\text{F}$-breaking effects. The challenge of the eye diagrams arises due to their poor signal-to-noise ratio demanding different numerical techniques to simulate and, moreover, they also induce mixing with operators of lower mass-dimension under renormalization. In the case of $\epsilon_2^{\overline{\text{MS}}}$, we observe sensitivity to the choice of evanescent operator scheme and provide formulae to convert to a broad class of such choices.

The successful application of the GF + SFTX framework demonstrated here and also in other works [39,42,43,45] motivates an extended program in the future. It will be interesting to incorporate the full $\Delta Q = 0$ operator basis and handle eye diagrams with the associated mixing of lower mass-dimension operators in the SFTX. Furthermore, it looks promising to choose a larger set of ensembles in order to improve control of all systematic effects in a high-precision study extending this calculation to use both physical light quarks as well as "heavier-than-charm" quarks to extrapolate towards the bottom. This will allow us to obtain a more complete picture of lifetimes and lifetime ratios for heavy-light mesons including $D^0, D^+, D_s^+, B^0, B^+$, and B_s as well as heavy baryons.

Note added. While this paper was under review, Ref. [270] presented the NNLO Wilson coefficients for heavy-meson lifetime ratios and combined them with the bag parameters determined here. It finds that our lattice results significantly change the charm lifetime-ratio predictions compared to the HQET sum-rule results [49], reduce the associated uncertainties, and improve the agreement with experiment.

ACKNOWLEDGMENTS

We thank the RBC/UKQCD Collaboration for generating and making their gauge field ensembles publicly available. Special thanks is given to Felix Erben, Ryan Hill, and J. Tobias Tsang for assistance in setting up the simulation code, and we thank Anna Hasenfratz and Martin Lang for constructive discussions. Fruitful input and encouragement from the members of the CRC TRR 257 is highly appreciated. Special thanks in this respect go to Alexander Lenz, Uli Nierste, and Thomas Mannel. We are also grateful to the authors of Ref. [270], especially Francesco Moretti, for comparing the anomalous dimensions of the general basis of evanescent operators given in Appendix A, including the nonphysical entries. Similarly, we thank the authors of Ref. [260], especially Pol Morell, for help comparing to our anomalous dimensions. These computations used resources provided by the OMNI cluster at the University of Siegen, the HAWK cluster at the High-Performance Computing Center Stuttgart, the DeiC Large Memory HPC Type3/Hippo System managed by the eScience Center at the University of Southern Denmark, and LUMI-G at the CSC data center Finland (DeiC National HPC g.a. DEIC-SDU-L5-13 and DEIC-SDU-N5-2024053). This research was supported by Deutsche Forschungsgemeinschaft (DFG, German Research Foundation) through Grant No. 396021762—TRR 257 "Particle Physics Phenomenology after the Higgs Discovery," through Grant No. 513989149, Germany's Excellence Strategy—EXC 3107—Project No. 533766364, UK STFC Grant No. ST/X000494/1, the Swiss National Science Foundation (SNSF) under Contract No. TMSGI2_211209, the National Science Foundation under Grant No. PHY-2209185, and the DOE Topical Collaboration "Nuclear Theory for New Physics" Award No. DE-SC0023663.

DATA AVAILABILITY

The data that support the findings of this article are openly available [271].

APPENDIX A: RENORMALIZATION CONSTANTS

The bare gauge coupling is related to the $\overline{\text{MS}}$-renormalized coupling by

$$g_0 = \left(\frac{\mu^2 e^{\gamma_E}}{4\pi}\right)^{\epsilon/2} Z_g(a_s(\mu))g(\mu), \tag{A1}$$

where μ denotes the renormalization scale and Z_g is the renormalization constant of the coupling,

$$Z_g(a_s) = 1 - a_s\frac{\beta_0}{2\epsilon} + a_s^2\left(\frac{3\beta_0^2}{8\epsilon^2} - \frac{\beta_1}{4\epsilon}\right) + \mathcal{O}(a_s^3), \tag{A2}$$

with the coefficients

$$\beta_0 = \frac{1}{4}\left(11 - \frac{2}{3}n_f\right),$$
$$\beta_1 = \frac{1}{16}\left(102 - \frac{38}{3}n_f\right), \tag{A3}$$

of the QCD beta function

$$\beta(a_s) = -\epsilon - a_s\sum_{n=0}^{\infty}\beta_n a_s^n. \tag{A4}$$

The NNLO relation between a generic renormalization constant and the corresponding anomalous dimension, defined by

$$\frac{d}{d\ln\mu^2}Z_{ij} = -\gamma_{ik}Z_{kj} \tag{A5}$$

and

$$\gamma_{ij} = -a_s\sum_{n=0}^{\infty}a_s^n\gamma_{n,ij} \tag{A6}$$

is

$$Z_{ij} = \delta_{ij} + a_s\left(-\frac{1}{\epsilon}\gamma_{0,ij} + Z_{ij}^{10}\right) + a_s^2\left(\frac{1}{2\epsilon^2}[\gamma_{0,ik}\gamma_{0,kj} + \beta_0\gamma_{0,ij}] - \frac{1}{2\epsilon}[\gamma_{1,ij} + \beta_0 Z_{ij}^{10} + \gamma_{0,ik}Z_{kj}^{10} + Z_{ik}^{10}\gamma_{0,kj}] + Z_{ij}^{20}\right) + \mathcal{O}(a_s^3). \tag{A7}$$

The finite parts of the renormalization constants, Z_{ij}^{n0} are only nonzero if $i \in \mathcal{E}$ and $j \in \mathcal{O}$ as described in Sec. IV A.

As mentioned in Sec. IV C, the two sets of operators $\mathcal{O}^{(1)} \equiv \{\mathcal{O}_1, \mathcal{T}_1\}$ and $\mathcal{O}^{(2)} \equiv \{\mathcal{O}_2, \mathcal{T}_2\}$ do not mix with each other. The result for the physical submatrix of the anomalous dimension is [205,258,259]

$$\gamma_0^{(1)} = \begin{pmatrix} 0 & -\frac{3}{2} \\ -\frac{1}{3} & \frac{1}{2} \end{pmatrix}, \tag{A8}$$

$$\gamma_0^{(2)} = \begin{pmatrix} 2 & 0 \\ 0 & -\frac{1}{4} \end{pmatrix}, \tag{A9}$$

and

$$\gamma_1^{(1)} = \begin{pmatrix} \frac{7}{24} & -\frac{111}{32} + \frac{7}{24}n_f \\ -\frac{85}{48} + \frac{7}{108}n_f & -\frac{185}{96} + \frac{11}{72}n_f \end{pmatrix}, \tag{A10}$$

$$\gamma_1^{(2)} = \begin{pmatrix} \frac{49}{6} - \frac{5}{18}n_f & -\frac{95}{32} + \frac{1}{12}n_f \\ -\frac{23}{144} + \frac{1}{54}n_f & -\frac{269}{64} + \frac{37}{144}n_f \end{pmatrix}. \tag{A11}$$

In order to be able to rotate to a more general scheme (see Appendix B), we also need unphysical parts of the renormalization matrix, which we find to be[15]

$$\gamma_{0,\mathcal{OE}}^{(1)} = \begin{pmatrix} 0 & \frac{1}{4} & 0 & 0 \\ \frac{1}{18} & \frac{5}{48} & 0 & 0 \end{pmatrix}, \qquad \gamma_{0,\mathcal{OE}}^{(2)} = \begin{pmatrix} 0 & \frac{1}{4} & 0 & 0 \\ \frac{1}{18} & \frac{5}{48} & 0 & 0 \end{pmatrix},$$
$$\gamma_{1,\mathcal{OE}}^{(1)} = \begin{pmatrix} -\frac{17}{48} & \frac{11}{192} - \frac{1}{144}n_f & \frac{7}{576} & \frac{35}{1536} \\ -\frac{169}{864} - \frac{1}{648}n_f & \frac{317}{1152} - \frac{5}{1728}n_f & \frac{35}{6912} & -\frac{1}{3072} \end{pmatrix},$$
$$\gamma_{1,\mathcal{OE}}^{(2)} = \begin{pmatrix} -\frac{11}{36} & \frac{7}{24} - \frac{1}{144}n_f & \frac{7}{576} & \frac{35}{1536} \\ -\frac{31}{216} - \frac{1}{648}n_f & \frac{283}{1152} - \frac{5}{1728}n_f & \frac{35}{6912} & -\frac{1}{3072} \end{pmatrix},$$
$$\gamma_{0,\mathcal{EE}}^{(1)} = \begin{pmatrix} 0 & -\frac{7}{2} & 0 & \frac{1}{4} \\ -\frac{7}{9} & -\frac{1}{3} & \frac{1}{18} & \frac{5}{48} \\ * & * & * & * \\ * & * & * & * \end{pmatrix},$$
$$\gamma_{0,\mathcal{EE}}^{(2)} = \begin{pmatrix} -\frac{2}{3} & -4 & 0 & \frac{1}{4} \\ -\frac{8}{9} & -\frac{1}{12} & \frac{1}{18} & \frac{5}{48} \\ * & * & * & * \\ * & * & * & * \end{pmatrix}, \tag{A12}$$

where the entries denoted by $*$ in $\gamma_{0,\mathcal{EE}}$ do not contribute to our final result. They require including the evanescent operators of the third generation and were thus not computed. The two-loop anomalous dimensions γ_1 are scheme dependent, meaning that their values are specified for the choice of evanescent operators of Sec. IV A. The result in a general scheme can be found in the ancillary files (see Appendix C and Ref. [209]).

For the $\Delta Q = 2$ operator, we find

$$\gamma_{\mathcal{Q}_1}^{(0)} = -\frac{1}{2}, \qquad \gamma_{\mathcal{Q}_1}^{(1)} = \frac{7}{32} - \frac{1}{72}n_f. \tag{A13}$$

[15]These results have been obtained independently in Ref. [270].

The $\overline{\text{MS}}$ renormalization constant of the flowed-quark field $Z_\chi^{\overline{\text{MS}}}$, introduced in Eq. (27), is related by Eq. (A7) to the anomalous dimensions given by [34,213]

$$\gamma_{\chi,0} = -1,$$
$$\gamma_{\chi,1} = -\frac{73}{8} + \frac{11}{36}n_\text{f} + \frac{26}{9}\ln 2. \tag{A14}$$

The finite renormalization ζ_χ relating the ringed scheme to the $\overline{\text{MS}}$ scheme,

$$\mathring{Z}_\chi = \zeta_\chi(\tau,\mu) Z_\chi^{\overline{\text{MS}}}, \tag{A15}$$

is [201,203]

$$\begin{aligned}\zeta_\chi(\tau,\mu) = 1 &- a_\text{s}\left(\gamma_{\chi,0}L_{\mu\tau} + \ln 3 + \frac{4}{3}\ln 2\right)\\ &+ a_\text{s}^2\left\{\frac{\gamma_{\chi,0}}{2}(\gamma_{\chi,0}-\beta_0)L_{\mu\tau}^2\right.\\ &+ \left[\gamma_{\chi,0}(\beta_0-\gamma_{\chi,0})\ln 3 + \frac{4}{3}\gamma_{\chi,0}(\beta_0-\gamma_{\chi,0})\ln 2\right.\\ &\left.\left. - \gamma_{\chi,1}\right]L_{\mu\tau} + \frac{c_\chi^{(2)}}{16}\right\} + \mathcal{O}(a_\text{s}^3),\end{aligned} \tag{A16}$$

where

$$c_\chi^{(2)} = 4c_{\chi,\text{A}} + \frac{16}{9}c_{\chi,\text{F}} + \frac{2}{3}n_\text{f}c_{\chi,\text{R}}. \tag{A17}$$

The coefficients have been determined in Ref. [201]:

$$\begin{aligned}c_{\chi,\text{A}} &= -23.7947, \qquad c_{\chi,\text{F}} = 30.3914,\\ c_{\chi,\text{R}} &= -\frac{131}{18} + \frac{46}{3}\zeta(2) + \frac{944}{9}\ln 2 + \frac{160}{3}\ln^2 2 - \frac{172}{3}\ln 3\\ &\quad + \frac{104}{3}\ln 2\ln 3 - \frac{178}{3}\ln^2 3 + \frac{8}{3}\text{Li}_2(1/9)\\ &\quad - \frac{400}{3}\text{Li}_2(1/3) + \frac{112}{3}\text{Li}_2(3/4) = -3.92255\ldots.\end{aligned} \tag{A18}$$

Only digits which are not affected by the numerical uncertainty are quoted in Eq. (A18).

APPENDIX B: SCHEME DEPENDENCE

The definition of the scheme for the evanescent operators in Eqs. (34) and (35) includes an arbitrariness; in particular, one is free to add terms which vanish in $D = 4$. Such additional terms, however, change the result of our calculation and correspond to choosing a different renormalization scheme. In a more general scheme, the evanescent operators of the first generation are

$$\begin{aligned}\mathcal{E}'^{(1)}_{\mathcal{O}_1} &= (\bar\psi_\alpha\gamma_{\mu\nu\rho}(1-\gamma_5)\psi_\beta)(\bar\psi_\gamma\gamma_{\rho\nu\mu}(1-\gamma_5)\psi_\delta) + E_1^{(1)}\mathcal{O}_1,\\ \mathcal{E}'^{(1)}_{T_1} &= (\bar\psi_\alpha\gamma_{\mu\nu\rho}(1-\gamma_5)T^A\psi_\beta)(\bar\psi_\gamma\gamma_{\rho\nu\mu}(1-\gamma_5)T^A\psi_\delta)\\ &\quad + E_2^{(1)}T_1,\\ \mathcal{E}'^{(1)}_{\mathcal{O}_2} &= (\bar\psi_\alpha\gamma_{\mu\nu}(1-\gamma_5)\psi_\beta)(\bar\psi_\gamma\gamma_{\nu\mu}(1+\gamma_5)\psi_\delta) + E_3^{(1)}\mathcal{O}_2,\\ \mathcal{E}'^{(1)}_{T_2} &= (\bar\psi_\alpha\gamma_{\mu\nu}(1-\gamma_5)T^A\psi_\beta)(\bar\psi_\gamma\gamma_{\nu\mu}(1+\gamma_5)T^A\psi_\delta)\\ &\quad + E_4^{(1)}T_2,\end{aligned} \tag{B1}$$

where

$$\begin{aligned}E_1^{(1)} &= -4 + E_{1,1}^1\varepsilon + E_{1,2}^1\varepsilon^2,\\ E_2^{(1)} &= -4 + E_{2,1}^1\varepsilon + E_{2,2}^1\varepsilon^2,\\ E_3^{(1)} &= -4 + E_{3,1}^1\varepsilon + E_{3,2}^1\varepsilon^2,\\ E_4^{(1)} &= -4 + E_{4,1}^1\varepsilon + E_{4,2}^1\varepsilon^2.\end{aligned} \tag{B2}$$

For the second generation, we work with the operators

$$\begin{aligned}\mathcal{E}'^{(2)}_{\mathcal{O}_1} &= (\bar\psi_\alpha\gamma_{\mu\nu\rho\sigma\tau}(1-\gamma_5)\psi_\beta)(\bar\psi_\gamma\gamma_{\tau\sigma\rho\nu\mu}(1-\gamma_5)\psi_\delta)\\ &\quad + E_1^{(2)}\mathcal{O}_1 + B_1\mathcal{E}^{(1)}_{\mathcal{O}_1},\\ \mathcal{E}'^{(2)}_{T_1} &= (\bar\psi_\alpha\gamma_{\mu\nu\rho\sigma\tau}(1-\gamma_5)T^A\psi_\beta)(\bar\psi_\gamma\gamma_{\tau\sigma\rho\nu\mu}(1-\gamma_5)T^A\psi_\delta)\\ &\quad + E_2^{(2)}T_1 + B_2\mathcal{E}^{(1)}_{T_1},\\ \mathcal{E}'^{(2)}_{\mathcal{O}_2} &= (\bar\psi_\alpha\gamma_{\mu\nu\rho\sigma}(1-\gamma_5)\psi_\beta)(\bar\psi_\gamma\gamma_{\sigma\rho\nu\mu}(1+\gamma_5)\psi_\delta)\\ &\quad + E_3^{(2)}\mathcal{O}_2 + B_3\mathcal{E}^{(1)}_{\mathcal{O}_2},\\ \mathcal{E}'^{(2)}_{T_2} &= (\bar\psi_\alpha\gamma_{\mu\nu\rho\sigma}(1-\gamma_5)T^A\psi_\beta)(\bar\psi_\gamma\gamma_{\sigma\rho\nu\mu}(1+\gamma_5)T^A\psi_\delta)\\ &\quad + E_4^{(2)}T_2 + B_4\mathcal{E}^{(1)}_{T_2},\end{aligned} \tag{B3}$$

where

$$\begin{aligned}E_1^{(2)} &= -16 + E_{1,1}^2\varepsilon + E_{1,2}^2\varepsilon^2,\\ B_1 &= B_{1,0} + B_{1,1}\varepsilon,\\ E_2^{(2)} &= -16 + E_{2,1}^2\varepsilon + E_{2,2}^2\varepsilon^2,\\ B_2 &= B_{2,0} + B_{2,1}\varepsilon,\\ E_3^{(2)} &= -16 + E_{3,1}^2\varepsilon + E_{3,2}^2\varepsilon^2,\\ B_3 &= B_{3,0} + B_{3,1}\varepsilon,\\ E_4^{(2)} &= -16 + E_{4,1}^2\varepsilon + E_{4,2}^2\varepsilon^2,\\ B_4 &= B_{4,0} + B_{4,1}\varepsilon.\end{aligned} \tag{B4}$$

The numerically specified coefficients were obtained by Fierz relations and are chosen such that the operators are evanescent; all other coefficients are part of the definition of the basis of evanescent operators.

In the case of the $\Delta Q = 2$ operators, we use the nonmixing basis which refers to the physical operators

TABLE II. The expressions of the ancillary files `Zeta.m` and `Zeta.py` that encode the main results of this paper. The notation of the variables should be self-explanatory; more details are given in the header of these files.

`Zeta.m`	`Zeta.py`	Meaning	Reference
`ZfinInv1`	`ZfinInv1(alpha_s, nf)`	$Z_{\mathrm{fin},1}^{-1}$	Eq. (B9)
`ZfinInv2`	`ZfinInv2(alpha_s, nf)`	$Z_{\mathrm{fin},2}^{-1}$	Eq. (B9)
`zetaInv1`	`zetaInv1(alpha_s, nf, mu, t)`	$\zeta_1'^{-1}$	Eqs. (44), (58), and (B10)
`zetaInv2`	`zetaInv2(alpha_s, nf, mu, t)`	$\zeta_2'^{-1}$	Eqs. (45), (58), and (B10)
`zetaInvMixing`	`zetaInvMixing(alpha_s, nf, mu, t)`	$\zeta_{\mathcal{Q}_1}^{-1}$	Eqs. (50) and (58)
`zetaInv1NormA`	`zetaInv1NormA(alpha_s, nf, mu, t)`	$\zeta_{B,1}'^{-1}$	Eqs. (58) and (B10)
`zetaInv2NormP`	`zetaInv2NormP(alpha_s, nf, mu, t)`	$\zeta_{B,2}'^{-1}$	Eqs. (58) and (B10)
`zetaInvMixingNormA`	`zetaInvMixingNormA(alpha_s, nf, mu, t)`	$\zeta_{\mathcal{B},1}^{-1}$	Eq. (58)
`gamma1`	`gamma1(alpha_s, nf)`	$\gamma'^{(1)}$	Eqs. (A6), (A8), (A10), (A12), and (B10)
`gamma2`	`gamma2(alpha_s, nf)`	$\gamma'^{(2)}$	Eqs. (A6), (A9), (A11), (A12), and (B10)
`gammaMixing`	`gammaMixing(alpha_s, nf)`	$\gamma_{\mathcal{Q}_1}$	Eqs. (A6) and (A13)

$\{\mathcal{O}_+, \mathcal{O}_-\}$ and the evanescent operators $\{\mathcal{E}'^{(1)}_{\mathcal{O}_1}, \mathcal{E}'^{(1)}_{\mathcal{T}_1}, \mathcal{E}'^{(2)}_{\mathcal{O}_1}, \mathcal{E}'^{(2)}_{\mathcal{T}_1}\}$ given in Eqs. (B1) and (B3) with $\alpha = \gamma = Q$, $\beta = \delta = q$ and the coefficients of Eqs. (B2) and (B4) given by [205,230]

$$\begin{aligned} E^1_{1,1} &= E^1_{2,1} = 8, \\ E^1_{1,2} &= E^1_{2,2} = -4, \\ E^2_{1,1} &= E^2_{2,1} = 64, \\ E^2_{1,2} &= -\frac{1688}{25}, \qquad E^2_{2,2} = \frac{2632}{25}, \\ B_{1,0} &= B_{2,0} = -40, \\ B_{1,1} &= B_{2,1} = 40. \end{aligned} \tag{B5}$$

This choice of scheme respects Fierz symmetry and ensures that there is no mixing among $\mathcal{O}_+$ and $\mathcal{O}_-$ such that there are no off-diagonal entries in the physical submatrices of both the matching matrix as well as the anomalous dimensions.

In the ancillary file, we provide the matching matrix and the anomalous dimension matrix in a general scheme as a function of the coefficients $E^k_{i,j}$.[16] The results in a general scheme can be obtained by performing a rotation of the evanescent operators from the minimal basis of Eqs. (34) and (35) to the more general basis of Eqs. (B1) to (B4) [230,272]

$$\mathcal{E}'_i = M_i(\mathcal{E}_i + \varepsilon U_i \mathcal{O}_i + \varepsilon^2 V_i \mathcal{O}_i), \tag{B6}$$

where

$$M_1 = \begin{pmatrix} 1 & 0 & 0 & 0 \\ 0 & 1 & 0 & 0 \\ B_{1,0} + \varepsilon B_{1,1} & 1 & 1 & 0 \\ 0 & B_{2,0} + \varepsilon B_{2,1} & 0 & 1 \end{pmatrix},$$
$$M_2 = \begin{pmatrix} 1 & 0 & 0 & 0 \\ 0 & 1 & 0 & 0 \\ B_{3,0} + \varepsilon B_{3,1} & 1 & 1 & 0 \\ 0 & B_{4,0} + \varepsilon B_{4,1} & 0 & 1 \end{pmatrix}, \tag{B7}$$

and

$$U_1 = \begin{pmatrix} E^1_{1,1} & 0 \\ 0 & E^1_{2,1} \\ E^2_{1,1} & 0 \\ 0 & E^2_{2,1} \end{pmatrix}, \qquad U_2 = \begin{pmatrix} E^1_{3,1} & 0 \\ 0 & E^1_{4,1} \\ E^2_{3,1} & 0 \\ 0 & E^2_{4,1} \end{pmatrix},$$
$$V_1 = \begin{pmatrix} E^1_{1,2} & 0 \\ 0 & E^1_{2,2} \\ E^2_{1,2} & 0 \\ 0 & E^2_{2,2} \end{pmatrix}, \qquad V_2 = \begin{pmatrix} E^1_{3,2} & 0 \\ 0 & E^1_{4,2} \\ E^2_{3,2} & 0 \\ 0 & E^2_{4,2} \end{pmatrix}. \tag{B8}$$

TABLE III. Notation for the variables in the ancillary files.

`Zeta.m`	`Zeta.py`	Meaning	Reference
`nc`	`NC`	N_c	Section III
`tr`	`TR`	T_R	Appendix C
`Lmut`	`Lmut`	$L_{\mu\tau}$	Eq. (43)
`as`	`a_s`	a_s	Section IV C
`nf`	`nf`	n_f	Section IV C
`z2`	`zeta2`	$\zeta(2)$	Eq. (42)

[16]The choice of $B_{4,1}$ neither impacts the matching matrix nor the physical part of the anomalous dimension, which can be seen from the fact that in the rotation to a general scheme it only appears in the matrix describing the rotation among the evanescent operators M_i.

We can now obtain the matching matrix in a general scheme by applying the transformation to the bare results before performing the renormalization. Alternatively, the renormalized result in a general scheme can be obtained by multiplying the renormalized matching matrix with a finite renormalization induced by the rotation matrices U, V

$$\begin{aligned} Z_{\mathrm{fin},1/2} &= 1 + a_s Z^1_{\mathrm{fin},1/2} + a_s^2 Z^2_{\mathrm{fin},1/2} + \mathcal{O}(a_s^3), \\ Z^1_{\mathrm{fin},1/2} &= \gamma^{(1/2)}_{0,\mathcal{OE}} U_{1/2}, \\ Z^2_{\mathrm{fin},1/2} &= \frac{1}{2}\gamma^{(1/2)}_{1,\mathcal{OE}} U_{1/2} + \frac{1}{2}(\gamma^{(1/2)}_{0,\mathcal{O},k}\gamma^{(1/2)}_{0,k\mathcal{E}} + \beta_0\gamma^{(1/2)}_{0,\mathcal{OE}})V_{1/2} \\ &\quad - \gamma^{(1/2)}_{0,\mathcal{OE}} V_{1/2}\gamma^{(1/2)}_0. \end{aligned} \tag{B9}$$

We then get the result for the matching matrix in the general scheme $\zeta'^{-1}_{1/2}$ by

$$\zeta'^{-1}_{1/2} = Z^{-1}_{\mathrm{fin},1/2}\zeta^{-1}_{1/2}. \tag{B10}$$

A third way to determine the general scheme dependence is the direct calculation of the matching matrix using the evanescent operators displayed in Eqs. (B1) to (B4). We find agreement between all three methods which provides a strong check on our result. The finite renormalization constant in Eq. (B9) can also be found in the ancillary file; it can be used to convert the results of the bag parameters from Eq. (70) to any scheme captured by Appendix B.

APPENDIX C: ANCILLARY FILES

We provide the perturbative results of this paper in computer-readable form as ancillary files in both *Mathematica* and *Python* format in the files `Zeta.m` and `Zeta.py`, respectively [209]. The provided quantities and their notation in either format are listed in Table II, while the variables they depend on can be found in Table III.

We provide the matching coefficients in two schemes for the flowed quarks, where this scheme can be chosen by setting the variable `Xzetachi` to 0 or 1 to get the $\overline{\mathrm{MS}}$ or the ringed scheme [see Eq. (27)]. The coefficients $c^{(2)}_\chi$ are denoted by `C2` and the function `chi2(nf)` in `Zeta.m` and `Zeta.py`, respectively. Using the replacement rule `ReplaceC2`, $c^{(2)}_\chi$ can be substituted by the values in Eq. (A17).

Additionally, the scheme related to the evanescent operators can be chosen by setting $E^i_{j,k}$ = `Eijepk` to any value. In particular, using the replacement rules `ReplaceScheme1`, the default scheme choice of this paper, which is used in both Eq. (70) as well as Eqs. (44) (45) (for the definition of this scheme see Section IV A) can be substituted. We also provide the explicit coefficients of the scheme used in Ref. [49] and Eq. (71) which can be replaced by `ReplaceScheme2`. Our results in the ancillary files are expressed in dependence of $T_R = \frac{1}{2}$.

APPENDIX D: CORRELATOR FITS

We now show the results of fits to Eq. (53) for all five bag parameters studied on each ensemble listed in Table I at select flow times, with p-values. The fits combine multiple source separations ΔT as described in Sec. VI and are fully correlated in both independent analyses.

Fits on the C1 and C2 ensembles are collected in Table IV, then on the M1, M2, and M3 ensembles in Table V, and finally for the F1S ensemble in Table VI.

Moreover, the fit results of the chiral-continuum limits for each bag parameter at a set of physical flow times are shown in Table VII.

TABLE IV. Bag parameters extracted from ratio fits for the coarse ensembles at select flow times with p-values.

Ens	τ[GeV^{-2}]	τ/a^2	$\mathcal{B}_1^{\mathrm{GF}}$	p	B_1^{GF}	p	B_2^{GF}	p	ϵ_1^{GF}	p	ϵ_2^{GF}	p
	0.094	0.30	0.8894(6)	0.67	1.0149(10)	0.85	0.9846(3)	0.94	−0.0919(2)	0.51	−0.00527(4)	0.95
	0.157	0.50	0.9099(6)	0.80	1.0097(9)	0.86	0.9875(3)	0.93	−0.0749(2)	0.54	−0.00538(4)	0.98
	0.220	0.70	0.9247(5)	0.70	1.0067(9)	0.87	0.9898(3)	0.87	−0.0623(2)	0.48	−0.00524(5)	0.98
C1	0.251	0.80	0.9305(5)	0.71	1.0057(9)	0.87	0.9908(3)	0.85	−0.0573(2)	0.51	−0.00512(5)	0.98
	0.314	1.00	0.9400(5)	0.86	1.0043(9)	0.89	0.9924(3)	0.92	−0.0489(2)	0.50	−0.00481(5)	0.98
	0.345	1.10	0.9440(5)	0.75	1.0038(9)	0.90	0.9931(3)	0.89	−0.0454(2)	0.55	−0.00464(6)	0.95
	0.408	1.30	0.9509(5)	0.63	1.0031(8)	0.91	0.9944(3)	0.94	−0.0395(2)	0.66	−0.00429(6)	0.96
	0.094	0.30	0.8889(6)	0.72	1.0117(5)	0.92	0.9817(4)	0.95	−0.0921(4)	0.49	−0.00556(15)	0.46
	0.157	0.50	0.9097(6)	0.64	1.0065(5)	0.94	0.9847(4)	0.95	−0.0752(4)	0.50	−0.0057(2)	0.43
	0.220	0.70	0.9243(6)	0.62	1.0035(5)	0.92	0.9871(4)	0.95	−0.0627(4)	0.64	−0.0056(2)	0.32
C2	0.251	0.80	0.9303(6)	0.54	1.0025(5)	0.91	0.9882(4)	0.96	−0.0577(4)	0.63	−0.0055(2)	0.32
	0.314	1.00	0.9396(5)	0.63	1.0011(4)	0.90	0.9900(4)	0.99	−0.0493(4)	0.71	−0.0052(2)	0.42
	0.345	1.10	0.9436(5)	0.62	1.0007(4)	0.89	0.9907(4)	1.00	−0.0458(3)	0.75	−0.0050(2)	0.30
	0.408	1.30	0.9505(5)	0.42	1.0000(4)	0.87	0.9920(4)	0.97	−0.0398(3)	0.86	−0.0047(2)	0.42

TABLE V. Bag parameters extracted from ratio fits for the medium ensembles at select flow times with p-values.

Ens	$\tau[\mathrm{GeV}^{-2}]$	τ/a^2	$\mathcal{B}_1^{\mathrm{GF}}$	p	B_1^{GF}	p	B_2^{GF}	p	ϵ_1^{GF}	p	ϵ_2^{GF}	p
	0.106	0.60	0.8901(6)	0.90	1.0139(6)	0.50	0.9830(6)	0.78	−0.0951(4)	0.93	−0.00610(5)	0.18
	0.158	0.90	0.9085(6)	0.88	1.0088(6)	0.57	0.9861(6)	0.82	−0.0783(4)	0.96	−0.00595(5)	0.10
	0.211	1.20	0.9218(7)	0.86	1.0057(6)	0.49	0.9884(7)	0.73	−0.0663(2)	0.24	−0.00565(6)	0.39
M1	0.246	1.40	0.9288(7)	0.82	1.0043(6)	0.60	0.9898(6)	0.86	−0.0599(2)	0.19	−0.00545(5)	0.43
	0.299	1.70	0.9373(6)	0.89	1.0028(6)	0.65	0.9914(6)	0.88	−0.0519(2)	0.12	−0.00513(6)	0.51
	0.352	2.00	0.9442(6)	0.78	1.0018(6)	0.67	0.9926(5)	0.97	−0.0455(2)	0.15	−0.00479(6)	0.68
	0.405	2.30	0.9500(6)	0.68	1.0012(6)	0.70	0.9937(5)	0.98	−0.0403(2)	0.18	−0.00447(6)	0.74
	0.106	0.60	0.8906(7)	0.28	1.0152(7)	0.20	0.9825(4)	0.54	−0.0957(3)	0.90	−0.00610(5)	0.76
	0.158	0.90	0.9089(7)	0.36	1.0099(6)	0.20	0.9856(4)	0.52	−0.0787(3)	0.86	−0.00595(6)	0.78
	0.211	1.20	0.9223(6)	0.43	1.0067(6)	0.14	0.9880(4)	0.49	−0.0665(3)	0.85	−0.00566(6)	0.79
M2	0.246	1.40	0.9293(6)	0.43	1.0053(7)	0.12	0.9893(4)	0.47	−0.0599(3)	0.85	−0.00545(7)	0.80
	0.299	1.70	0.9378(6)	0.48	1.0038(7)	0.13	0.9909(4)	0.39	−0.0518(2)	0.38	−0.00511(7)	0.84
	0.352	2.00	0.9448(6)	0.39	1.0027(6)	0.15	0.9923(4)	0.38	−0.0455(2)	0.38	−0.00479(7)	0.75
	0.405	2.30	0.9503(7)	0.47	1.0020(5)	0.06	0.9933(4)	0.44	−0.0402(3)	0.38	−0.00444(8)	0.82
	0.106	0.60	0.8910(7)	0.20	1.0133(7)	0.50	0.9824(3)	0.97	−0.0962(3)	0.27	−0.00634(8)	0.51
	0.158	0.90	0.9094(8)	0.24	1.0079(6)	0.50	0.9855(3)	0.99	−0.0793(3)	0.23	−0.00618(8)	0.26
	0.211	1.20	0.9227(7)	0.27	1.0044(7)	0.64	0.9880(3)	0.99	−0.0667(3)	0.52	−0.00584(9)	0.15
M3	0.246	1.40	0.9296(8)	0.26	1.0030(7)	0.65	0.9893(3)	0.99	−0.0603(2)	0.30	−0.00562(9)	0.15
	0.299	1.70	0.9383(8)	0.30	1.0015(6)	0.66	0.9910(3)	0.96	−0.0523(2)	0.31	−0.00537(11)	0.51
	0.352	2.00	0.9451(8)	0.34	1.0005(6)	0.68	0.9924(3)	0.92	−0.0458(2)	0.41	−0.00498(11)	0.37
	0.405	2.30	0.9508(7)	0.39	0.9999(6)	0.66	0.9935(3)	0.88	−0.0405(2)	0.44	−0.00470(12)	0.68

TABLE VI. Bag parameters extracted from ratio fits for the F1S ensemble at select flow times with p-values.

Ens	$\tau[\mathrm{GeV}^{-2}]$	τ/a^2	$\mathcal{B}_1^{\mathrm{GF}}$	p	B_1^{GF}	p	B_2^{GF}	p	ϵ_1^{GF}	p	ϵ_2^{GF}	p
	0.103	0.80	0.8888(5)	0.11	1.0156(3)	0.12	0.9828(2)	0.56	−0.0981(3)	0.84	−0.00629(3)	0.75
	0.155	1.20	0.9080(4)	0.05	1.0099(3)	0.11	0.9859(2)	0.51	−0.0804(3)	0.68	−0.00608(3)	0.76
	0.206	1.60	0.9211(4)	0.07	1.0066(3)	0.10	0.9883(2)	0.45	−0.0677(2)	0.83	−0.00578(4)	0.67
F1S	0.258	2.00	0.9311(4)	0.60	1.0044(3)	0.11	0.9901(2)	0.46	−0.0581(2)	0.73	−0.00546(3)	0.86
	0.309	2.40	0.9391(3)	0.61	1.0030(2)	0.12	0.9915(2)	0.47	−0.0506(2)	0.73	−0.00512(4)	0.63
	0.348	2.70	0.9440(4)	0.63	1.0023(2)	0.12	0.9925(2)	0.44	−0.0459(2)	0.72	−0.00486(5)	0.73
	0.400	3.10	0.9496(4)	0.64	1.0016(2)	0.21	0.9935(2)	0.44	−0.0407(2)	0.71	−0.00451(4)	0.74

TABLE VII. Chiral-continuum limit extrapolations of the bag parameters at select flow times with p-values.

Ens	$\tau[\mathrm{GeV}^{-2}]$	$\mathcal{B}_1^{\mathrm{GF}}$	p	B_1^{GF}	p	B_2^{GF}	p	ϵ_1^{GF}	p	ϵ_2^{GF}	p
	0.100	0.8845(8)	0.54	1.0172(10)	0.12	0.9800(4)	0.36	−0.1072(4)	0.05	−0.00716(6)	0.41
	0.150	0.9051(8)	0.64	1.0101(9)	0.15	0.9839(4)	0.27	−0.0866(4)	0.17	−0.00678(7)	0.45
	0.200	0.9192(8)	0.77	1.0059(9)	0.16	0.9867(4)	0.25	−0.0720(3)	0.24	−0.00630(7)	0.79
$a=0$	0.250	0.9295(8)	0.81	1.0033(9)	0.19	0.9887(4)	0.16	−0.0617(3)	0.26	−0.00589(7)	0.73
	0.300	0.9377(9)	0.73	1.0016(9)	0.19	0.9904(4)	0.10	−0.0533(3)	0.42	−0.00553(8)	0.53
	0.350	0.9442(8)	0.68	1.0006(9)	0.17	0.9917(4)	0.07	−0.0467(3)	0.64	−0.00512(9)	0.71
	0.400	0.9495(8)	0.72	0.9998(9)	0.17	0.9927(4)	0.05	−0.0414(3)	0.70	−0.00477(9)	0.57

[1] E. Gamiz, C. T. H. Davies, G. P. Lepage, J. Shigemitsu, and M. Wingate (HPQCD Collaboration), Neutral B meson mixing in unquenched lattice QCD, Phys. Rev. D **80**, 014503 (2009).

[2] S. Dürr *et al.* (BMW Collaboration), Precision computation of the kaon bag parameter, Phys. Lett. B **705**, 477 (2011).

[3] B. J. Choi *et al.* (SWME Collaboration), Kaon BSM B-parameters using improved staggered fermions from $N_f = 2 + 1$ unquenched QCD, Phys. Rev. D **93**, 014511 (2016).

[4] T. Blum *et al.* (RBC Collaboration and UKQCD Collaboration), Domain wall QCD with physical quark masses, Phys. Rev. D **93**, 074505 (2016).

[5] Y. Aoki, T. Ishikawa, T. Izubuchi, C. Lehner, and A. Soni, Neutral B meson mixings and B meson decay constants with static heavy and domain-wall light quarks, Phys. Rev. D **91**, 114505 (2015).

[6] P. A. Boyle, F. Erben, J. M. Flynn, N. Garron, J. Kettle, R. Mukherjee, and J. T. Tsang (RBC Collaboration and UKQCD Collaboration), Kaon mixing beyond the standard model with physical masses, Phys. Rev. D **110**, 034501 (2024).

[7] V. Bertone *et al.* (ETM Collaboration), Kaon Mixing Beyond the SM from $N_f = 2$ tmQCD and model independent constraints from the UTA, J. High Energy Phys. 03 (2013) 089; 07 (2013) 143.

[8] N. Carrasco *et al.* (ETM Collaboration), B-physics from $N_f = 2$ tmQCD: The Standard Model and beyond, J. High Energy Phys. 03 (2014) 016.

[9] N. Carrasco *et al.*, $D^0 - \bar{D}^0$ mixing in the standard model and beyond from $N_f = 2$ twisted mass QCD, Phys. Rev. D **90**, 014502 (2014).

[10] N. Carrasco, P. Dimopoulos, R. Frezzotti, V. Lubicz, G. C. Rossi, S. Simula, and C. Tarantino (ETM Collaboration), $\Delta S = 2$ and $\Delta C = 2$ bag parameters in the standard model and beyond from $N_f = 2 + 1 + 1$ twisted-mass lattice QCD, Phys. Rev. D **92**, 034516 (2015).

[11] J. Laiho and R. S. Van de Water, Pseudoscalar decay constants, light-quark masses, and B_K from mixed-action lattice QCD, Proc. Sci. LATTICE2011 (**2011**) 293.

[12] A. Bazavov *et al.*, Short-distance matrix elements for D^0-meson mixing for $N_f = 2 + 1$ lattice QCD, Phys. Rev. D **97**, 034513 (2018).

[13] A. Bazavov *et al.* (Fermilab Lattice Collaboration and MILC Collaboration), $B^0_{(s)}$-mixing matrix elements from lattice QCD for the Standard Model and beyond, Phys. Rev. D **93**, 113016 (2016).

[14] R. J. Dowdall, C. T. H. Davies, R. R. Horgan, G. P. Lepage, C. J. Monahan, J. Shigemitsu, and M. Wingate, Neutral B-meson mixing from full lattice QCD at the physical point, Phys. Rev. D **100**, 094508 (2019).

[15] R. S. Van de Water and S. R. Sharpe, B_K in staggered chiral perturbation theory, Phys. Rev. D **73**, 014003 (2006).

[16] J. A. Bailey, H.-J. Kim, W. Lee, and S. R. Sharpe, Kaon mixing matrix elements from beyond-the-Standard-Model operators in staggered chiral perturbation theory, Phys. Rev. D **85**, 074507 (2012).

[17] G. Martinelli, C. Pittori, C. T. Sachrajda, M. Testa, and A. Vladikas, A general method for non-perturbative renormalization of lattice operators, Nucl. Phys. **B445**, 81 (1995).

[18] C. Sturm, Y. Aoki, N. H. Christ, T. Izubuchi, C. T. C. Sachrajda, and A. Soni, Renormalization of quark bilinear operators in a momentum-subtraction scheme with a nonexceptional subtraction point, Phys. Rev. D **80**, 014501 (2009).

[19] P. A. Boyle, N. Garron, R. J. Hudspith, C. Lehner, and A. T. Lytle (RBC Collaboration and UKQCD Collaboration), Neutral kaon mixing beyond the Standard Model with $n_f = 2 + 1$ chiral fermions. Part 2: Non perturbative renormalisation of the $\Delta F = 2$ four-quark operators, J. High Energy Phys. 10 (2017) 054.

[20] Y. Aoki *et al.* (Flavour Lattice Averaging Group (FLAG)), FLAG review 2024, Phys. Rev. D **113**, 014508 (2026).

[21] N. Garron, R. J. Hudspith, and A. T. Lytle (RBC/UKQCD Collaboration), Neutral Kaon mixing beyond the Standard Model with $n_f = 2 + 1$ chiral fermions Part 1: Bare matrix elements and physical results, J. High Energy Phys. 11 (2016) 001.

[22] P. Boyle, F. Erben, A. Jüttner, T. Kaneko, M. Marshall, A. Portelli, O. Witzel, L. Del Debbio, and J. T. Tsang, BSM $B - \bar{B}$ mixing on JLQCD and RBC/UKQCD $N_f = 2 + 1$ DWF ensembles Proc. Sci., LATTICE2021 (**2022**) 224.

[23] L. Giusti, T. Harris, A. Nada, and S. Schaefer, Frequency-splitting estimators of single-propagator traces, Eur. Phys. J. C **79**, 586 (2019).

[24] P. A. Boyle, F. Erben, J. M. Flynn, V. Gülpers, R. C. Hill, R. Hodgson, A. Jüttner, F. Ó. hÓgáin, A. Portelli, and C. T. Sachrajda (RBC Collaboration and UKQCD Collaboration), Simulating rare kaon decays $K^+ \to \pi^+ \ell^+ \ell^-$ using domain wall lattice QCD with physical light quark masses, Phys. Rev. D **107**, L011503 (2023).

[25] G. Spanoudes, M. Costa, K. Mitsidi, and H. Panagopoulos, Classification of four-quark operators with $\Delta F \leq 2$ under flavor symmetry and their renormalization in a gauge-invariant scheme, Phys. Rev. D **113**, 034504 (2026).

[26] J. Lin, W. Detmold, and S. Meinel, Position-space renormalization schemes for four-quark operators in HQET, J. High Energy Phys. 07 (2024) 188.

[27] M. Di Pierro and C. T. Sachrajda (UKQCD Collaboration), A Lattice study of spectator effects in inclusive decays of B mesons, Nucl. Phys. **B534**, 373 (1998).

[28] M. Di Pierro, C. T. Sachrajda, and C. Michael (UKQCD Collaboration), An Exploratory lattice study of spectator effects in inclusive decays of the Λ_b baryon, Phys. Lett. B **468**, 143 (1999); **525**, 360(E) (2002).

[29] D. Becirevic, Theoretical progress in describing the B meson lifetimes, Proc. Sci. HEP2001 (**2001**) 098 [arXiv:hep-ph/0110124].

[30] J. Lin, W. Detmold, and S. Meinel, Lattice study of spectator effects in b-hadron decays, Proc. Sci. LATTICE2022 (**2023**) 417 [arXiv:2212.09275].

[31] R. Narayanan and H. Neuberger, Infinite N phase transitions in continuum Wilson loop operators, J. High Energy Phys. 03 (2006) 064.

[32] M. Lüscher, Trivializing maps, the Wilson flow and the HMC algorithm, Commun. Math. Phys. **293**, 899 (2010).

[33] M. Lüscher, Properties and uses of the Wilson flow in lattice QCD, J. High Energy Phys. 08 (2010) 071; 03 (2014) 092.
[34] M. Lüscher, Chiral symmetry and the Yang–Mills gradient flow, J. High Energy Phys. 04 (2013) 123.
[35] M. Lüscher and P. Weisz, Perturbative analysis of the gradient flow in non-Abelian gauge theories, J. High Energy Phys. 02 (2011) 051.
[36] H. Suzuki, Energy–momentum tensor from the Yang–Mills gradient flow, Prog. Theor. Exp. Phys. **2013**, 083B03 (2013); **2015**, 079201 (2015).
[37] M. Lüscher, Future applications of the Yang-Mills gradient flow in lattice QCD, Proc. Sci. LATTICE2013 (**2014**) 016 [arXiv:1308.5598].
[38] Y. Taniguchi, Non-perturbative renormalization of Kaon B parameter using gradient flow, in *Contribution to the 37th International Symposium on Lattice Field Theory*, https://indico.cern.ch/event/764552/contributions/3420565/ (2019).
[39] M. Black, R. V. Harlander, A. Hasenfratz, A. Rago, and O. Witzel, Renormalized quark masses using gradient flow, Phys. Rev. D **113**, 094504 (2026).
[40] A. Shindler, Moments of parton distribution functions of any order from lattice QCD, Phys. Rev. D **110**, L051503 (2024).
[41] R. V. Harlander, J. T. Kohnen, and A. Shindler, Short-flow-time expansion of non-singlet twist-two operators at next-to-next-to-leading order QCD, Eur. Phys. J. C **86**, 439 (2026).
[42] A. Francis *et al.*, Gradient flow for parton distribution functions: first application to the pion, Phys. Rev. Lett. **136**, 171903 (2026).
[43] A. Francis, P. Fritzsch, R. Karur, J. Kim, G. Pederiva, D. A. Pefkou, A. Rago, A. Shindler, A. Walker-Loud, and S. Zafeiropoulos, Moments of parton distributions functions of the pion from lattice QCD using gradient flow, Phys. Rev. D **113**, 074520 (2026).
[44] R. Edwards, J. Karpie, L. Maio, C. J. Monahan, K. Orginos, D. Richards, A. M. Sturzu, and S. Zafeiropoulos (HadStruc Collaboration), Accessing the gluon momentum fraction of nucleons through the gradient flow, Phys. Rev. D **114**, 014516 (2026).
[45] T. Iritani, M. Kitazawa, H. Suzuki, and H. Takaura, Thermodynamics in quenched QCD: Energy–momentum tensor with two-loop order coefficients in the gradient-flow formalism, Prog. Theor. Exp. Phys. **2019**, 023B02 (2019).
[46] Y. Taniguchi, S. Ejiri, K. Kanaya, M. Kitazawa, H. Suzuki, and T. Umeda (WHOT-QCD Collaboration), $N_f = 2 + 1$ QCD thermodynamics with gradient flow using two-loop matching coefficients, Phys. Rev. D **102**, 014510 (2020); **102**, 059903(E) (2020).
[47] P. Boyle, L. Del Debbio, and A. Khamseh, Massive momentum-subtraction scheme, Phys. Rev. D **95**, 054505 (2017).
[48] L. Del Debbio, F. Erben, J. M. Flynn, R. Mukherjee, and J. T. Tsang (RBC Collaboration and UKQCD Collaboration), Absorbing discretization effects with a massive renormalization scheme: The charm-quark mass, Phys. Rev. D **110**, 054512 (2024).
[49] M. Black, M. Lang, A. Lenz, and Z. Wüthrich, HQET sum rules for matrix elements of dimension-six four-quark operators for meson lifetimes within and beyond the Standard Model, J. High Energy Phys. 04 (2025) 081.
[50] M. Black, R. Harlander, F. Lange, A. Rago, A. Shindler, and O. Witzel, Using gradient flow to renormalise matrix elements for meson mixing and lifetimes, Proc. Sci. LATTICE2023 (**2024**) 263 [arXiv:2310.18059].
[51] M. Black, R. Harlander, F. Lange, A. Rago, A. Shindler, and O. Witzel, Gradient flow renormalisation for meson mixing and lifetimes, Proc. Sci. LATTICE2024 (**2025**) 243 [arXiv:2409.18891].
[52] M. Black, Improving Precision for Hadronic Observables in the Standard Model and Beyond, Ph.D. thesis, Universität Siegen, 2024, 10.25819/ubsi/10603.
[53] M. Black, R. V. Harlander, J. T. Kohnen, F. Lange, A. Rago, A. Shindler, and O. Witzel, companion Letter, Bag parameters for heavy meson lifetimes from a lattice QCD calculation at the $\mathrm{SU}(3)_{\mathrm{F}}$-symmetric point, Phys. Rev. Lett. **137**, 191905 (2026).
[54] V. A. Khoze and M. A. Shifman, Heavy quarks, Sov. Phys. Usp. **26**, 387 (1983).
[55] M. A. Shifman and M. B. Voloshin, Preasymptotic effects in inclusive weak decays of charmed particles, Sov. J. Nucl. Phys. **41**, 120 (1985).
[56] K. G. Wilson, Nonlagrangian models of current algebra, Phys. Rev. **179**, 1499 (1969).
[57] K. G. Wilson and J. B. Kogut, The Renormalization group and the epsilon expansion, Phys. Rep. **12**, 75 (1974).
[58] D. Buskulic *et al.* (ALEPH Collaboration), Improved measurement of the $B_d^0 - \bar{B}_d^0$ oscillation frequency, Z. Phys. C **75**, 397 (1997).
[59] P. Abreu *et al.* (DELPHI Collaboration), Measurement of $B_d^0 - \bar{B}_d^0$ oscillations, Z. Phys. C **76**, 579 (1997).
[60] J. Abdallah *et al.* (DELPHI Collaboration), Search for $B_s^0 - \bar{B}_s^0$ oscillations and a measurement of $B_d^0 - \bar{B}_d^0$ oscillations using events with an inclusively reconstructed vertex, Eur. Phys. J. C **28**, 155 (2003).
[61] K. Ackerstaff *et al.* (OPAL Collaboration), An updated study of B meson oscillations using dilepton events, Z. Phys. C **76**, 417 (1997).
[62] K. Ackerstaff *et al.* (OPAL Collaboration), A study of B meson oscillations using hadronic Z^0 decays containing leptons, Z. Phys. C **76**, 401 (1997).
[63] G. Abbiendi *et al.* (OPAL Collaboration), Measurement of the B^0 lifetime and oscillation frequency using $\bar{B}^0 \to D^{*+}\ell^-$ anti-neutrino decays, Phys. Lett. B **493**, 266 (2000).
[64] F. Abe *et al.* (CDF Collaboration), Measurement of the $B^0 - \bar{B}^0$ oscillation frequency using $\pi - B$ meson charge-flavor correlations in $p\bar{p}$ collisions at $\sqrt{s} = 1.8$ TeV, Phys. Rev. Lett. **80**, 2057 (1998).
[65] F. Abe *et al.* (CDF Collaboration), Measurement of the $B_d^0 - \bar{B}_d^0$ flavor oscillation frequency and study of same side flavor tagging of B mesons in $p\bar{p}$ collisions, Phys. Rev. D **59**, 032001 (1999).
[66] F. Abe *et al.* (CDF Collaboration), Measurement of the $B_d^0\bar{B}_d^0$ oscillation frequency using dimuon data in $p\bar{p}$ collisions at $\sqrt{s} = 1.8$ TeV, Phys. Rev. D **60**, 051101 (1999).

[67] F. Abe *et al.* (CDF Collaboration), Measurement of $B^0 - \bar{B}^0$ flavor oscillations using jet-charge and lepton flavor tagging in $p\bar{p}$ collisions at $\sqrt{s} = 1.8$ TeV, Phys. Rev. D **60**, 072003 (1999).

[68] T. Affolder *et al.* (CDF Collaboration), Measurement of the $B^0\bar{B}^0$ oscillation frequency using $\ell^- D^{*+}$ pairs and lepton flavor tags, Phys. Rev. D **60**, 112004 (1999).

[69] M. Acciarri *et al.* (L3 Collaboration), Measurement of the $B_d^0 - \bar{B}_d^0$ oscillation frequency, Eur. Phys. J. C **5**, 195 (1998).

[70] B. Aubert *et al.* (*BABAR* Collaboration), Measurement of $B^0 - \bar{B}^0$ flavor oscillations in hadronic B^0 decays, Phys. Rev. Lett. **88**, 221802 (2002).

[71] B. Aubert *et al.* (*BABAR* Collaboration), Measurement of the $B^0 - \bar{B}^0$ oscillation frequency with inclusive dilepton events, Phys. Rev. Lett. **88**, 221803 (2002).

[72] B. Aubert *et al.* (*BABAR* Collaboration), A study of time dependent CP-violating asymmetries and flavor oscillations in neutral B decays at the $\Upsilon(4S)$, Phys. Rev. D **66**, 032003 (2002).

[73] B. Aubert *et al.* (*BABAR* Collaboration), Simultaneous measurement of the B^0 meson lifetime and mixing frequency with $B^0 \to D^{*-}\ell^+\nu_\ell$ decays, Phys. Rev. D **67**, 072002 (2003).

[74] B. Aubert *et al.* (*BABAR* Collaboration), Measurement of the $\bar{B}^0$ lifetime and the $B^0\bar{B}^0$ oscillation frequency using partially reconstructed $\bar{B}^0 \to D^{*+}\ell^-\bar{\nu}_\ell$ decays, Phys. Rev. D **73**, 012004 (2006).

[75] N. C. Hastings *et al.* (Belle Collaboration), Studies of $B^0 - \bar{B}^0$ mixing properties with inclusive dilepton events, Phys. Rev. D **67**, 052004 (2003).

[76] Y. Zheng *et al.* (Belle Collaboration), Measurement of the $B^0 - \bar{B}^0$ mixing rate with $B^0(\bar{B}^0) \to D^{*\mp}\pi^\pm$ partial reconstruction, Phys. Rev. D **67**, 092004 (2003).

[77] K. Abe *et al.* (Belle Collaboration), Improved measurement of CP-violation parameters $\sin 2\phi_1$ and $|\lambda|$, B meson lifetimes, and $B^0 - \bar{B}^0$ mixing parameter Δm_d, Phys. Rev. D **71**, 072003 (2005); **71**, 079903(E) (2005).

[78] F. Abudinén *et al.* (Belle-II Collaboration), Measurement of the B^0 lifetime and flavor-oscillation frequency using hadronic decays reconstructed in 2019–2021 Belle II data, Phys. Rev. D **107**, L091102 (2023).

[79] R. Aaij *et al.* (LHCb Collaboration), Measurement of the $B^0 - \bar{B}^0$ oscillation frequency Δm_d with the decays $B^0 \to D^-\pi^+$ and $B^0 \to J/\psi K^{*0}$, Phys. Lett. B **719**, 318 (2013).

[80] R. Aaij *et al.* (LHCb Collaboration), Observation of $B_s^0 - \bar{B}_s^0$ mixing and measurement of mixing frequencies using semileptonic B decays, Eur. Phys. J. C **73**, 2655 (2013).

[81] R. Aaij *et al.* (LHCb Collaboration), A precise measurement of the B^0 meson oscillation frequency, Eur. Phys. J. C **76**, 412 (2016).

[82] A. Abulencia *et al.* (CDF Collaboration), Observation of $B_s^0 - \bar{B}_s^0$ Oscillations, Phys. Rev. Lett. **97**, 242003 (2006).

[83] R. Aaij *et al.* (LHCb Collaboration), Measurement of the $B_s^0 - \bar{B}_s^0$ oscillation frequency Δm_s in $B_s^0 \to D_s^-(3)\pi$ decays, Phys. Lett. B **709**, 177 (2012).

[84] R. Aaij *et al.* (LHCb Collaboration), Precision measurement of the $B_s^0 - \bar{B}_s^0$ oscillation frequency with the decay $B_s^0 \to D_s^-\pi^+$, New J. Phys. **15**, 053021 (2013).

[85] R. Aaij *et al.* (LHCb Collaboration), Precision measurement of CP violation in $B_s^0 \to J/\psi K^+K^-$ decays, Phys. Rev. Lett. **114**, 041801 (2015).

[86] R. Aaij *et al.* (LHCb Collaboration), Measurement of the CKM angle γ and $B_s^0 - \bar{B}_s^0$ mixing frequency with $B_s^0 \to D_s^\mp h^\pm\pi^\pm\pi^\mp$ decays, J. High Energy Phys. 03 (2021) 137.

[87] R. Aaij *et al.* (LHCb Collaboration), Precise determination of the $B_s^0 - \bar{B}_s^0$ oscillation frequency, Nat. Phys. **18**, 1 (2022).

[88] I. Bezshyiko *et al.* (LHCb Collaboration), Improved measurement of CP violation parameters in $B_s^0 \to J/\psi K^+K^-$ decays in the vicinity of the $\phi(1020)$ resonance, Phys. Rev. Lett. **132**, 051802 (2024).

[89] A. M. Sirunyan *et al.* (CMS Collaboration), Measurement of the CP-violating phase ϕ_s in the $B_s^0 \to J/\psi\phi(1020) \to \mu^+\mu^-K^+K^-$ channel in proton-proton collisions at $s = 13$ TeV, Phys. Lett. B **816**, 136188 (2021).

[90] M. Staric *et al.* (Belle Collaboration), Evidence for $D^0 - \bar{D}^0$ mixing, Phys. Rev. Lett. **98**, 211803 (2007).

[91] B. Aubert *et al.* (*BABAR* Collaboration), Evidence for $D^0 - \bar{D}^0$ mixing, Phys. Rev. Lett. **98**, 211802 (2007).

[92] T. Aaltonen *et al.* (CDF Collaboration), Evidence for $D^0 - \bar{D}^0$ mixing using the CDF II detector, Phys. Rev. Lett. **100**, 121802 (2008).

[93] R. Aaij *et al.* (LHCb Collaboration), Observation of $D^0 - \bar{D}^0$ oscillations, Phys. Rev. Lett. **110**, 101802 (2013).

[94] T. A. Aaltonen *et al.* (CDF Collaboration), Observation of $D^0 - \bar{D}^0$ mixing using the CDF II detector, Phys. Rev. Lett. **111**, 231802 (2013).

[95] B. R. Ko *et al.* (Belle Collaboration), Observation of $D^0 - \bar{D}^0$ mixing in e^+e^- collisions, Phys. Rev. Lett. **112**, 111801 (2014); **112**, 139903(A) (2014).

[96] R. Aaij *et al.* (LHCb Collaboration), First observation of $D^0 - \bar{D}^0$ oscillations in $D^0 \to K^+\pi^-\pi^+\pi^-$ decays and measurement of the associated coherence parameters, Phys. Rev. Lett. **116**, 241801 (2016).

[97] R. Aaij *et al.* (LHCb Collaboration), Measurement of the charm-mixing parameter y_{CP}, Phys. Rev. Lett. **122**, 011802 (2019).

[98] R. Aaij *et al.* (LHCb Collaboration), Measurement of the mass difference between neutral charm-meson eigenstates, Phys. Rev. Lett. **122**, 231802 (2019).

[99] R. Aaij *et al.* (LHCb Collaboration), Observation of the mass difference between neutral charm-meson eigenstates, Phys. Rev. Lett. **127**, 111801 (2021).

[100] R. Aaij *et al.* (LHCb Collaboration), Simultaneous determination of CKM angle γ and charm mixing parameters, J. High Energy Phys. 12 (2021) 141.

[101] R. Aaij *et al.* (LHCb Collaboration), Measurement of the charm mixing parameter $y_{CP} - y_{CP}^{K\pi}$ using two-body D^0 meson decays, Phys. Rev. D **105**, 092013 (2022).

[102] R. Aaij *et al.* (LHCb Collaboration), Measurement of $D^0 - \bar{D}^0$ mixing and search for CP violation with $D^0 \to K^+\pi$ decays, Phys. Rev. D **111**, 012001 (2025).

[103] LHCb Collaboration, Simultaneous determination of the CKM angle γ and parameters related to mixing and CP violation in the charm sector 10.17181/CERN.8CUC.W3FT (2024).

[104] R. Aaij *et al.* (LHCb Collaboration), Search for charge-parity violation in semileptonically tagged $D^0 \to K^+\pi^-$ decays, J. High Energy Phys. 03 (2025) 149.
[105] I. Adachi *et al.* (Belle Collaboration and Belle-II Collaboration), Model-independent measurement of $D^0 - \bar{D}^0$ mixing parameters in $D^0 \to K^0_S\pi^+\pi^-$ decays at Belle and Belle II, Phys. Rev. D **111**, 112011 (2025).
[106] S. Banerjee *et al.* (Heavy Flavor Averaging Group (HFLAV) Collaboration), Averages of b-hadron, c-hadron, and τ-lepton properties as of 2023, Phys. Rev. D **113**, 012008 (2026).
[107] A. Lenz and G. Wilkinson, Mixing and CP violation in the charm system, Annu. Rev. Nucl. Part. Sci. **71**, 59 (2021).
[108] M. Di Carlo, F. Erben, and M. T. Hansen, Long distance contributions to neutral D-meson mixing from lattice QCD, J. High Energy Phys. 07 (2025) 229.
[109] M. Artuso, G. Borissov, and A. Lenz, CP violation in the B^0_s system, Rev. Mod. Phys. **88**, 045002 (2016); **91**, 049901(A) (2019).
[110] R. Harlander, S. Klein, and M. Lipp, FeynGame, Comput. Phys. Commun. **256**, 107465 (2020).
[111] L. Bündgen, R. V. Harlander, S. Y. Klein, and M. C. Schaaf, FeynGame 3.0, Comput. Phys. Commun. **314**, 109662 (2025).
[112] T. Inami and C. S. Lim, Effects of superheavy quarks and leptons in low-energy weak processes $K_L \to \mu\bar{\mu}$, $K^+ \to \pi^+\nu\bar{\nu}$ and $K^0 \leftrightarrow \bar{K}^0$, Prog. Theor. Phys. **65**, 297 (1981); **65**, 1772(E) (1981).
[113] A. J. Buras, M. Jamin, and P. H. Weisz, Leading and next-to-leading QCD corrections to ϵ parameter and $B^0 - \bar{B}^0$ mixing in the presence of a heavy top quark, Nucl. Phys. **B347**, 491 (1990).
[114] S. Navas *et al.* (Particle Data Group), Review of particle physics, Phys. Rev. D **110**, 030001 (2024).
[115] A. G. Grozin, R. Klein, T. Mannel, and A. A. Pivovarov, $B^0 - \bar{B}^0$ mixing at next-to-leading order, Phys. Rev. D **94**, 034024 (2016).
[116] M. Kirk, A. Lenz, and T. Rauh, Dimension-six matrix elements for meson mixing and lifetimes from sum rules, J. High Energy Phys. 12 (2017) 068; 06 (2020) 162(E).
[117] M. J. Kirk, Charming new physics in beautiful processes?, Ph.D. thesis, Durham University, IPPP, 2018, 10.1007/978-3-030-19197-9.
[118] D. King, A. Lenz, and T. Rauh, B_s mixing observables and $|V_{td}/V_{ts}|$ from sum rules, J. High Energy Phys. 05 (2019) 034.
[119] C. T. H. Davies, J. Harrison, G. P. Lepage, C. J. Monahan, J. Shigemitsu, and M. Wingate (HPQCD Collaboration), Lattice QCD matrix elements for the $B^0_s - \bar{B}^0_s$ width difference beyond leading order, Phys. Rev. Lett. **124**, 082001 (2020).
[120] P. Abreu *et al.* (DELPHI Collaboration), A measurement of B^+ and B^0 lifetimes using $\bar{D}\ell^+$ events, Z. Phys. C **68**, 13 (1995).
[121] W. Adam *et al.* (DELPHI Collaboration), Lifetimes of charged and neutral B hadrons using event topology, Z. Phys. C **68**, 363 (1995).
[122] P. Abreu *et al.* (DELPHI Collaboration), A precise measurement of the B^0_d meson lifetime using a new technique, Z. Phys. C **74**, 19 (1997); **75**, 579(E) (1997).
[123] P. Abreu *et al.* (DELPHI Collaboration), Study of $B^0_s - \bar{B}^0_s$ oscillations and B^0_s lifetimes using hadronic decays of B^0_s mesons, Eur. Phys. J. C **18**, 229 (2000).
[124] J. Abdallah *et al.* (DELPHI Collaboration), A precise measurement of the B^+, B^0 and mean b hadron lifetime with the DELPHI detector at LEP1, Eur. Phys. J. C **33**, 307 (2004).
[125] P. Abreu *et al.* (DELPHI Collaboration), Measurement of the B^0_s lifetime and study of $B^0_s - \bar{B}^0_s$ oscillations using $D_s\ell$ events, Eur. Phys. J. C **16**, 555 (2000).
[126] D. Buskulic *et al.* (ALEPH Collaboration), Improved measurement of the $\bar{B}^0$ and B^- meson lifetimes, Z. Phys. C **71**, 31 (1996).
[127] R. Barate *et al.* (ALEPH Collaboration), Study of B^0_s oscillations and lifetime using fully reconstructed D_s—decays, Eur. Phys. J. C **4**, 367 (1998).
[128] R. Barate *et al.* (ALEPH Collaboration), Measurement of the $\bar{B}^0$ and B^- meson lifetimes, Phys. Lett. B **492**, 275 (2000).
[129] R. Barate *et al.* (ALEPH Collaboration), A study of the decay width difference in the $B^0_s - \bar{B}^0_s$ system using $\phi\phi$ correlations, Phys. Lett. B **486**, 286 (2000).
[130] M. Acciarri *et al.* (L3 Collaboration), Upper limit on the lifetime difference of shortlived and longlived B^0_s mesons, Phys. Lett. B **438**, 417 (1998).
[131] R. Akers *et al.* (OPAL Collaboration), Improved measurements of the B^0 and B^+ meson lifetimes, Z. Phys. C **67**, 379 (1995).
[132] K. Ackerstaff *et al.* (OPAL Collaboration), A measurement of the B^0_s lifetime using reconstructed D^-_s—mesons, Eur. Phys. J. C **2**, 407 (1998).
[133] K. Ackerstaff *et al.* (OPAL Collaboration), Measurements of the B^0_s and Λ^0_b lifetimes, Phys. Lett. B **426**, 161 (1998).
[134] G. Abbiendi *et al.* (OPAL Collaboration), Measurement of the B^+ and B^0 lifetimes and search for CP(T) violation using reconstructed secondary vertices, Eur. Phys. J. C **12**, 609 (2000).
[135] K. Abe *et al.* (SLD Collaboration), Measurement of the B^+ and B^0 lifetimes using topological reconstruction of inclusive and semileptonic decays, Phys. Rev. Lett. **79**, 590 (1997).
[136] F. Abe *et al.* (CDF Collaboration), Measurement of B hadron lifetimes using J/ψ final states at CDF, Phys. Rev. D **57**, 5382 (1998).
[137] F. Abe *et al.* (CDF Collaboration), Improved measurement of the B^- and $\bar{B}^0$ meson lifetimes using semileptonic decays, Phys. Rev. D **58**, 092002 (1998).
[138] F. Abe *et al.* (CDF Collaboration), Measurement of the B^0_s meson lifetime using semileptonic decays, Phys. Rev. D **59**, 032004 (1999).
[139] D. Acosta *et al.* (CDF Collaboration), Measurement of B meson lifetimes using fully reconstructed B decays produced in $p\bar{p}$ collisions at $\sqrt{s} = 1.8$ TeV, Phys. Rev. D **65**, 092009 (2002).
[140] T. Aaltonen *et al.* (CDF Collaboration), Measurement of b hadron lifetimes in exclusive decays containing a J/ψ in p^- pbar collisions at $\sqrt{s} = 1.96$ TeV, Phys. Rev. Lett. **106**, 121804 (2011).

[141] T. Aaltonen *et al.* (CDF Collaboration), Measurement of the B^- lifetime using a simulation free approach for trigger bias correction, Phys. Rev. D **83**, 032008 (2011).

[142] T. Aaltonen *et al.* (CDF Collaboration), Measurement of the B_s lifetime in fully and partially reconstructed $B_s \to D_s^-(\phi\pi^-)X$ decays in $\bar{p}-p$ collisions at $\sqrt{s} = 1.96$ TeV, Phys. Rev. Lett. **107**, 272001 (2011).

[143] T. Aaltonen *et al.* (CDF Collaboration), Measurement of branching ratio and B_s^0 lifetime in the decay $B_s^0 \to J/\psi f_0(980)$ at CDF, Phys. Rev. D **84**, 052012 (2011).

[144] T. Aaltonen *et al.* (CDF Collaboration), Measurement of the bottom-strange meson mixing phase in the full CDF data set, Phys. Rev. Lett. **109**, 171802 (2012).

[145] V. M. Abazov *et al.* (D0 Collaboration), Measurement of the ratio of B^+ and B^0 meson lifetimes, Phys. Rev. Lett. **94**, 182001 (2005).

[146] V. M. Abazov *et al.* (D0 Collaboration), Measurement of the B_s^0 lifetime in the exclusive decay channel $B_s^0 \to J/\psi\phi$, Phys. Rev. Lett. **94**, 042001 (2005).

[147] V. M. Abazov *et al.* (D0 Collaboration), Measurement of the angular and lifetime parameters of the decays $B_d^0 \to J/\psi K^{*0}$ and $B_s^0 \to J/\psi\phi$, Phys. Rev. Lett. **102**, 032001 (2009).

[148] V. M. Abazov *et al.* (D0 Collaboration), Measurement of the CP-violating phase $\phi_s^{J/\psi\phi}$ using the flavor-tagged decay $B_s^0 \to J/\psi\phi$ in 8 fb^{-1} of $p\bar{p}$ collisions, Phys. Rev. D **85**, 032006 (2012).

[149] V. M. Abazov *et al.* (D0 Collaboration), Measurement of the B_s^0 lifetime in the flavor-specific decay channel $B_s^0 \to D_s^-\mu^+\nu X$, Phys. Rev. Lett. **114**, 062001 (2015).

[150] V. M. Abazov *et al.* (D0 Collaboration), B_s^0 lifetime measurement in the CP-odd decay channel $B_s^0 \to J/\psi f_0(980)$, Phys. Rev. D **94**, 012001 (2016).

[151] B. Aubert *et al.* (*BABAR* Collaboration), Measurement of the B^0 and B^+ meson lifetimes with fully reconstructed hadronic final states, Phys. Rev. Lett. **87**, 201803 (2001).

[152] B. Aubert *et al.* (*BABAR* Collaboration), Measurement of the B^0 lifetime with partially reconstructed $B^0 \to D^{*-}\ell^+\nu_\ell$ decays, Phys. Rev. Lett. **89**, 011802 (2002); **89**, 169903 (E) (2002).

[153] B. Aubert *et al.* (*BABAR* Collaboration), Measurement of the B^0 meson lifetime with partial reconstruction of $B^0 \to D^{*-}\pi^+$ and $B^0 \to D^{*-}\rho^+$ decays, Phys. Rev. D **67**, 091101 (2003).

[154] G. Aad *et al.* (ATLAS Collaboration), Flavor tagged time-dependent angular analysis of the $B_s \to J/\psi\phi$ decay and extraction of $\Delta\Gamma_s$ and the weak phase ϕ_s in ATLAS, Phys. Rev. D **90**, 052007 (2014).

[155] G. Aad *et al.* (ATLAS Collaboration), Measurement of the CP-violating phase ϕ_s and the B_s^0 meson decay width difference with $B_s^0 \to J/\psi\phi$ decays in ATLAS, J. High Energy Phys. 08 (2016) 147.

[156] G. Aad *et al.* (ATLAS Collaboration), Measurement of the CP-violating phase ϕ_s in $B_s^0 \to J/\psi\phi$ decays in ATLAS at 13 TeV, Eur. Phys. J. C **81**, 342 (2021).

[157] V. Khachatryan *et al.* (CMS Collaboration), Measurement of the CP-violating weak phase ϕ_s and the decay width difference $\Delta\Gamma_s$ using the $B_s^0 \to J/\psi\phi(1020)$ decay channel in pp collisions at $\sqrt{s} = 8$ TeV, Phys. Lett. B **757**, 97 (2016).

[158] A. M. Sirunyan *et al.* (CMS Collaboration), Measurement of b hadron lifetimes in pp collisions at $\sqrt{s} = 8$ TeV, Eur. Phys. J. C **78**, 457 (2018); **78**, 561(E) (2018).

[159] A. M. Sirunyan *et al.* (CMS Collaboration), Measurement of properties of $B_s^0 \to \mu^+\mu^-$ decays and search for $B^0 \to \mu^+\mu^-$ with the CMS experiment, J. High Energy Phys. 04 (2019) 188.

[160] R. Aaij *et al.* (LHCb Collaboration), Measurement of the effective $B_s^0 \to K^+K^-$ lifetime, Phys. Lett. B **707**, 349 (2012).

[161] R. Aaij *et al.* (LHCb Collaboration), Measurement of the effective $B_s^0 \to J/\psi K_S^0$ lifetime, Nucl. Phys. **B873**, 275 (2013).

[162] R. Aaij *et al.* (LHCb Collaboration), Measurement of the $\bar{B}_s^0 \to D_s^-D_s^+$ and $\bar{B}_s^0 \to D^-D_s^+$ effective lifetimes, Phys. Rev. Lett. **112**, 111802 (2014).

[163] R. Aaij *et al.* (LHCb Collaboration), Measurement of CP violation and the B_s^0 meson decay width difference with $B_s^0 \to J/\psi K^+K^-$ and $B_s^0 \to J/\psi\pi^+\pi^-$ decays, Phys. Rev. D **87**, 112010 (2013).

[164] R. Aaij *et al.* (LHCb Collaboration), Measurements of the B^+, B^0, B_s^0 meson and Λ_b^0 baryon lifetimes, J. High Energy Phys. 04 (2014) 114.

[165] R. Aaij *et al.* (LHCb Collaboration), Effective lifetime measurements in the $B_s^0 \to K^+K^-$, $B^0 \to K^+\pi^-$ and $B_s^0 \to \pi^+K^-$ decays, Phys. Lett. B **736**, 446 (2014).

[166] R. Aaij *et al.* (LHCb Collaboration), Measurement of the $\bar{B}_s^0$ meson lifetime in $D_s^+\pi^-$ decays, Phys. Rev. Lett. **113**, 172001 (2014).

[167] R. Aaij *et al.* (LHCb Collaboration), Measurement of the $B_s^0 \to J/\psi\eta$ lifetime, Phys. Lett. B **762**, 484 (2016).

[168] R. Aaij *et al.* (LHCb Collaboration), First study of the CP -violating phase and decay-width difference in $B_s^0 \to \psi(2S)\phi$ decays, Phys. Lett. B **762**, 253 (2016).

[169] R. Aaij *et al.* (LHCb Collaboration), Measurement of B_s^0 and D_s^- meson lifetimes, Phys. Rev. Lett. **119**, 101801 (2017).

[170] R. Aaij *et al.* (LHCb Collaboration), Resonances and CP violation in B_s^0 and $\bar{B}_s^0 \to J/\psi K^+K^-$ decays in the mass region above the $\phi(1020)$, J. High Energy Phys. 08 (2017) 037.

[171] R. Aaij *et al.* (LHCb Collaboration), Measurement of the CP-violating phase ϕ_s from $B_s^0 \to J/\psi\pi^+\pi^-$ decays in 13 TeV pp collisions, Phys. Lett. B **797**, 134789 (2019).

[172] R. Aaij *et al.* (LHCb Collaboration), Updated measurement of time-dependent CP-violating observables in $B_s^0 \to J/\psi K^+K^-$ decays, Eur. Phys. J. C **79**, 706 (2019); **80**, 601 (E) (2020).

[173] R. Aaij *et al.* (LHCb Collaboration), First measurement of the CP-violating phase in $B_s^0 \to J/\psi(\to e^+e^-)\phi$ decays, Eur. Phys. J. C **81**, 1026 (2021).

[174] R. Aaij *et al.* (LHCb Collaboration), Measurement of the $B_s^0 \to \mu^+\mu^-$ decay properties and search for the $B^0 \to \mu^+\mu^-$ and $B_s^0 \to \mu^+\mu^-\gamma$ decays, Phys. Rev. D **105**, 012010 (2022).

[175] J. R. Raab *et al.* (Tagged Photon Spectrometer Collaboration), Measurement of the D^0, D^+ and D_s^+ lifetimes, Phys. Rev. D **37**, 2391 (1988).
[176] P. L. Frabetti *et al.* (E687 Collaboration), A precise measurement of the $D_S^{\pm}$ meson lifetime, Phys. Rev. Lett. **71**, 827 (1993).
[177] P. L. Frabetti *et al.* (E687 Collaboration), Precise measurements of the D^0 and D^+ meson lifetimes, Phys. Lett. B **323**, 459 (1994).
[178] E. M. Aitala *et al.* (E791 Collaboration), Measurement of the D_s lifetime, Phys. Lett. B **445**, 449 (1999).
[179] E. M. Aitala *et al.* (E791 Collaboration), Measurements of lifetimes and a limit on the lifetime difference in the neutral D meson system, Phys. Rev. Lett. **83**, 32 (1999).
[180] G. Bonvicini *et al.* (CLEO Collaboration), Measurement of charm meson lifetimes, Phys. Rev. Lett. **82**, 4586 (1999).
[181] A. Kushnirenko *et al.* (SELEX Collaboration), Precision measurements of the Λ_c^+ and D^0 lifetimes, Phys. Rev. Lett. **86**, 5243 (2001).
[182] M. Iori *et al.* (SELEX Collaboration), Measurement of the $D_s^{\pm}$ lifetime, Phys. Lett. B **523**, 22 (2001).
[183] J. M. Link *et al.* (FOCUS Collaboration), New measurements of the D^0 and D^+ lifetimes, Phys. Lett. B **537**, 192 (2002).
[184] J. M. Link *et al.* (FOCUS Collaboration), A measurement of the D_s^+ lifetime, Phys. Rev. Lett. **95**, 052003 (2005).
[185] F. Abudinén *et al.* (Belle-II Collaboration), Precise measurement of the D^0 and D^+ lifetimes at Belle II, Phys. Rev. Lett. **127**, 211801 (2021).
[186] I. Adachi *et al.* (Belle-II Collaboration), Precise measurement of the D_s^+ lifetime at Belle II, Phys. Rev. Lett. **131**, 171803 (2023).
[187] D. King, A. Lenz, M. L. Piscopo, T. Rauh, A. V. Rusov, and C. Vlahos, Revisiting inclusive decay widths of charmed mesons, J. High Energy Phys. 08 (2021) 241.
[188] J. Albrecht, F. Bernlochner, A. Lenz, and A. Rusov, Lifetimes of b-hadrons and mixing of neutral B-mesons: Theoretical and experimental status, Eur. Phys. J. Special Topics **233**, 359 (2024).
[189] M. L. Piscopo, Higher order corrections to the lifetime of heavy hadrons, Ph.D. thesis, Siegen University, 2021, 10.25819/ubsi/10024.
[190] B. Guberina, S. Nussinov, R. D. Peccei, and R. Rückl, D meson lifetimes and decays, Phys. Lett. B **89**, 111 (1979).
[191] M. A. Shifman and M. B. Voloshin, Hierarchy of lifetimes of charmed and beautiful hadrons, Sov. Phys. JETP **64**, 698 (1986).
[192] N. G. Uraltsev, On the problem of boosting nonleptonic b baryon decays, Phys. Lett. B **376**, 303 (1996).
[193] M. Neubert and C. T. Sachrajda, Spectator effects in inclusive decays of beauty hadrons, Nucl. Phys. **B483**, 339 (1997).
[194] M. Beneke, G. Buchalla, C. Greub, A. Lenz, and U. Nierste, The $B^+ - B_d^0$ lifetime difference beyond leading logarithms, Nucl. Phys. **B639**, 389 (2002).
[195] E. Franco, V. Lubicz, F. Mescia, and C. Tarantino, Lifetime ratios of beauty hadrons at the next-to-leading order in QCD, Nucl. Phys. **B633**, 212 (2002).
[196] A. Lenz and T. Rauh, D-meson lifetimes within the heavy quark expansion, Phys. Rev. D **88**, 034004 (2013).
[197] F. Gabbiani, A. I. Onishchenko, and A. A. Petrov, Λ_b lifetime puzzle in heavy quark expansion, Phys. Rev. D **68**, 114006 (2003).
[198] F. Gabbiani, A. I. Onishchenko, and A. A. Petrov, Spectator effects and lifetimes of heavy hadrons, Phys. Rev. D **70**, 094031 (2004).
[199] D. King, A. Lenz, and T. Rauh, SU(3) breaking effects in B and D meson lifetimes, J. High Energy Phys. 06 (2022) 134.
[200] D. J. King, Three loop corrections to HQET sum rules for the bag parameter, Ph.D. thesis, Durham University, 2022.
[201] J. Artz, R. V. Harlander, F. Lange, T. Neumann, and M. Prausa, Results and techniques for higher order calculations within the gradient-flow formalism, J. High Energy Phys. 06 (2019) 121; 10 (2019) 032(E).
[202] K. Hieda, H. Makino, and H. Suzuki, Proof of the renormalizability of the gradient flow, Nucl. Phys. **B918**, 23 (2017).
[203] H. Makino and H. Suzuki, Lattice energy–momentum tensor from the Yang–Mills gradient flow—inclusion of fermion fields, Prog. Theor. Exp. Phys. **2014**, 063B02 (2014); **2015**, 079202(E) (2015).
[204] J. Kim, T. Luu, M. D. Rizik, and A. Shindler (SymLat Collaboration), Nonperturbative renormalization of the quark chromoelectric dipole moment with the gradient flow: Power divergences, Phys. Rev. D **104**, 074516 (2021).
[205] A. J. Buras and P. H. Weisz, QCD nonleading corrections to weak decays in dimensional regularization and 't Hooft-Veltman schemes, Nucl. Phys. **B333**, 66 (1990).
[206] M. J. Dugan and B. Grinstein, On the vanishing of evanescent operators, Phys. Lett. B **256**, 239 (1991).
[207] S. Herrlich and U. Nierste, Evanescent operators, scheme dependences and double insertions, Nucl. Phys. **B455**, 39 (1995).
[208] M. Fierz, Zur Fermischen Theorie des β-Zerfalls, Z. Phys. **104**, 553 (1937).
[209] See Supplemental Material at http://link.aps.org/supplemental/10.1103/47j9-h8s5 for the perturbative results of this work.
[210] R. V. Harlander and F. Lange, Effective electroweak Hamiltonian in the gradient-flow formalism, Phys. Rev. D **105**, L071504 (2022).
[211] S. G. Gorishnii, S. A. Larin, and F. V. Tkachov, The algorithm for OPE coefficient functions in the MS scheme, Phys. Lett. B **124**, 217 (1983).
[212] S. G. Gorishnii and S. A. Larin, Coefficient functions of asymptotic operator expansions in minimal subtraction scheme, Nucl. Phys. **B283**, 452 (1987).
[213] R. V. Harlander, Y. Kluth, and F. Lange, The two-loop energy–momentum tensor within the gradient-flow formalism, Eur. Phys. J. C **78**, 944 (2018); **79**, 858(E) (2019).
[214] P. Nogueira, Automatic Feynman graph generation, J. Comput. Phys. **105**, 279 (1993).
[215] P. Nogueira, Abusing QGRAF, Nucl. Instrum. Methods Phys. Res., Sect. A **559**, 220 (2006).
[216] R. Harlander, T. Seidensticker, and M. Steinhauser, Corrections of $O(\alpha\alpha_s)$ to the decay of the Z boson into bottom quarks, Phys. Lett. B **426**, 125 (1998).

[217] T. Seidensticker, Automatic application of successive asymptotic expansions of Feynman diagrams, in *Proceedings of AIHENP 99, Crete, Greece* (1999).
[218] M. Gerlach, F. Herren, and M. Lang, tapir: A tool for topologies, amplitudes, partial fraction decomposition and input for reductions, Comput. Phys. Commun. **282**, 108544 (2023).
[219] J. A. M. Vermaseren, New features of FORM, arXiv:math-ph/0010025.
[220] B. Ruijl, T. Ueda, and J. Vermaseren, FORM version 4.2, arXiv:1707.06453.
[221] T. van Ritbergen, A. N. Schellekens, and J. A. M. Vermaseren, Group theory factors for Feynman diagrams, Int. J. Mod. Phys. A **14**, 41 (1999).
[222] F. V. Tkachov, A theorem on analytical calculability of 4-loop renormalization group functions, Phys. Lett. B **100**, 65 (1981).
[223] K. G. Chetyrkin and F. V. Tkachov, Integration by parts: The algorithm to calculate β-functions in 4 loops, Nucl. Phys. **B192**, 159 (1981).
[224] S. Laporta, High-precision calculation of multiloop Feynman integrals by difference equations, Int. J. Mod. Phys. A **15**, 5087 (2000).
[225] P. Maierhöfer, J. Usovitsch, and P. Uwer, Kira—A Feynman integral reduction program, Comput. Phys. Commun. **230**, 99 (2018).
[226] J. Klappert, F. Lange, P. Maierhöfer, and J. Usovitsch, Integral reduction with Kira 2.0 and finite field methods, Comput. Phys. Commun. **266**, 108024 (2021).
[227] J. Klappert and F. Lange, Reconstructing rational functions with FireFly, Comput. Phys. Commun. **247**, 106951 (2020).
[228] J. Klappert, S. Y. Klein, and F. Lange, Interpolation of dense and sparse rational functions and other improvements in FireFly, Comput. Phys. Commun. **264**, 107968 (2021).
[229] Ò. L. Crosas and P. Stoffer, One-loop matching of the LEFT to the QCD gradient flow, J. High Energy Phys. 07 (2026) 047.
[230] A. J. Buras, M. Gorbahn, U. Haisch, and U. Nierste, Charm quark contribution to $K^+ \to \pi^+ \nu\bar{\nu}$ at next-to-next-to-leading order, J. High Energy Phys. 11 (2006) 002; 11 (2012) 167(E).
[231] A. Suzuki, Y. Taniguchi, H. Suzuki, and K. Kanaya, Four quark operators for kaon bag parameter with gradient flow, Phys. Rev. D **102**, 034508 (2020).
[232] C. Allton *et al.* (RBC-UKQCD Collaboration), Physical results from $2+1$ flavor domain wall QCD and SU(2) chiral perturbation theory, Phys. Rev. D **78**, 114509 (2008).
[233] Y. Aoki *et al.* (RBC/UKQCD Collaboration), Continuum limit physics from $2+1$ flavor domain wall QCD, Phys. Rev. D **83**, 074508 (2011).
[234] T. Blum *et al.* (RBC/UKQCD Collaboration), Domain wall QCD with physical quark masses, Phys. Rev. D **93**, 074505 (2016).
[235] P. A. Boyle, L. Del Debbio, N. Garron, A. Jüttner, A. Soni, J. T. Tsang, and O. Witzel (RBC/UKQCD Collaboration), SU(3)-breaking ratios for $D_{(s)}$ and $B_{(s)}$ mesons, arXiv:1812.08791.
[236] Y. Iwasaki, Renormalization group analysis of lattice theories and improved lattice action. II. Four-dimensional non-Abelian SU(N) gauge model, arXiv:1111.7054.
[237] D. B. Kaplan, A method for simulating chiral fermions on the lattice, Phys. Lett. B **288**, 342 (1992).
[238] Y. Shamir, Chiral fermions from lattice boundaries, Nucl. Phys. **B406**, 90 (1993).
[239] V. Furman and Y. Shamir, Axial symmetries in lattice QCD with Kaplan fermions, Nucl. Phys. **B439**, 54 (1995).
[240] C. Morningstar and M. J. Peardon, Analytic smearing of SU(3) link variables in lattice QCD, Phys. Rev. D **69**, 054501 (2004).
[241] R. C. Brower, H. Neff, and K. Orginos, The Möbius domain wall fermion algorithm, Comput. Phys. Commun. **220**, 1 (2017).
[242] Y.-G. Cho, S. Hashimoto, A. Jüttner, T. Kaneko, M. Marinkovic, J.-I. Noaki, and J. T. Tsang, Improved lattice fermion action for heavy quarks, J. High Energy Phys. 05 (2015) 072.
[243] S. Güsken, U. Löw, K. H. Mütter, R. Sommer, A. Patel, and K. Schilling, Nonsinglet Axial vector couplings of the baryon octet in lattice QCD, Phys. Lett. B **227**, 266 (1989).
[244] P. A. Boyle *et al.*, Grid: A next generation data parallel C++ QCD library, Proc. Sci. LATTICE2015 (**2016**) 023.
[245] A. Portelli *et al.*, github.com/aportelli/Hadrons: `Hadrons` v1.2 10.5281/zenodo.4293902.
[246] A. Portelli *et al.*, github.com/aportelli/Hadrons: `Hadrons` v1.3 (2022) 10.5281/zenodo.6382460.
[247] B. Efron, Bootstrap methods: Another look at the jackknife, Ann. Stat. **7**, 1 (1979).
[248] U. Wolff (ALPHA Collaboration), Monte Carlo errors with less errors, Comput. Phys. Commun. **156**, 143 (2004); **176**, 383(E) (2007).
[249] S. Schaefer, R. Sommer, and F. Virotta (ALPHA Collaboration), Critical slowing down and error analysis in lattice QCD simulations, Nucl. Phys. **B845**, 93 (2011).
[250] A. Ramos, Automatic differentiation for error analysis of Monte Carlo data, Comput. Phys. Commun. **238**, 19 (2019).
[251] F. Joswig, S. Kuberski, J. T. Kuhlmann, and J. Neuendorf, PYERRORS: A Python framework for error analysis of Monte Carlo data, Comput. Phys. Commun. **288**, 108750 (2023).
[252] M. Bruno and R. Sommer, On fits to correlated and auto-correlated data, Comput. Phys. Commun. **285**, 108643 (2023).
[253] T. Endo, K. Hieda, D. Miura, and H. Suzuki, Universal formula for the flavor non-singlet axial-vector current from the gradient flow, Prog. Theor. Exp. Phys. **2015**, 053B03 (2015); **2024**, 039202(E) (2024).
[254] K. Hieda and H. Suzuki, Small flow-time representation of fermion bilinear operators, Mod. Phys. Lett. A **31**, 1650214 (2016).
[255] J. Borgulat, R. V. Harlander, J. T. Kohnen, and F. Lange, Short-flow-time expansion of quark bilinears through next-to-next-to-leading order QCD, J. High Energy Phys. 05 (2024) 179.
[256] K. G. Chetyrkin, J. H. Kühn, and M. Steinhauser, `RunDec`: A *Mathematica* package for running and decoupling

of the strong coupling and quark masses, Comput. Phys. Commun. **133**, 43 (2000).
[257] F. Herren and M. Steinhauser, Version 3 of RunDec and CRunDec, Comput. Phys. Commun. **224**, 333 (2018).
[258] M. Ciuchini, E. Franco, V. Lubicz, G. Martinelli, I. Scimemi, and L. Silvestrini, Next-to-leading order QCD corrections to $\Delta F = 2$ effective Hamiltonians, Nucl. Phys. **B523**, 501 (1998).
[259] A. J. Buras, M. Misiak, and J. Urban, Two loop QCD anomalous dimensions of flavor changing four quark operators within and beyond the standard model, Nucl. Phys. **B586**, 397 (2000); **B1002**, 116529(E) (2024).
[260] J. Aebischer, P. Morell, M. Pesut, and J. Virto, Two-loop anomalous dimensions in the LEFT: Dimension-six four-fermion operators in NDR, J. High Energy Phys. 05 (2026) 043.
[261] R. V. Harlander, F. Lange, and T. Neumann, Hadronic vacuum polarization using gradient flow, J. High Energy Phys. 08 (2020) 109.
[262] Y. Aoki, B. Colquhoun, H. Fukaya, S. Hashimoto, T. Kaneko, R. Kellermann, J. Koponen, and E. Kou (JLQCD Collaboration), B → D ∗ $\ell\nu\ell$ semileptonic form factors from lattice QCD with Möbius domain-wall quarks, Phys. Rev. D **109**, 074503 (2024).
[263] J.-W. Lee, Matrix elements of $\Delta B = 0$ operators in heavy hadron chiral perturbation theory, Phys. Rev. D **91**, 094511 (2015).
[264] M. Beneke, G. Buchalla, C. Greub, A. Lenz, and U. Nierste, Next-to-leading order QCD corrections to the lifetime difference of B_s mesons, Phys. Lett. B **459**, 631 (1999).
[265] T. Huber, T. Hurth, J. Jenkins, E. Lunghi, Q. Qin, and K. K. Vos, Phenomenology of inclusive $\bar{B} \to X_s \ell^+ \ell^-$ for the Belle II era, J. High Energy Phys. 10 (2020) 088.
[266] M. Fael, J. Jenkins, E. Lunghi, and Z. Polonsky, The standard model prediction for the rare decay $B \to X_s \nu\bar{\nu}$, J. High Energy Phys. 03 (2026) 217.
[267] A. Hasenfratz, C. J. Monahan, M. D. Rizik, A. Shindler, and O. Witzel, A novel nonperturbative renormalization scheme for local operators, Proc. Sci. LATTICE2021 (**2022**) 155.
[268] A. Carosso, A. Hasenfratz, and E. T. Neil, Nonperturbative renormalization of operators in near-conformal systems using gradient flows, Phys. Rev. Lett. **121**, 201601 (2018).
[269] A. Hasenfratz and O. Witzel, Continuous renormalization group β function from lattice simulations, Phys. Rev. D **101**, 034514 (2020).
[270] F. Moretti, U. Nierste, P. Reeck, and M. Steinhauser, Next-to-next-to-leading QCD corrections to the $B^+ - B_d^0$, $D^+ - D^0$, and $D_s^+ - D^0$ lifetime ratios, J. High Energy Phys. 09 (2026) 250.
[271] M. Black, R. Harlander, J. Kohnen, F. Lange, A. Rago, A. Shindler, and O. Witzel, Dataset: Heavy-meson bag parameters using gradient flow (2026) 10.25819/67d6vsvpskcu5g9w.
[272] M. Gorbahn and U. Haisch, Effective Hamiltonian for non-leptonic $|\Delta F| = 1$ decays at NNLO in QCD, Nucl. Phys. **B713**, 291 (2005).